RL-967

DESIGN AND ANALYSIS OF A FOUR-WIRE ANTENNA FOR ANECHOIC CHAMBER ILLUMINATION

by

Changyul Cheon

A dissertation submitted in partial fulfillment
of the requirements for the degree of
Doctor of Philosophy
(Electrical Engineering)
in The University of Michigan
1992

Doctoral Committee:

Research Scientist Valdis V. Liepa, Chairman
Professor Ward D. Getty
Assistant Professor James P. Holloway
Assistant Research Scientist Jianming Jin
Professor Emeritus Chen-To Tai
Associate Professor John L. Volakis

To my parents

ACKNOWLEDGEMENTS

Before presenting the material in this dissertation, which is a result of work I have done over the past five years, I would like to thank and acknowledge the many people and organizations who have contributed to and supported this work.

First, I would like to express my appreciation to the Radiation Laboratory for financial support in the form of a Research Assistantship. In particular, I thank Professor Valdis Liepa for support during my stay.

A special debt of gratitude is owed to Professor Songyop Hahn who was influential during my graduate studies at Seoul National University. My first research career with Professor Hahn was an application of the finite element method to electrical machines. This experience gave me a background of numerical analysis techniques that has been a great help in carrying out this work. He has also had a strong influence on my choice of a research area.

I would also like to thank my associates who have contributed to this effort. I am especially grateful Dr. Jian-ming Jin, Mr. Nenghang Fang, Mr. Martin Kutner, Dr. Kasra Barkeshli, Dr. Songcheol Hong, Mr. Jeffrey Collins, Mr. Yisok Oh, Mr. Youngwoo Kwon for their technical discussions and contributions. I also thank Dr. Jaehong Park, Mr. Sangmin Lee, and Dr. Suntae Chung, not only for their friendship, but their helpful support as well.

Finally, I would like to thank my committee members for their helpful suggestions and careful review of this manuscript. I especially acknowledge my advisor, Dr. Valdis

Liepa, for his constant support and encouragement; he has been a constant source of ideas and insights that have greatly contributed to this work.

TABLE OF CONTENTS

LIST OF FIGURES

CHAPTER I

INTRODUCTION

1.1 Electromagnetic Interference and Compatibility

With the rapid development of microwave engineering, electromagnetic interference (EMI) has become a serious environmental pollution problem. Sources of EMI can be catagorized into natural and artificial. Examples of major natural sources of electromagnetic pollution, or noise, include atmospheric noises produced by electrical discharges(lightning) that occur during thunderstorms, and cosmic noises from the sun[1]-[4]. Since lightning generates an extremely high momentary electromagnetic field, its interference with electronic equipment may be significant, and therefore, many measurements have been performed and much research undertaken to study the effects of lightning[1]-[3]. Likewise, a solar noise that results from an increased solar activity can be a source of interference to electronic equipment[4].

Artificial, or man-made sources of EMI are, strictly speaking, all electric or electronic devices. Some major sources of man-made electromagnetic noise are RF heaters, high A. C. voltage transmission lines, automotive ignitions, trains, fluorescent lamps, microwave ovens, communication transmitters, electric motors, etc.[5]-[9]. Furthermore, the noise generated by the sources mentioned above can be enhanced by reflections from buildings and other obstacles[10]-[15].

There are many electrical and electronic devices that may not operate properly under severe EMI. The problems attributed to EMI range from simple annoyances to catastrophe or permanent failure. Examples of such problems include interference to TV and radio reception[11],[12] and communication[13], malfunction of electronic equipment[16],[17], and failure of digital systems. Since digital systems use low voltage electronic devices, they are easily impacted even under a low level of EMI. To maintain reliable performance of digital systems, EMI testing has become a standard test for electric and electronic devices[18]-[20].

Many countries also impose commercial and military regulations on the level of emissions from electronic or electrical equipment, as well as on the electromagnetic compatibility (EMC) of such equipment with each other. The EMC regulations require that the electronic equipment be designed and built to function correctly under the standard EMI levels without creating additional EMI. When designing equipment to satisfy the EMC requirements, it is desirable to predict the electromagnetic performance of such equipment in its design stage. To accomplish this, numerous prediction techniques have been developed[19]-[24]. However, one still needs to measure and test the EMI and EMC performance of the equipment to verify that it is complies with applicable regulations.

The EMC measurement results are inevitably affected by the measurement equipment and the facilities used. For example, the sensor used in the field measurement affects the field itself. Even though the measurements may include such errors, it is said that one measurement is worth a hundred predictions. It is important that great care be exercised in designing the facility and making the measurements to keep the errors as low as possible.

In the EMC tests, measurements are often used to locate the sources of emission

and the areas of susceptibility. The measurements are also useful for EMC prediction in that they provide magnitudes of fields, voltages, and currents, which form the bases for the prediction analysis. There are several diagnostic measurements typically performed: radiated electric and magnetic field measurements, conducted line voltage and current measurements, and radiated and conductive susceptibility measurements. For both the radiated and susceptibility measurements, a broadband antenna is desirable to receive and transmit the signals. This thesis deals with a design and analysis of an antenna that simplifies these EMC and EMI measurements, due to its extremely broadband characteristics.

1.2 Desirable Antenna Properties for EMC Measurement and a Four-wire Antenna

Since the majority of unintentional electromagnetic noise occupies a wide frequency spectrum, a broadband measurement technique is desirable for the EMC measurements. The frequency range in measurements is limited by the bandwidth of the measurement system including its antenna. Thus, the equipment used in broadband measurements needs to be designed to cover as wide a frequency range as possible. Otherwise, the number of measurements becomes large and costly to cover the required frequency range (e.g., 10 KHz to 18 GHz in electric field susceptibility tests). Therefore, the design of broadband components[25]-[37] is quite desirable.

With the availability of broadband measurement equipment, broadband radiators are also needed. For this, many antenna designs, which show over 10 to 1 broadband characteristics, have been developed and are used. These include spiral antennas, log-periodic antennas, horn antennas, tapered horn antennas with resistive loading, ridge-horn antennas, tapered resistive dipoles, etc.[29]-[37]. However, these antennas,

except for the wire antennas, are inadequate for low frequency measurements since the antenna becomes physically too large to handle and too expensive to construct. A long wire antenna is one of the structures that has broadband potential and is economical and simple to implement[33],[34]. However, the long wire by itself is not a broadband device nor does it produce the desired field pattern. The broadband and uniform field characteristics can be achieved by forming the proper wire geometry and using a distributed and lumped loading at the ends of the wires[34],[37].

The broadband antennas used in EMC measurements are different from broadcast or communication antennas in the field distribution aspect. In a broadcast antenna, a high directivity is usually a desirable parameter. In EMI measurements, on the other hand, an antenna with an excessive directivity may be disadvantageous[38]. An overly narrow beamwidth may not cover the entire equipment under test (EUT), and would necessitate an increase in the distance between the antenna and the test unit.

Likewise, it is desirable to design an antenna for EMI measurements that can produce a uniform field distribution in the test area over a broad frequency range. In radiated susceptibility tests, for example, an antenna is required to generate uniform fields over the EUT. A tapered resistive dipole[37] is a simple wire antenna that can be used as a wideband antenna, but it is not adequate in creating a uniform field. If a far field region is chosen as the test region, then a uniform field distribution is obtained. However, since the field intensity decreases with distances, the signal would be too low to make the satisfactory measurements. This can be overcome by using a near field region as the test region, provided uniform fields can be obtained in this region.

Another important aspect of the broadband antenna is its input impedance vari-

ation with frequency. The EMC measurement antennas are specified with a nominal input impedance of 50 ohms, whereas the actual impedance of the antenna may be much different. This discrepancy results in a high voltage standing wave ratio(VSWR) that may limit the use of high power amplifiers in driving the antenna. In order to obtain a lower VSWR, impedance matching may be used, but this is difficult to achieve for high VSWR cases, especially over a broadband frequency range. Consequently, an antenna must be designed with an input impedance that does not vary appreciably over the required frequency range. Besides these aspects, it is desirable to build the antenna at a reasonably low cost.

To satisfy such requirements, a four-wire antenna is proposed in this thesis. The advantages of the four-wire antenna are summarized as follows:

- broadband characteristics
- low frequency operation ($\geq$ 50 MHz)
- uniform field distribution in the test region
- nondispersive characteristics
- compatibility with anechoic chamber use
- low cost and relatively simple implementation

The idea of the four-wire antenna basically comes from the parallel four transmission-line simulator proposed by Carl E. Baum[39]. He found that four parallel wires can create uniform field distribution at the center of the four wires. The most uniform field distribution is obtained with the specific spacing ratio of $1/\sqrt{3}$ between wires of the same polarity to the wires of the opposite polarity. This idea is applied to a

double-V antenna, and leads to the concept of the four-wire antenna presented in this thesis.

The four-wire antenna is formed by two V antennas spreading away from each other from the center feed (see figure 2.1). Four wires essentially form a low frequency (low-pass) transmission system[40],[41] since they support waves whose wavelengths are larger than, or at most equal to, the spacing between the wires. The field in the test region is essentially a TEM wave with a spherical phase front. The four-wire antenna is also a broadband radiator. When the spacing of the antenna approaches a wavelength, the wave starts to radiate and propagate in the same direction as the low frequency TEM wave. Thus, the high frequency limit of the four-wire antenna depends only on the gap size and its geometry at the feed. An important property of this antenna is that it is essentially dispersionless—the currents on the wires, or the TEM waves, travel at the same velocity as the launched waves thus preserving the phase coherence.

Besides the EMC application, the four-wire antenna can also be used in other electromagnetic measurements such as backscattering or radar cross section measurements and surface field measurements.

1.3 The Use of an Anechoic Chamber

In general, outdoor measurements may be more accurate than indoor measurements if the ambient and other external noise sources are sufficiently small. However, it is practically impossible to avoid such noises and weather conditions may further delay or interfere with the measurements. For such reasons, EMC and EMI measurements are often made in shielded rooms.

The use of a shielded room, however, can produce errors in both the radiated emis-

sion measurements and the radiated susceptibility tests. The errors are attributed to:

- internal room reflections
- coupling of antennas with the conductive walls
- field distortion due to standing waves
- room excitation in various cavity modes

These errors, however, can be reduced significantly by covering the walls with absorbing materials[38]. Such rooms are called anechoic chambers.

The anechoic chamber uses absorbing materials (absorbers) that are placed on the walls, ceiling, and floor of the chamber to absorb microwave energy. These absorbers have good performance at relatively high frequencies (above 300 MHz). However, in the lower frequency range (below 300 MHz), the absorbers perform poorly and may even introduce additional scattering[42]-[43]. Despite these inherent problems at low frequencies, the use of anechoic chambers is still a popular facility for EMC measurements.

Under the study presented in this thesis, a four-wire antenna was installed in the tapered anechoic chamber at the Radiation Laboratory of the University of Michigan. Before installing the antenna in the chamber, distortions in field distribution due to the chamber walls were anticipated and are analyzed here. It was expected that the performance of the four-wire antenna in the chamber at high frequencies (above 300 MHz) would be essentially the same as in free space, while the low frequency performance would be significantly different from that in free space. The chamber resonances and reflections would have a significant affect on the field distributions.

Therefore, to fully understand the performance of such an antenna in the anechoic chamber, the analysis must take into account the antenna and the chamber as a whole.

1.4 Overview

Chapter I presents the introduction of this thesis. Chapter II presents an analysis of the four-wire antenna when it is located in free space. In this analysis, an appropriate loading resistance is determined that eliminates the standing waves on the wires. Then the input impedances and the field distributions are computed to characterize the antenna.

Chapter III presents an analysis of the wedge absorber used in the anechoic chamber based on the method of moment technique. Volume-surface integral equations are developed for this analysis. When considering the whole chamber it is desirable to simplify the wedge absorber to an equivalent layered slab to reduce the size of the (numerical) problem. The equivalent layer is formulated so that its reflectivity is compatible with that of the original absorber. These results are then used in analyses presented in Chapters IV and V.

Chapter IV presents an analysis of a dipole antenna when it is located near lossy dielectric layers backed by a perfect conductor. A Green's function is derived which satisfies the wave equations with proper (absorber) boundary conditions for this analysis. Lossy dielectric layers with conductor backing simulate the absorbers and the chamber walls, respectively. This particular study provides pertinent information on the performance of the absorbing materials that are illuminated from nearby wire antennas.

Chapter V presents an analysis of the tapered anechoic chamber with the four

wire antenna using a three dimensional finite element technique. To reduce the total number of unknowns, the chamber geometry is simplified by replacing the pyramidal absorbers with equivalent absorbing layers. In the analysis, currents and field distributions are obtained at frequencies below 100 MHz.

Chapter VI describes the construction and the installation of the four-wire antenna in the anechoic chamber. The electrical performance of the antenna and the test measurements are presented. These include the antenna impedance measurements, field distribution measurements, and sample measurements of surface current and backscattering.

Finally, Chapter VII provides conclusions and suggestions for future work.

CHAPTER II

ANALYSIS OF FOUR-WIRE ANTENNA IN FREE SPACE

2.1 Introduction

In this chapter, a four-wire antenna is analyzed in free space. The results of the analysis provide data that are necessary for the design and construction of a four-wire antenna. The results of the analysis are also used to predict the performance of the antenna.

The free space analysis provides input impedances, current distributions on wires, field distributions, and optimum loading resistance distributions. To obtain the current distributions, the computer code called Numerical Electromagnetic Code (NEC) [44] is used. The NEC program uses the method of moments to solve an integral equation for the electric field. This equation, given below, models the electromagnetic response of thin-wire structures of small or vanishing volume conductors. When an incident electric field, $\vec{E}^{inc}$ is given, the total electric field is written as

$$\vec{E}^{tot}(\vec{r}) = \vec{E}^{inc}(\vec{r}) + \vec{E}^{scat}(\vec{r}) \tag{2.1}$$

where

$$\vec{E}^{tot}(\vec{r}) \;=\; Z(\vec{r})\vec{J}(\vec{r})$$

$$\vec{E}^{scat}(\vec{r}) = \frac{-j\eta_0}{4\pi k_0}\int_V \vec{J}(\vec{r'})\cdot\overline{\overline{G}}(\vec{r},\vec{r'})dV'$$

with

$$\overline{\overline{G}}(\vec{r},\vec{r'}) = (k_0^2\overline{\overline{I}} + \nabla\nabla)g(\vec{r},\vec{r'})$$

$$g(\vec{r},\vec{r'}) = \exp(-jk_0|\vec{r}-\vec{r'}|)/|\vec{r}-\vec{r'}|$$

$$k_0 = \omega\sqrt{\mu_0\epsilon_0}$$

$$\eta_0 = \sqrt{\mu_0/\epsilon_0}$$

and $\overline{\overline{I}}$ is a unity dyad. The impedance, Z, is defined as the ratio of the electric field to the current density and $\vec{E}^{tot}(\vec{r})$, $\vec{E}^{inc}(\vec{r})$, and $\vec{E}^{scat}(\vec{r})$ denote the total, incident, and scattered field, respectively. In the above equations and throughout the thesis, $exp(j\omega t)$ time convention is implied.

Once the current distribution on the antenna is obtained for a given voltage source, the input impedance is calculated by dividing the driving voltage by the current at the input terminals. The total field distributions are obtained from Eq.(2.1) by substituting the computed current density $\vec{J}(\vec{r'})$. The analysis is performed up to 1 GHz since the numerical implementation is computationally too intensive at higher frequencies.

In section 2.2 the optimum loading distribution is determined to suppress current reflections from the wire ends, thus enhancing the antenna bandwidth. In section 2.3 the computed input impedances of the four-wire antenna in free space are presented, and in section 2.4 the computed field distributions at the test area are presented.

2.2 Effects of Loading Resistance on Current Distributions

A long wire is usually used for a traveling wave antenna. When one end is excited by a source and the other end is open, there exists a standing wave pattern that is

the result of two waves propagating in opposite directions along the wire. Since the waves are radiated even though the medium is lossless, the waves propagating in opposite directions do not have the same magnitudes, except at the open end. The resultant standing wave has a decaying sinusoidal wave form. The long wire antennas are usually designed to have a traveling current wave only in one direction. This is achieved by loading a proper impedance at the end of the wire so that the reflection at the end is minimized. The value of the proper impedance is usually adjusted about the characteristic impedance of the wire antenna to minimize the reflection.

By using loading to produce traveling waves only in one direction, the antenna illuminates single direction and produces a more uniform field. In addition, the voltage standing wave ratio (VSWR) at the feed point is acceptable over a broad frequency range.

The effective resistance loading over a broad frequency range is obtained by using distributed resistances. The proper loading resistance distributions are achieved by considering the following: since the high frequency waves are highly dependent on the slope of the loading resistance per unit length and are dissipated over a short distance, the early part of loading resistance must have a small value and vary slowly. The low frequency waves are less sensitive to the slope of resistance and propagate farther in comparison to the high frequency waves. Therefore, the latter part of the loading resistance can be changed more rapidly and the value must be large enough to dissipate the lowest frequencies. Consequently, the length of distributed loading resistance must be sufficiently long to eliminate the lowest frequency wave without allowing the highest frequency wave to be reflected due to abrupt changes in the resistance.

There are a number of ways to distribute the loading resistances, including the

forms of quadratic, exponential, and inverse functions. In this analysis, a quadratic function is chosen,

$$\frac{R(z)}{R_0} = \begin{cases} (z-l)^2/l_R^2 & \text{if } l < z < l + l_R \\ 0 & \text{otherwise} \end{cases} \tag{2.2}$$

where

z : distance from the source along the wire [cm]

$R(z)$: resistance density [ohms/cm]

R_0: maximum resistance density at the end of the wire [ohms/cm]

l : antenna wire length without the loading resistance [cm]

l_R: the length of loading resistance [cm].

Figure 2.1 shows the four-wire antenna with the loading resistance distribution. With this loading distribution, the wire currents on the antenna are computed for different values of R_0. The results are shown in Figure 2.2. The antenna wires are 15 meters long (l=15 m) and the loading resistances are distributed over 3 meters (l_R = 3 m). The operating frequency is 100 MHz. For the distributed resistances with R_0 = 10 ohms/cm, the resistance value is too small to eliminate the standing waves. The current with this loading is not sufficiently attenuated at the end of the loading. Thus, there exists a reflected wave at the end of the loading that generates a standing wave in currents. When R_0 is 100 ohms/cm, the fast increase of the initial section of the tapered loading causes reflections that give rise to a standing wave in currents. Using a trial and error approach, the loading with R_0=18 ohms/cm is found to eliminate the standing waves almost entirely. With this loading resistance distribution, most currents are dissipated before reaching the end of the loading and the slope of resistance is small enough as not to reflect the waves.

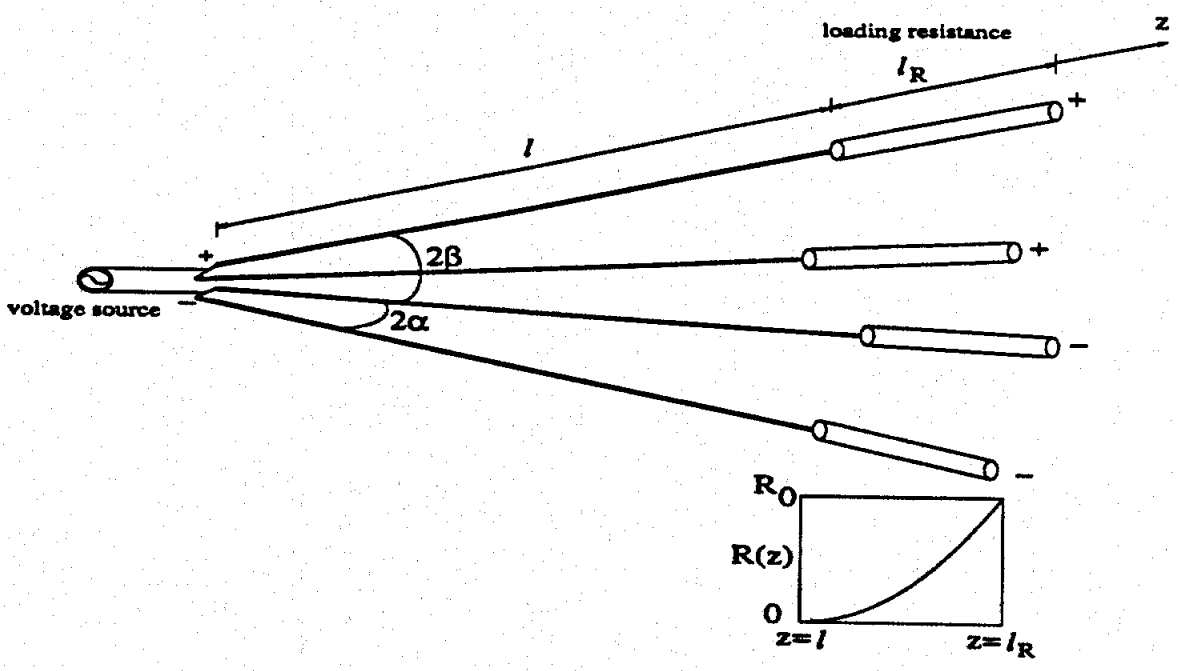

Figure 2.1: The four-wire antenna with loaded resistance distribution.

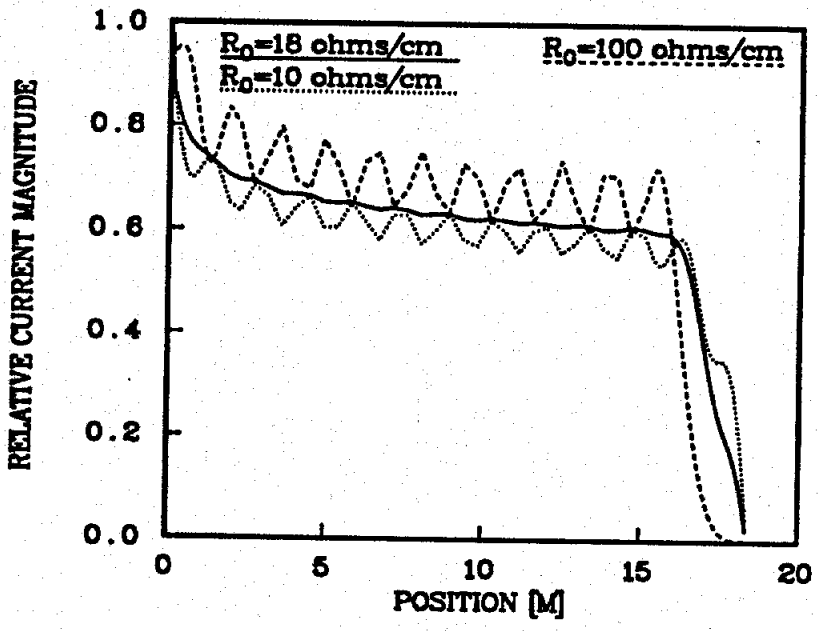

Figure 2.2: Current distribution on the wire of the four-wire antenna.

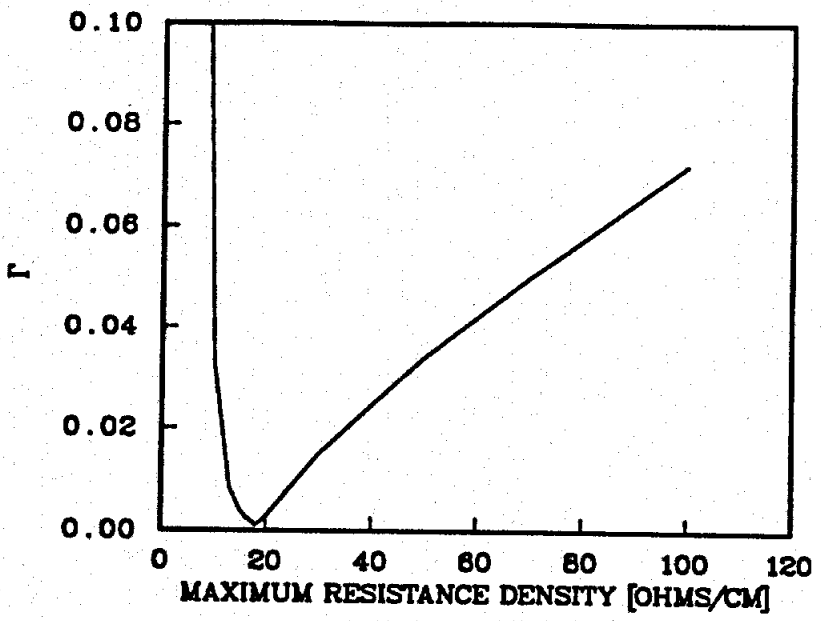

Figure 2.3: Γ as a function of R_0 at 100 MHz.

Figure 2.3 shows a reflection coefficient, Γ, as a function of maximum resistance density, R_0. The reflection coefficient is defined as

$$\Gamma = Average\left[\frac{I_{max} - I_{min}}{I_{max} + I_{min}}\right] \tag{2.3}$$

where I_{max} and I_{min} are locally maximum and minimum values of current over a distance of a half wavelength, respectively. Figure 2.3 indicates that the optimum R_0 is 18 ohms/cm for the resistance distributions of Eq.(2.2). Computations also showed that the same resistance distribution eliminates the standing wave effectively in dipoles and V antennas of the same length and diameter as the four-wire antenna. Numerical results also showed that the maximum resistance value, R_0, is not dependent on the inside angle of the four-wire antenna. This optimum loading resistance is valid for higher frequencies as shown in Figure 2.4 for the four-wire antennas, where Γ is plotted as a function of frequency. However, the optimum value of R_0 did seem to be highly dependent on the radius of the wire. The optimum R_0 decreases as the

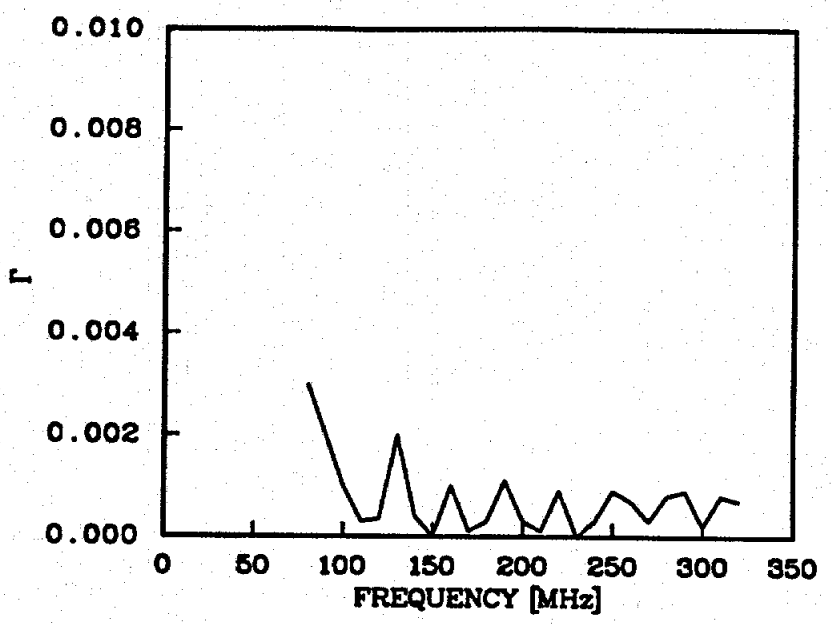

Figure 2.4: Γ as a function of frequency when $R_0 = 18$ ohm/cm.

wire becomes thicker.

Harold E. Foster studied the current distribution on a transmission-line for various type of loading resistance[45]. In his study, Foster used a one meter long transmission-line when the wavelength was 8/9 meters. The loading resistance was distributed over one wavelength. He obtained optimum current distribution when the loading was an inverse resistance function of the distance and given by

$$R(z) = \frac{9}{4} Z_0 \left(\frac{1}{1-z} - 1\right) \quad \text{[ohms/meter]} \tag{2.4}$$

where Z_0 is the characteristic impedance of the transmission-line and z is measured in meters along the line. Using the resistance distribution of Eq.(2.4), Foster obtained a reflection coefficient of about 0.005. Although his inverse resistance distribution is optimum in transmission-lines, it is not clear whether it is valid for the four-wire antenna since the characteristic impedance of the four-wire antenna is not constant due to diverging geometry of the wires. In our analysis, the comparison of various

loading resistance distributions for a long wire antenna was not performed. However, according to the Figures 2.3 and 2.4, the quadratic function distribution with optimum R_0 produces sufficiently good results when compared to Foster's results.

Foster also showed that although the continuous resistance distribution reduces the reflection coefficient more than the discrete loading resistance, an eighth of a wavelength spacing of lumped resistances produces very nearly the same current distribution and transmission-line impedances as a continum of resistance loading. The numerical computation in our analysis confirmed that the same is valid for the four-wire antenna.

2.3 Input Impedance

The useful bandwidth of an antenna is the range of frequencies over which the antenna maintains a certain required input impedance, radiation pattern, and polarization characteristics. When designing an antenna to operate over a large bandwidth, the major task is to maintain a desired input impedance and radiation pattern characteristics. Since the main interest of this study is in the near field region, the primary concern is to maintain the desired input impedance over a wide frequency range.

To find input impedance, the current was calculated for the given voltage source and then the applied voltage was divided by the current at the input terminals. Figure 2.5 shows the input impedance of the four-wire antenna with and without loading resistances. Without loading, the impedance oscillates as a function of frequency, and this would not be adequate for broadband operation. With proper loading, the input impedance oscillates below 50 MHz and becomes uniform above 50 MHz. Hence, the low frequency limit with such a loading is 50 MHz.

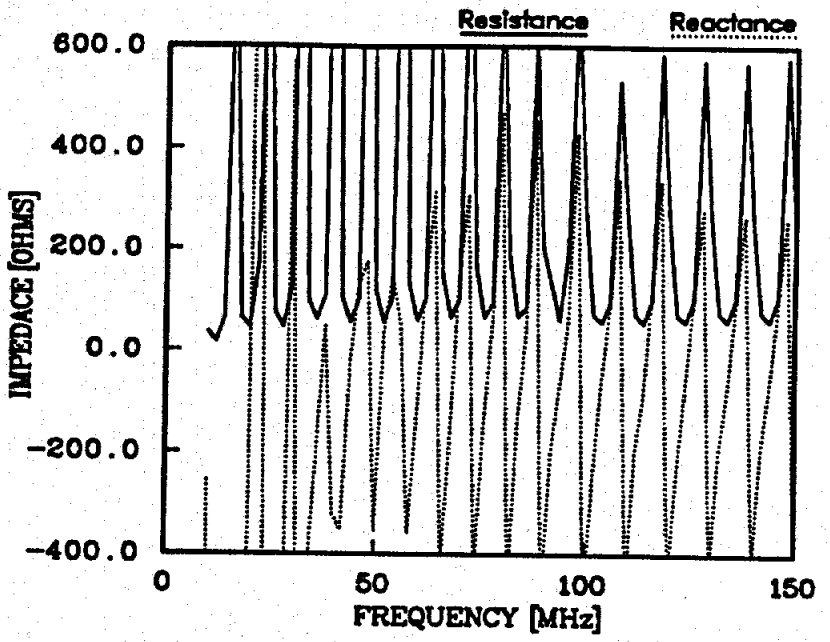

(a) Input impedance without loading.

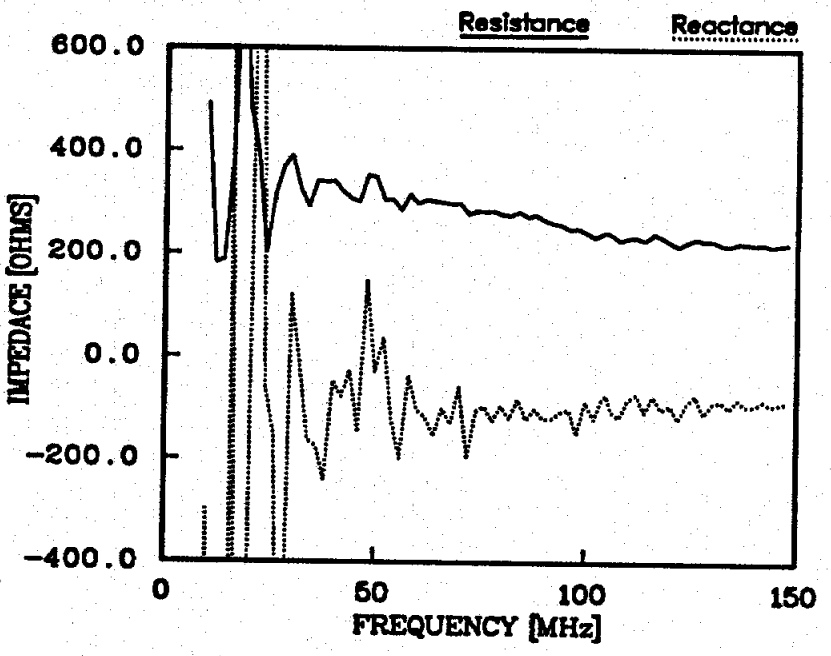

(b) Input impedance with the optimum loading.

Figure 2.5: Comparison of input impedances between open and loaded terminations

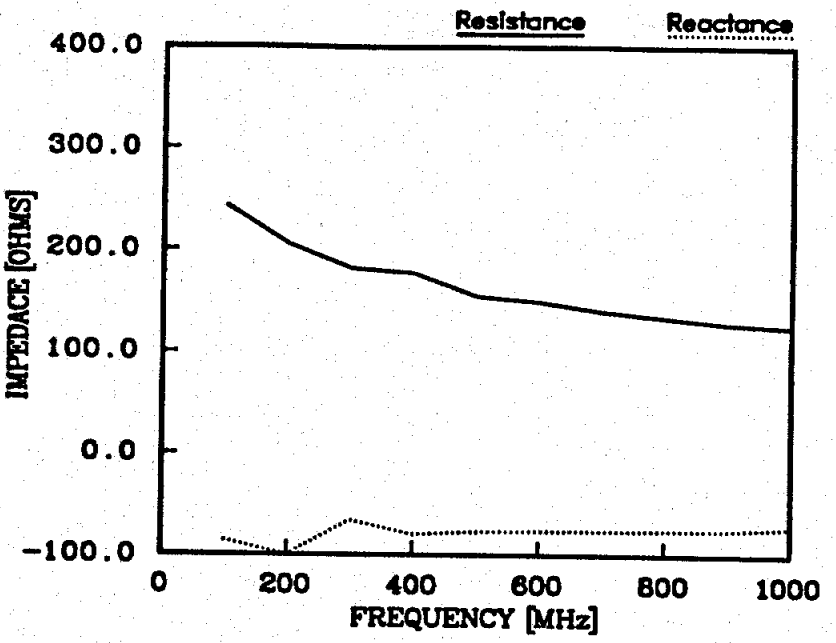

Figure 2.6: Input impedance of the four-wire antenna with resistive loading.

Figure 2.6 shows the input impedance of the four-wire antenna with the loading for expanded frequency range. Based on the input impedance, this analysis shows that the possible frequency range is from 50 MHz to over 1 GHz. The upper frequency limit, however, is expected to extend to about 5 GHz, according to the trend of Figure 2.6, and is limited only by the geometry of the feed.

2.4 Field Distribution

Since the four-wire antenna system will eventually be used in an anechoic chamber, the design parameters such as wire length, inner angle, loading length etc. must be chosen under the consideration of the anechoic chamber geometry. The anechoic chamber at the University of Michigan has a tapered cross section that is shown in Figure 2.7. The main dimensions of the chamber are 18 feet wide, 60 feet long, and 18 feet high. The anechoic treatment consists of 72 inch pyramidal absorbers on the

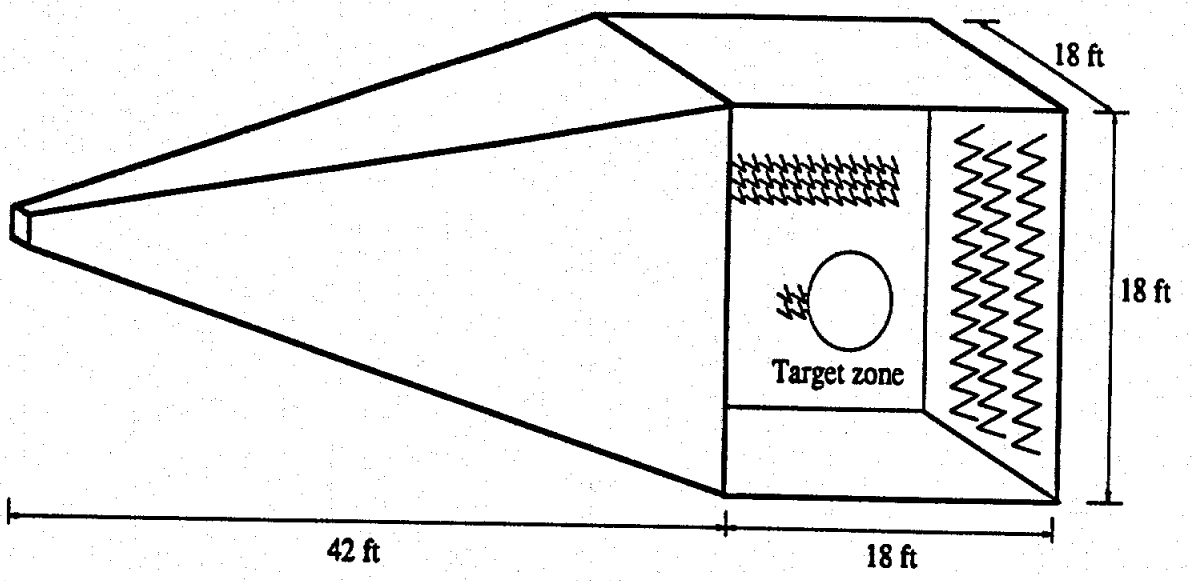

Figure 2.7: Geometry of anechoic chamber.

endwall of the chamber; 24 inch and 18 inch pyramidal absorbers, and 12 inch wedge absorbers on the side walls, ceiling, and floor surfaces of the 18 ft. × 18 ft. × 22 ft. test region; and 18 inch pyramidal and 12 inch wedge absorbers on remaining surfaces of the tapered section. In addition, the 140 square feet of the test region floor surface is treated with 24 inch walkway absorber.

Carl E. Baum[39] reported on a parallel four transmission-line simulator designed for a uniform field distribution near the center of the four wires. He found that the four wires can create the best uniform field distribution at the center of the four wires with the specific spacing ratio of $1/\sqrt{3}$ between wires of the same polarity to the wires of the opposite polarity.

To find the widest uniform field distributions around the test region for the four-wire antenna, field computations were performed for various lengths and wire angles

considering the dimensions of the anechoic chamber. The Baum's ratio was found to be applicable to the four-wire antenna based on an inner angle ratio instead of a spacing ratio. The optimum dimensions that have the widest uniform field distribution are

$$\alpha = 4.85 \text{ degrees} \qquad \beta = 8.37 \text{ degrees}$$

$$l = 15.0 \text{ meters} \qquad l_R = 3.0 \text{ meters}$$

where α, β, l and l_R are defined in Figure 2.1. The wire diameter is 0.125 inch. For these dimensions, the four-wire antenna has a uniform field within $\pm$ 0.5 dB within a region defined by a two meter diameter sphere.

A design with four wires symmetrically placed was also investigated. With such an arrangement, the field distribution is not optimal, but some flexibility is provided. The configuration allows the user to change the polarization of the antenna by simply selecting the proper excitation at the feed point. Also, the symmetric arrangement is more compatible with the square cross section of the chamber.

With the following design specification, the antenna can illuminate the uniform field distribution within $\pm$0.5 dB inside a target area defined by a 1.2 meter diameter sphere.

$$\alpha = 8.37 \text{ degrees} \qquad \beta = 8.37 \text{ degrees}$$

$$l = 15.0 \text{ meters} \qquad l_R = 3.0 \text{ meters}$$

Similarly, a $\pm$1 dB uniform field distribution exists within a two meter diameter sphere. Figure 2.8 shows the field deviation within a test region defined by a two meter diameter sphere at various frequencies. In Figures 2.8(a) and (b), the field deviations along the horizontal and vertical axis of the cross section plane, which is located 14 meters from the feed, are shown, respectively. These fields are normalized to the field at the center point. Figure 2.9 shows the field deviation along the

propagation direction. In this figure, the fields are normalized to the field at the 14 meter point.

In Figure 2.10, the field deviation is shown as a function of frequency in the test zone of a one meter diameter sphere. The degree of field deviation is defined as the ratio of the maximum field to the minimum field within the sphere. Here, we see that the deviation is $\pm$ 0.25 dB from 100 MHz to 1000 MHz.

In practice antennas are usually located at a sufficient distance from other obstacles that they may be analyzed as isolated antennas in so far as impedances and current distributions are concerned. The four-wire antenna under consideration will be built in an anechoic chamber relatively close to the walls. Hence, it is expected that a substantial interaction between the antenna and the chamber will occur. This interaction is considered in the following chapters.

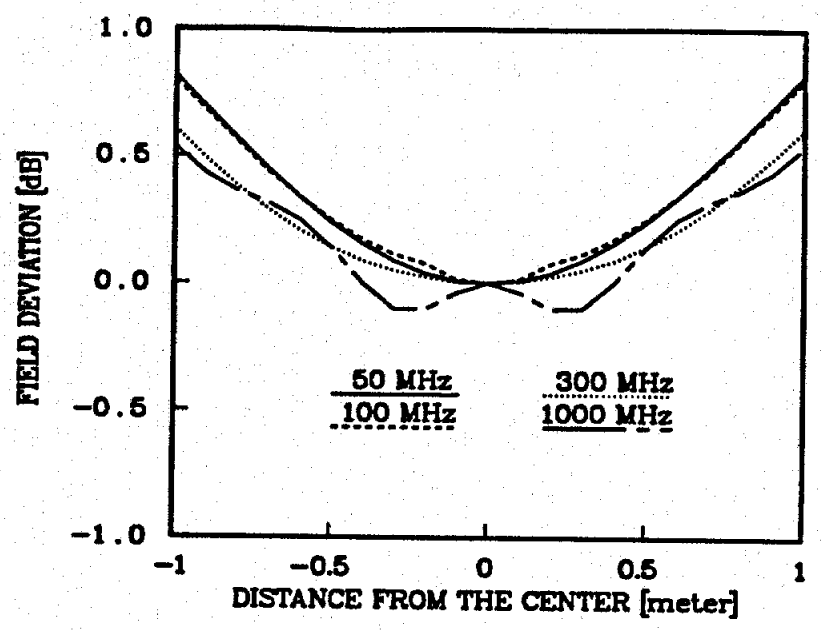

(a) horizontal

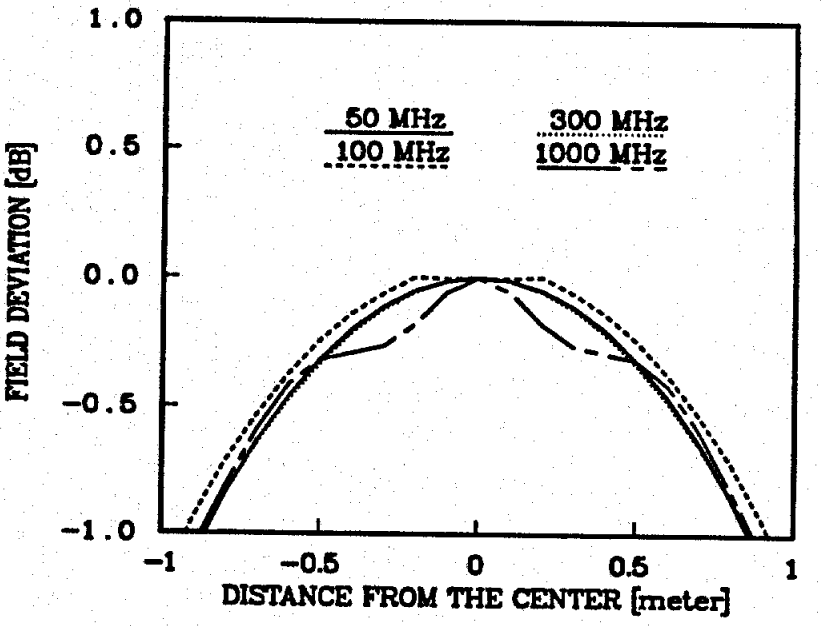

(b) vertical

Figure 2.8: Field deviation at the cross section plane that is 14 meters from the feed. Fields are normalized to the field at the center point.

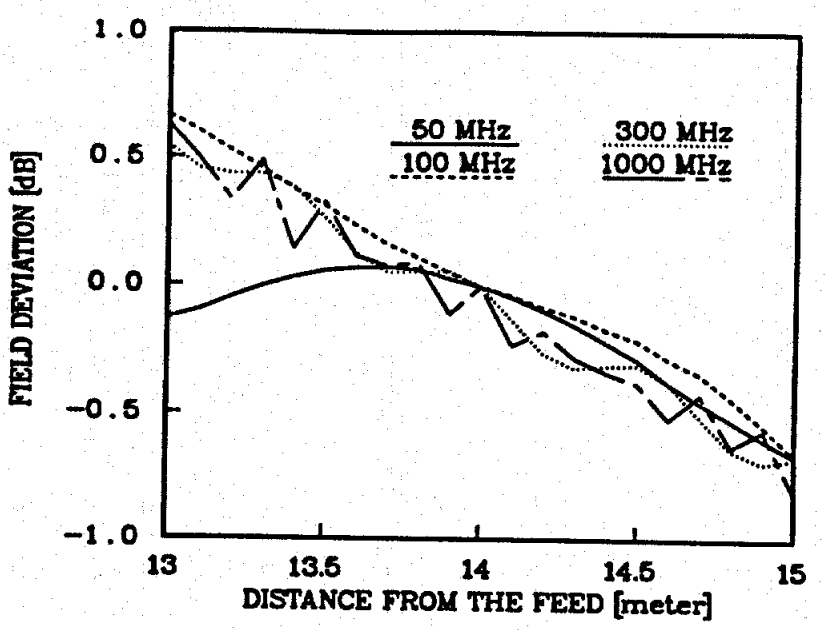

Figure 2.9: Field deviation along the propagation direction. Fields are normalized to the field at the 14 meter point from the feed.

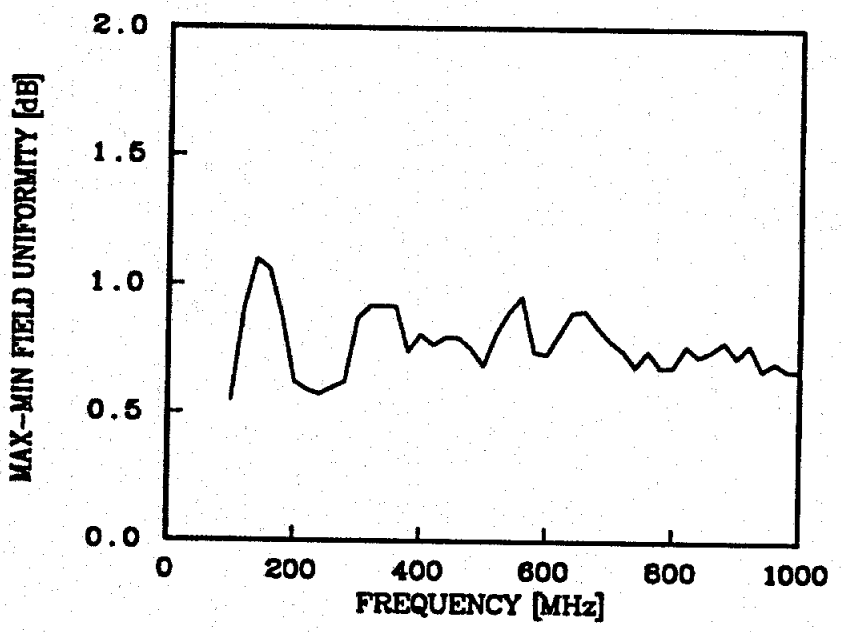

Figure 2.10: Field deviation of target area versus frequency. Field deviation is defined as the maximum field divided by minimum field in the one meter diameter sphere.

CHAPTER III

FULL WAVE ANALYSIS OF WEDGE ABSORBER

3.1 Introduction

In this chapter, a full wave analysis of the wedge absorber is performed to obtain an equivalent layer. The equivalent layer is formulated so that its reflectivity is compatible with that of the original absorber. This equivalent layer is then used in Chapter V, where the four-wire antenna in the chamber is solved numerically.

The use of wedge type absorbing materials is gaining popularity in anechoic chamber linings, especially on side walls where incident illumination is near grazing. A substantial number of studies have been done on these materials and their applications, both experimentally and theoretically[46], and in the latter case, high frequency techniques such as geometrical theory of diffraction (GTD) have been applied. In this chapter a numerical technique is presented that covers low- and mid-frequency regions in order to analyze the scattering created by an infinitely long periodic wedge absorber backed by a perfect conductor.

The wedge absorbers used on the side walls of the anechoic chamber have a periodic structure in the transverse direction. The periodic structures have been studied by many researchers both analytically[47] and numerically[48]-[52]. Usually,

these structures are catagorized into two classes of problems: a dielectric surface scattering problem[48],[49] and a metallic or resistive grating problem[50]-[52]. Both problems are solved by using the surface integral equations for electric and magnetic fields. The surface integral equations, however, do not include the multiple reflections that occur due to the finite thickness of the absorber. When the absorber contains a finite dielectric volume or depth, the volume integral must also be used.

The volume-surface integral equations (VSIEs) were introduced by Jin, et al.[53] to solve these types of problems. The original VSIEs were formulated only for a side incident wave (which means that the incidence plane is perpendicular to the longitudinal axis of the wedge absorber) and this leads to two decoupled integral equations for E- and H-polarized cases. However, when treating the absorbing wedges on the side walls of an anechoic chamber, the forward incident wave (which means the incidence plane is parallel to the longitudinal axis) must be considered since the wedges are illuminated by such a wave.

In this chapter, the VSIEs are modified with proper boundary conditions. The resultant VSIEs are two coupled (for forward incidence) or decoupled (for side incidence) integral equations for longitudinal electric and magnetic fields. The modified VSIEs are then applied to the forward incidence problem as well as the side incidence problem of the wedge absorber. Since the wedge absorber is a periodic structure, the Floquet mode expansion can be used to reduce the analysis region.

In section 3.2 the modified volume-surface integral equations are derived and applied to a periodic geometry. The numerical technique is described in section 3.3. In order to obtain realistic results, the dielectric and the magnetic constants of the absorbing material were measured using the coaxial line technique. The measurements and results are presented in section 3.4. Finally, in section 3.5, numerical results for

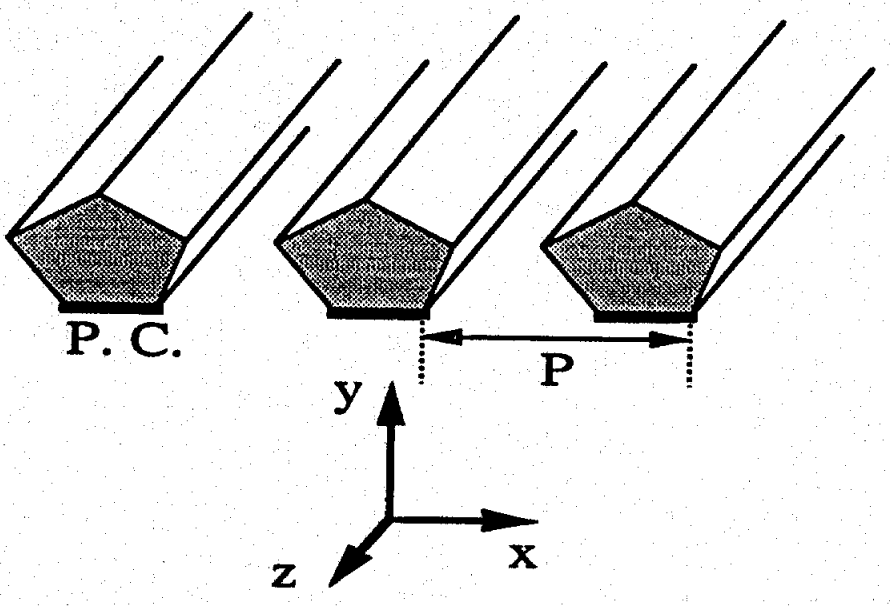

Figure 3.1: Infinitely periodic cylindrical structure on a perfect conductor (P.C.).

the absorber are presented. Also, an equivalent layered slab is obtained for which the reflection coefficients are similar to those of the wedge absorber. The use of an equivalent slab reduces the complexity of the problem, especially in numerical analysis.

3.2 Formulation

Consider a cylindrical or two dimensional structure composed of periodic arbitrary cross sections embedded in a single surrounding medium as depicted in Figure 3.1. In the cylindrical geometry, provided the axial component of the propagation vector is known, two components are sufficient to obtain all the six electromagnetic field components from Maxwell's equations. Therefore, a formulation of equations to solve for any two components of the field is required and here, the axial components of the electric and magnetic fields are chosen. Once the axial components, E_z and

H_z, are found, the other four field components are obtained from

$$E_x = \frac{-jk_z}{k^2 - k_z^2}\left(\frac{\partial}{\partial x}E_z + \frac{\omega\mu}{k_z}\frac{\partial}{\partial y}H_z\right)$$
$$E_y = \frac{-jk_z}{k^2 - k_z^2}\left(\frac{\partial}{\partial y}E_z - \frac{\omega\mu}{k_z}\frac{\partial}{\partial x}H_z\right)$$
$$H_x = \frac{-jk_z}{k^2 - k_z^2}\left(\frac{\partial}{\partial x}H_z - \frac{\omega\epsilon}{k_z}\frac{\partial}{\partial y}E_z\right)$$
$$H_y = \frac{-jk_z}{k^2 - k_z^2}\left(\frac{\partial}{\partial y}H_z + \frac{\omega\epsilon}{k_z}\frac{\partial}{\partial x}E_z\right)$$

where k_z denotes an axial component of the propagation vector and $k^2 = k_0^2\mu_r\epsilon_r = \omega^2\mu\epsilon$.

In an isotropic homogeneous medium, the $\hat{z}$ component of the total electric or magnetic field, denoted by $F(\vec{r})$, satisfies the scalar wave equation

$$\nabla^2 F(\vec{r}) + k^2 F(\vec{r}) = 0$$

Applying Green's second identity to this wave equation and the free space Green's function, $G_0(\vec{r}, \vec{r'})$, which satisfies

$$\nabla^2 G_0(\vec{r}, \vec{r'}) + k_0^2 G_0(\vec{r}, \vec{r'}) = -\delta(\vec{r} - \vec{r'})$$

one can obtain an integral equation for the $\hat{z}$ component of electric field inside the dielectric medium, $E_z(\vec{r'})$, as

$$\oint_\Gamma (G_0 \nabla' E_z(\vec{r'}) - E_z(\vec{r'})\nabla' G_0) \cdot d\Gamma' + k_0^2 \int_\Omega (\mu_r\epsilon_r - 1) E_z(\vec{r'}) G_0 d\Omega' = E_z(\vec{r}) \quad (3.1)$$

In free space or outside the medium, the integral equation for the $\hat{z}$ component of electric field, $E_z^a(\vec{r'})$, is

$$\oint_\Gamma (G_0 \nabla' E_z^a(\vec{r'}) - E_z^a(\vec{r'})\nabla' G_0) \cdot d\Gamma' = E_z^{inc}(\vec{r}) - E_z^a(\vec{r}) \quad (3.2)$$

In the above equations, Ω and Γ denote the volume and boundary surface of the dielectric medium and $\vec{r}$ and $\vec{r'}$ represent the field and source point vectors, respectively. $E_z^{inc}(\vec{r})$ is a $\hat{z}$ component of the incident electric field and is given in the

form

$$E^{inc}(\vec{r}) = E_0 exp\{-j(k_{xi}x - k_{yi}y + k_{zi}z)\}$$

For side and forward incidences, which are shown in Figures 3.2(a) and (b), respectively, the propagation vector of the incident field is defined as

$$\vec{k_i} = k_{xi}\hat{x} - k_{yi}\hat{y} + k_{zi}\hat{z}$$

where

$$k_{xi} = \begin{cases} k_0 \sin\phi_i & \text{for side incidence} \\ 0 & \text{for forward incidence} \end{cases}$$

$$k_{yi} = \begin{cases} k_0 \cos\phi_i & \text{for side incidence} \\ k_0 \cos\theta_i & \text{for forward incidence} \end{cases}$$

$$k_{zi} = \begin{cases} 0 & \text{for side incidence} \\ k_0 \sin\theta_i & \text{for forward incidence} \end{cases}$$

and ϕ_i and θ_i are angles of incidence measured from the axis normal to the xy and yz planes, respectively.

In a way similar to the one described above, integral equations inside the medium for the $\hat{z}$ component of the magnetic field, $H_z(\vec{r'})$, are obtained as

$$\oint_\Gamma (G_0 \nabla' H_z(\vec{r'}) - H_z(\vec{r'}) \nabla' G_0) \cdot d\Gamma' + k_0^2 \int_\Omega (\mu_r \epsilon_r - 1) H_z(\vec{r'}) G_0 d\Omega' = H_z(\vec{r}) \quad (3.3)$$

and for $H_z^a(\vec{r'})$, in free space, as

$$\oint_\Gamma (G_0 \nabla' H_z^a(\vec{r'}) - H_z^a(\vec{r'}) \nabla' G_0) \cdot d\Gamma' = H_z^{inc}(\vec{r}) - H_z^a(\vec{r}) \quad (3.4)$$

Next, we apply the boundary conditions which require that all tangential fields(E_z, H_z, E_l, and H_l) be continuous across the boundary surface, Γ. When the incident

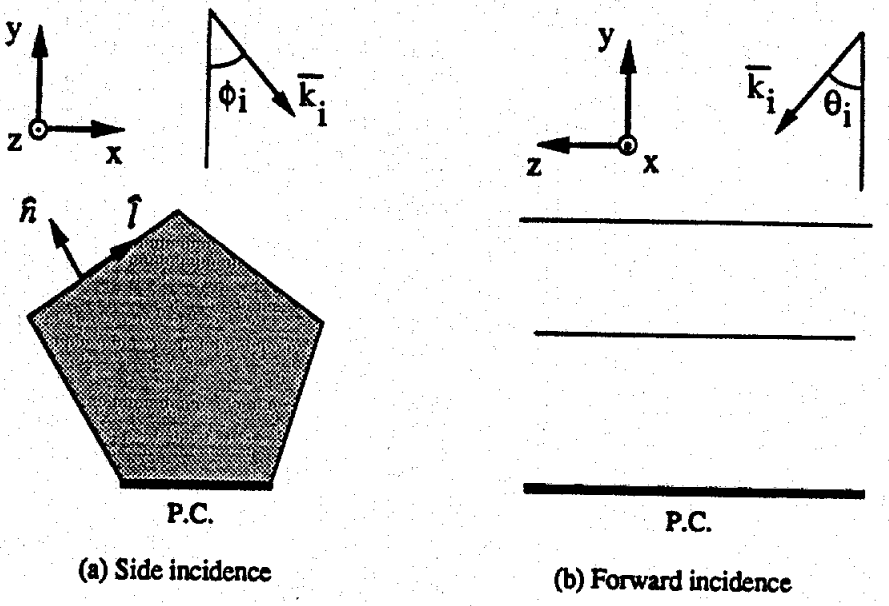

Figure 3.2: Incident wave configuration with respect to the geometry.

wave propagates perpendicularly to $\hat{z}$ (side incidence), E- or H-polarization is defined in a conventional way in which either E_z or H_z exists. We choose E_z and H_l $(= \frac{1}{\mu}\frac{\partial E_z}{\partial n})$ for E-polarization, and H_z and E_l $(= \frac{1}{\epsilon}\frac{\partial H_z}{\partial n})$ for H-polarization to be continuous(boundary conditions) at the dielectric/air boundary. By combining Eqs.(3.1) and (3.2) (for E-polarization) and Eqs.(3.3) and (3.4) (for H-polarization) with the boundary conditions, we obtain two decoupled integral equations for both polarizations.

However, when the propagation vector of the incident wave has a nonzero $\hat{z}$ component and a zero $\hat{x}$ component (forward incidence), both E_z and H_z exist at the same time. In this case, it is preferred to enforce all tangential fields to be continuous on the dielectric-air boundary for the purpose of formulation even though some fields are related through Maxwell's equations. The transverse tangential fields, E_l and H_l,

can be written in terms of $\hat{z}$ component of fields, E_z and H_z, as

$$E_l = \frac{-jk_z}{k^2 - k_z^2}\left(\frac{\partial E_z}{\partial l} + \frac{\omega\mu}{k_z}\frac{\partial H_z}{\partial n}\right) \tag{3.5}$$

$$H_l = \frac{-jk_z}{k^2 - k_z^2}\left(\frac{\partial H_z}{\partial l} - \frac{\omega\epsilon}{k_z}\frac{\partial E_z}{\partial n}\right) \tag{3.6}$$

where $\hat{l}$ and $\hat{n}$ denote the unit transverse tangential and outward normal vectors on the boundary surface, respectively, as shown in Figure 3.2. On the conducting boundary surface, the tangential electric fields, E_z and E_l, and the normal magnetic field, H_n, are zero or from Eq.(3.5)

$$E_z = E_l = \frac{\partial}{\partial n}H_z = 0$$

By enforcing these boundary conditions on Eqs.(3.1) through (3.4), two coupled integral equations for E_z and H_z are obtained as

$$\begin{aligned}
&\int_\Omega \frac{k_0^2 k^2}{k^2 - k_z^2}\left(\epsilon_r - \frac{1}{\mu_r}\right)E_z(\vec{r'})G_0 dV' + \int_{\Gamma_c}\frac{k^2}{\mu_r(k^2 - k_z^2)}G_0\frac{\partial E_z(\vec{r'})}{\partial n_c'}dS' \\
+ &\int_{\Gamma_d}\frac{k_z(k_0^2 - k^2)\omega\mu_0}{(k^2 - k_z^2)(k_0^2 - k_z^2)}G_0\frac{\partial H_z(\vec{r'})}{\partial l'} + \left(\frac{k_0^2}{k_0^2 - k_z^2} - \frac{k^2}{\mu_r(k^2 - k_z^2)}\right)E_z(\vec{r'})\frac{\partial G_0}{\partial n'}dS' \\
= &\frac{k_0^2}{k_0^2 - k_z^2}E_z^{inc} + \begin{cases} \frac{k^2}{(k^2 - k_z^2)\mu_r}E_z(\vec{r}) & \vec{r} \text{ inside dielectric} \\ \frac{k_0^2}{(k_0^2 - k_z^2)}E_z(\vec{r}) & \vec{r} \text{ outside dielectric} \\ \frac{1}{2}\left(\frac{k^2}{(k^2 - k_z^2)\mu_r} + \frac{k_0^2}{(k_0^2 - k_z^2)}\right)E_z(\vec{r}) & \vec{r} \text{ on } \Gamma_d \\ 0 & \vec{r} \text{ on } \Gamma_c \end{cases}
\end{aligned} \tag{3.7}$$

$$\begin{aligned}
&\int_\Omega \frac{k_0^2 k^2}{k^2 - k_z^2}\left(\mu_r - \frac{1}{\epsilon_r}\right)H_z(\vec{r'})G_0 dV' - \int_{\Gamma_c}\frac{k^2}{\epsilon_r(k^2 - k_z^2)}H_z(\vec{r'})\frac{\partial G_0}{\partial n_c'}]dS' \\
+ &\int_{\Gamma_d}\frac{k_z(k_0^2 - k^2)\omega\epsilon_0}{(k^2 - k_z^2)(k_0^2 - k_z^2)}G_0\frac{\partial E_z(\vec{r'})}{\partial l'} + \left(\frac{k_0^2}{k_0^2 - k_z^2} - \frac{k^2}{\epsilon_r(k^2 - k_z^2)}\right)H_z(\vec{r'})\frac{\partial G_0}{\partial n'}dS' \\
= &\frac{k_0^2}{k_0^2 - k_z^2}H^{inc} + \begin{cases} \frac{k^2}{(k^2 - k_z^2)\epsilon_r}H_z(\vec{r}) & \vec{r} \text{ inside dielectric} \\ \frac{k_0^2}{(k_0^2 - k_z^2)}H_z(\vec{r}) & \vec{r} \text{ outside dielectric} \\ \frac{1}{2}\left(\frac{k^2}{(k^2 - k_z^2)\epsilon_r} + \frac{k_0^2}{(k_0^2 - k_z^2)}\right)H_z(\vec{r}) & \vec{r} \text{ on } \Gamma_d \\ \frac{k_0^2}{(k_0^2 - k_z^2)}H_z(\vec{r}) & \vec{r} \text{ on } \Gamma_c \end{cases}
\end{aligned} \tag{3.8}$$

where $\Gamma = \Gamma_d + \Gamma_c$, and Γ_d denotes the dielectric/free space interface and Γ_c the dielectric/perfect conductor interface. The integral over Γ can be evaluated using the Cauchy principal value integral to remove the singular point, $\vec{r} = \vec{r'}$, from the integration[55].

This formulation for E_z and H_z may yield unreliable results when $|k^2 - k_z^2|$ is zero as is noted in [54]. When the value of $|k^2 - k_z^2|$ is very small, but not exactly zero, the numerical solution of the above equations may not be stable. The trouble can be overcome by multiplying both sides of Eqs.(3.7) and (3.8) by $(k^2 - k_z^2)$. Another way to avoid this difficulty is to formulate the equations in terms of transverse fields, that is, $E_x - E_y$ or $H_x - H_y$ as was done in [54].

In this formulation, the coupled terms appear because both $\vec{E}$ and $\vec{H}$ have a nonzero axial component when the incident wave is forward. The nonzero axial component of a magnetic (or electric) field induces an axial surface electric (or magnetic) current on the dielectric surfaces. The equivalent electric current for a scattered field due to the existance of the axial component of magnetic field in Eq.(3.7) is

$$J_z = -jk_z \frac{k^2 - k_0^2}{k_0^2(k^2 - k_z^2)} \frac{\partial H_z}{\partial l}$$

and the scattered field due to the equivalent current is

$$E_z = -j\omega\mu_0 \int_\Gamma J_z G_0 dS'$$

A similar interpretation can be made for the coupled term of Eq.(3.8) with the equivalent magnetic current.

For the case of side incidence, the coupled terms disappear because H_z is zero in Eq.(3.7) and E_z is zero in Eq.(3.8). In other words, k_z is zero for the side incidence, and hence, the coupling terms of Eqs.(3.7) and (3.8) are zero. The physical interpretations for the other terms of Eqs.(3.7) and (3.8) are corresponding to those of

Eq.(13) in [53].

Since the dielectric medium has an infinite dimension in both the $\hat{x}$ and $\hat{z}$ axes, the volume and the surface integrals in Eqs.(3.7) and (3.8) should be evaluated over infinite intervals. The infinite integrations in the $\hat{x}$ direction, however, can be reduced to the infinite summations of integrals over one period interval by taking advantage of the periodicity. Also, the infinite integration in the $\hat{z}$ direction can be performed analytically by exploiting the cylindrical geometry. With periodic properties of fields, the $\hat{z}$ component of electric or magnetic fields, $F(\vec{r})$, can be written at any point as

$$F(x+mP,y,z) = F(x,y,0)exp(-jk_{xi}mP)exp(-jk_{xi}z) \tag{3.9}$$

where m is an arbitrary integer and P is the period. The free space Green function, $G_0(\vec{r},\vec{r'})$, can be expanded as an integration of plane waves as

$$\begin{aligned} G_0(\vec{r},\vec{r'}) &= exp(-jk\left|\vec{r}-\vec{r'}\right|)/4\pi\left|\vec{r}-\vec{r'}\right| \\ &= \frac{-j}{8\pi^2}\int_{-\infty}^{\infty}\int_{-\infty}^{\infty} dk_x dk_z \cdot \\ &\quad exp[-j\{k_y^{\pm}(y-y')+k_x(x-x')+k_z(z-z')\}]/k_y^{+} \end{aligned} \tag{3.10}$$

where

$$k_y^{\pm} = \begin{cases} k_y^{+} & \text{for } y > y' \\ k_y^{-} & \text{for } y < y' \end{cases}$$

and

$$k_y^{+} = -k_y^{-} = \begin{cases} -j\sqrt{k_x^2+k_z^2-k^2} & \text{for } k < \sqrt{k_x^2+k_z^2} \\ \sqrt{k^2-k_x^2-k_z^2} & \text{for } k > \sqrt{k_x^2+k_z^2} \end{cases}$$

Using Eqs.(3.9) and (3.10) with the following relations

$$\begin{aligned} \sum_{m=-\infty}^{\infty} exp\{-jm(k_{xi}-k_x)P\} &= \sum_{n=-\infty}^{\infty}\frac{2\pi}{P}\delta(k_x-k_{xi}-\frac{2n\pi}{P}) \\ \int_{-\infty}^{\infty} exp\{-jz(k_{xi}-k_z)\}dz &= 2\pi\delta(k_{xi}-k_z) \end{aligned}$$

Eqs.(3.7) and (3.8) can be rewritten as

$$\begin{aligned}
&\frac{k_0^2k^2}{k^2-k_z^2}(\epsilon_r-\frac{1}{\mu_r})I^1_{E_z}+\frac{k^2}{\mu_r(k^2-k_z^2)}I^2_{\frac{\partial E_z}{\partial n}}\\
&+\frac{k_z(k_0^2-k^2)\omega\mu_0}{(k^2-k_z^2)(k_0^2-k_z^2)}I^2_{\frac{\partial H_z}{\partial l}}+(\frac{k_0^2}{k_0^2-k_z^2}-\frac{k^2}{\mu_r(k^2-k_z^2)})I^3_{E_z}\\
&=\frac{k_0^2}{k_0^2-k_z^2}E_z^{inc}+\begin{cases}\frac{k^2}{(k^2-k_z^2)\mu_r}E_z(\vec{r}) & \vec{r}\text{ inside dielectric}\\ \frac{k_0^2}{(k_0^2-k_z^2)}E_z(\vec{r}) & \vec{r}\text{ outside dielectric}\\ \frac{1}{2}(\frac{k^2}{(k^2-k_z^2)\mu_r}+\frac{k_0^2}{(k_0^2-k_z^2)})E_z(\vec{r}) & \vec{r}\text{ on }\Gamma_d\\ 0 & \vec{r}\text{ on }\Gamma_c\end{cases}
\end{aligned}\tag{3.11}$$

$$\begin{aligned}
&\frac{k_0^2k^2}{k^2-k_z^2}(\mu_r-\frac{1}{\epsilon_r})I^1_{H_z}-\frac{k^2}{\epsilon_r(k^2-k_z^2)})I^3_{H_z}\\
&+\frac{k_z(k_0^2-k^2)\omega\epsilon_0}{(k^2-k_z^2)(k_0^2-k_z^2)}I^2_{\frac{\partial E_z}{\partial l}}+(\frac{k_0^2}{k_0^2-k_z^2}-\frac{k^2}{\epsilon_r(k^2-k_z^2)})I^3_{H_z}\\
&=\frac{k_0^2}{k_0^2-k_z^2}H_z^{inc}+\begin{cases}\frac{k^2}{(k^2-k_z^2)\epsilon_r}H_z(\vec{r}) & \vec{r}\text{ inside dielectric}\\ \frac{k_0^2}{(k_0^2-k_z^2)}H_z(\vec{r}) & \vec{r}\text{ outside dielectric}\\ \frac{1}{2}(\frac{k^2}{(k^2-k_z^2)\epsilon_r}+\frac{k_0^2}{(k_0^2-k_z^2)})H_z(\vec{r}) & \vec{r}\text{ on }\Gamma_d\\ \frac{k_0^2}{(k_0^2-k_z^2)}H_z(\vec{r}) & \vec{r}\text{ on }\Gamma_c\end{cases}
\end{aligned}\tag{3.12}$$

where

$$\begin{aligned}
I^1_A &= \frac{-j}{2P}\sum_{m=-\infty}^{\infty}\int\int_{S_P}A(x',y')\frac{exp\{-j[k_y(y-y')+k_x(x-x')+k_zz]\}}{k_y^+}dx'dy'\\
I^2_A &= \frac{1}{2P}\sum_{m=-\infty}^{\infty}\int_{l_P}A(x',y')(n_xk_x+n_yk_y)\frac{exp\{-j[k_y(y-y')+k_x(x-x')+k_zz]\}}{k_y^+}dl'\\
I^3_A &= \frac{-j}{2P}\sum_{m=-\infty}^{\infty}\int_{l_P}A(x',y')\frac{exp\{-j[k_y(y-y')+k_x(x-x')+k_zz]\}}{k_y^+}dl'
\end{aligned}$$

and

$$\begin{aligned}
k_x &= k_{xi}+\frac{2m\pi}{P}\\
k_z &= k_{xi}\\
\hat{n} &= n_x\hat{x}+n_y\hat{y}
\end{aligned}$$

In the above, S_P denotes the cross section area of the periodic cell and l_P denotes a boundary line of the cross section of the cell. The function $A(x', y')$ represents $H_z(\vec{r})$, $E_z(\vec{r})$ or their derivatives with respect to l or n indicated by the subscript of I. Also, m represents the m^{th} order of Floquet mode. The 0^{th} Floquet mode corresponds to the specularly reflected or transmitted wave. The modes corresponding to m, such that $k < \sqrt{k_x^2 + k_z^2}$, are evanescent modes that decay exponentially in the $\hat{y}$ direction.

As shown in Eqs.(3.11) and (3.12), the infinite volume and the surface integrations are reduced to the infinite summations of the surface and the line integrations over one period, respectively. While the infinite integrations of Eqs.(3.7) and (3.8) converge slowly, the infinite summations of the above I's converge fast. Some algebraic manipulations after dividing the summation into two cases, when $m = 0$ and $m \neq 0$, give the following forms that converge more fast.

$$
\begin{aligned}
I_A^1 &= \frac{-j}{2P}\int\int_{S_P} A(x',y')[\frac{1}{k_0 cos\theta_i} exp\{-j[k_0 sin\theta_i(x-x') + k_0 cos\theta_i|y-y'| + k_z z]\} \\
&+ \frac{-P}{8\pi} ln\{[1 - exp(-j\frac{2\pi}{P}(x-x') - \frac{2\pi}{P}|y-y'|)] \\
&\cdot [1 - exp(j\frac{2\pi}{P}(x-x') - \frac{2\pi}{P}|y-y'|)]\} \\
&+ \sum_{m=1}^{\infty}\{exp[-j\{(\frac{2m\pi}{P} + k_0 sin\theta_i)(x-x') + k_y^+(y-y')\}]/k_y^+ \\
&- \frac{jP}{2m\pi} exp[-j\{\frac{2m\pi}{P}(x-x') - j\frac{2m\pi}{P}|y-y'|\}] \\
&+ exp[-j\{(\frac{-2m\pi}{P} + k_0 sin\theta_i)(x-x') + k_y^-(y-y')\}]/k_y^- \\
&- \frac{jP}{2m\pi} exp[-j\{\frac{-2m\pi}{P}(x-x') - j\frac{2m\pi}{P}|y-y'|\}]\}]dx'dy'
\end{aligned}
$$

$$
\begin{aligned}
I_A^2 &= \frac{-1}{2P}\int A(x',y')[\frac{f'(x')k_0 sin\theta_i - k_0 cos\theta_i sgn(y-y')}{k_0 cos\theta_i} \\
&\cdot exp\{-j[k_0 sin\theta_i(x-x') + k_0 cos\theta_i|y-y'| + k_z z]\} \\
&- \frac{1}{2}\{[f'(x') + jsgn(y-y')]cot\{\frac{-\pi[(x-x') - j|y-y'|]}{P}\} \\
&+ [-f'(x') + jsgn(y-y')]cot\{\frac{\pi[(x-x') + j|y-y'|]}{P}\} - 2sgn(y-y')\}
\end{aligned}
$$

$$
\begin{aligned}
&+ \sum_{m=1}^{\infty}\{f'(x')(\frac{2m\pi}{P}+k_0sin\theta_i)exp[-j\{(\frac{2m\pi}{P}+k_0sin\theta_i)(x-x')+k_y^+(y-y')\}]/k_y^+ \\
&- jf'(x')exp[-j\{\frac{2m\pi}{P}(x-x')-j\frac{2m\pi}{P}|y-y'|\}] \\
&- sgn(y-y')exp[-j\{(\frac{2m\pi}{P}+k_0sin\theta_i)(x-x')+k_y^+(y-y')\}] \\
&+ sgn(y-y')exp[-j\{\frac{2m\pi}{P}(x-x')-j\frac{2m\pi}{P}(y-y')\}]\} \\
&+ \sum_{m=1}^{\infty}\{f'(x')(\frac{-2m\pi}{P}+k_0sin\theta_i)exp[-j\{(\frac{-2m\pi}{P}+k_0sin\theta_i)(x-x')+k_y^-(y-y')\}]/k_y^- \\
&+ jf'(x')exp[j\{\frac{2m\pi}{P}(x-x')+j\frac{2m\pi}{P}|y-y'|\}] \\
&- sgn(y-y')exp[-j\{(\frac{-2m\pi}{P}+k_0sin\theta_i)(x-x')+k_y^-(y-y')\}] \\
&+ sgn(y-y')exp[-j\{\frac{-2m\pi}{P}(x-x')-j\frac{2m\pi}{P}(y-y')\}]\}]dx'
\end{aligned}
$$

$$
\begin{aligned}
I_A^3 \;=\; & \frac{-j}{2P}\int A(x',y')[\frac{1}{k_0cos\theta_i}exp\{-j[k_0sin\theta_i(x-x')+k_0cos\theta_i|y-y'|+k_zz]\} \\
&+ \frac{-P}{8\pi}ln\{[1-exp(-j\frac{2\pi}{P}(x-x')-\frac{2\pi}{P}|y-y'|)] \\
&\cdot [1-exp(j\frac{2\pi}{P}(x-x')-\frac{2\pi}{P}|y-y'|)]\} \\
&+ \sum_{m=1}^{\infty}\{exp[-j\{(\frac{2m\pi}{P}+k_0sin\theta_i)(x-x')+k_y^+(y-y')\}]/k_y^+ \\
&- \frac{jP}{2m\pi}exp[-j\{\frac{2m\pi}{P}(x-x')-j\frac{2m\pi}{P}|y-y'|\}] \\
&+ exp[-j\{(\frac{-2m\pi}{P}+k_0sin\theta_i)(x-x')+k_y^-(y-y')\}]/k_y^- \\
&- \frac{jP}{2m\pi}exp[-j\{\frac{-2m\pi}{P}(x-x')-j\frac{2m\pi}{P}|y-y'|\}]\}\sqrt{1+f'(x')^2}]dx'
\end{aligned}
$$

In the above expressions, $f'(x)$ represents a derivative of a boundary surface function with respect to x. The $sgn(y-y')$ denotes $+1$ if $y \geq y'$ and -1 if $y < y'$.

For the half space problem, Eqs.(3.7) and (3.8) can be simplified and solved analytically to obtain the reflectivity and the transmittivity. The periodic structures in both $\hat{x}$ and $\hat{z}$ directions can also be formulated in a similar manner, but are not considered in this thesis.

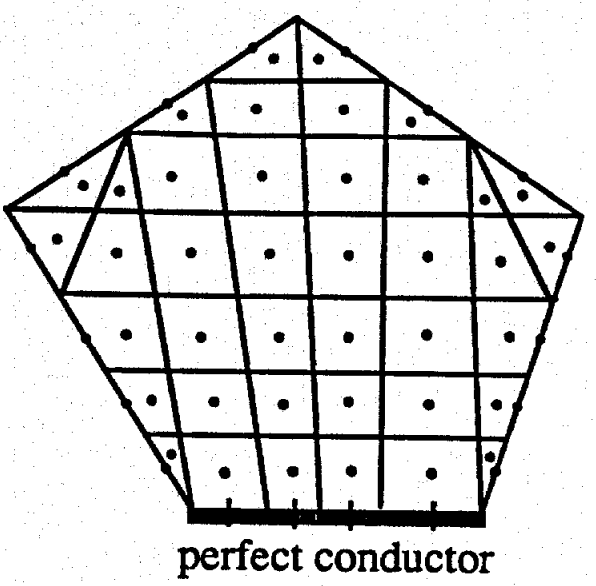

Figure 3.3: Cross section discretization of cylindrical structure over one period.

3.3 Numerical Procedure

The resultant integral equations over one period of Eqs.(3.11) and (3.12) are solved numerically using the point matching technique. In order to apply this technique, the dielectric region and the boundary lines are discretized into N cells as shown in Figure 3.3. The cells are plane segments inside the dielectric medium and line segments on the boundary. Next, we can approximate the unknown field in terms of a set of pulse functions. For the field inside the dielectric, we write

$$F_z(\vec{r}) = \sum_{i=1}^{N} F_i P_i$$

where P_i is a pulse function being one in i^{th} cell and zero elsewhere, and F_i is an unknown coefficient. Similarly, for the field of dielectric/free-space boundary,

$$F_z(\vec{r}) = \sum_{i=1}^{M} F_i P_i$$

and for the field of dielectric/conductor boundary,

$$F_z(\vec{r}) = \sum_{i=1}^{L} F_i P_i$$

Here, N, M and L denote the total number of segments inside, on the dielectric/free space boundary, and on the dielectric/conductor boundary, respectively. The normal derivative of the field, which appears in the second integral of Eq.(3.11), is also considered as an unknown field and is expanded as

$$\frac{\partial F}{\partial n_c} = \sum_{i=1}^{L} K_i P_i$$

where K_i is an unknown coefficient as was done in [55]. Note that when a normal derivative of an unknown field is considered as a variable, the field itself need not be considered as a variable. The derivative of field with respect to $\hat{l}$ can be approximated as

$$\frac{\partial F}{\partial l} = (F(r_{j+1}) - F(r_{j+1}))/(r_{j+1} - r_{j-1})$$

at r_j where r_{j+1} and r_{j-1} are centers of adjacent line segments of r_j at the dielectric/free-space boundary. Every segment, therefore, has two unknowns: E_z and H_z or $\partial E_z/\partial n'$ and H_z.

With these pulse expansions of the field, there are $2(N + M + L)$ linearly independent equations with $2(N + M + L)$ variables from Eqs.(3.11) and (3.12). These linear equations are then solved using a matrix inversion process.

After solving for the fields in the dielectric medium and on the conductor, the fields are computed at any point of free space using Eqs.(3.11) and (3.12). The fields that are scattered by truncated periodic wedges are obtained using an array factor, AF, which is written as

$$|AF(\phi)| = \left| \frac{sin\{\frac{N_t P}{2}(k_{xi} + k_0 sin\phi)\}}{sin\{\frac{P}{2}(k_{xi} + k_0 sin\phi)\}} \right|$$

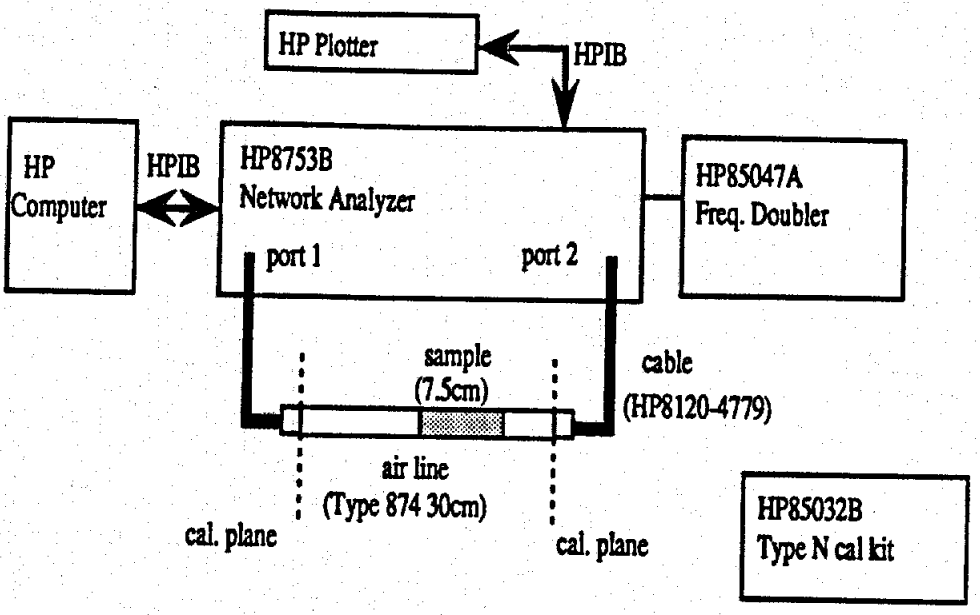

Figure 3.4: Dielectric constant measurement set up for microwave absorbing materials.

The scattering pattern is then given by

$$|A(\phi)| = |A_1(\phi)| \cdot |AF|$$

where N_t is a total number of wedges. In the above, $A_1(\phi)$ denotes the scattered electric or magnetic field computed over one period.

3.4 Dielectric Constant Measurement

To provide realistic and practical results, the dielectric constants of the wedge samples were measured using a coaxial line measurement technique with a microwave Network Analyzer[56]. Figure 3.4 shows the equipment set up and instruments used. A full 2-port calibration[57] is performed at the calibration planes shown in the figure. This essentially eliminates the reflections from all the connectors except the air-line connectors. The reflections from the air-line connectors are eliminated using time

domain gating techniques. However, one should be careful when using the gating technique, since it may introduce errors, especially at lower frequencies[56].

The dielectric and magnetic constants are computed from measured values for S_{11} and S_{21} of a 50 ohm air line filled with the absorber sample. In short, the reflection coefficient, Γ, from the surface of the semi-infinite sample and the transmission coefficient, T, in the sample, are written in terms of measured $S_{11}(\omega)$ and $S_{21}(\omega)$ as

$$\begin{aligned} \Gamma &= K \pm \sqrt{K^2 - 1} \\ T &= \frac{S_{11}^2(\omega) - S_{21}^2(\omega) + 1}{1 - (S_{11}(\omega) - S_{21}(\omega))\Gamma} \end{aligned}$$

where

$$K = \frac{S_{11}^2(\omega) - S_{21}^2(\omega) + 1}{2S_{11}(\omega)}$$

Since Γ and T are [58]

$$\begin{aligned} \Gamma &= \frac{\sqrt{\frac{\mu_r}{\epsilon_r}} - 1}{\sqrt{\frac{\mu_r}{\epsilon_r}} + 1} \\ T &= exp(-j\omega\sqrt{\mu\epsilon}d) = exp(-j(\omega/c)\sqrt{\mu_r\epsilon_r}d) \end{aligned}$$

the dielectric and the magnetic constants are obtained as

$$\begin{aligned} \epsilon_r(\omega) &= (\frac{jc}{\omega d}\frac{1-\Gamma}{1+\Gamma}lnT)^2 \\ \mu_r(\omega) &= (\frac{jc}{\omega d}\frac{1+\Gamma}{1-\Gamma}lnT)^2 \end{aligned}$$

where c is light velocity and d is the physical sample length.

In these measurements, two samples were taken from a microwave range pyramidal absorber: (1) the upper part and (2) the lower part. The microwave absorber is the 8-inch wedge absorber used in the University of Michigan anechoic chamber. Figures 3.5(a) and (b) show the measured dielectric and magnetic constants of the sample as functions of frequency, respectively. Both samples give the same

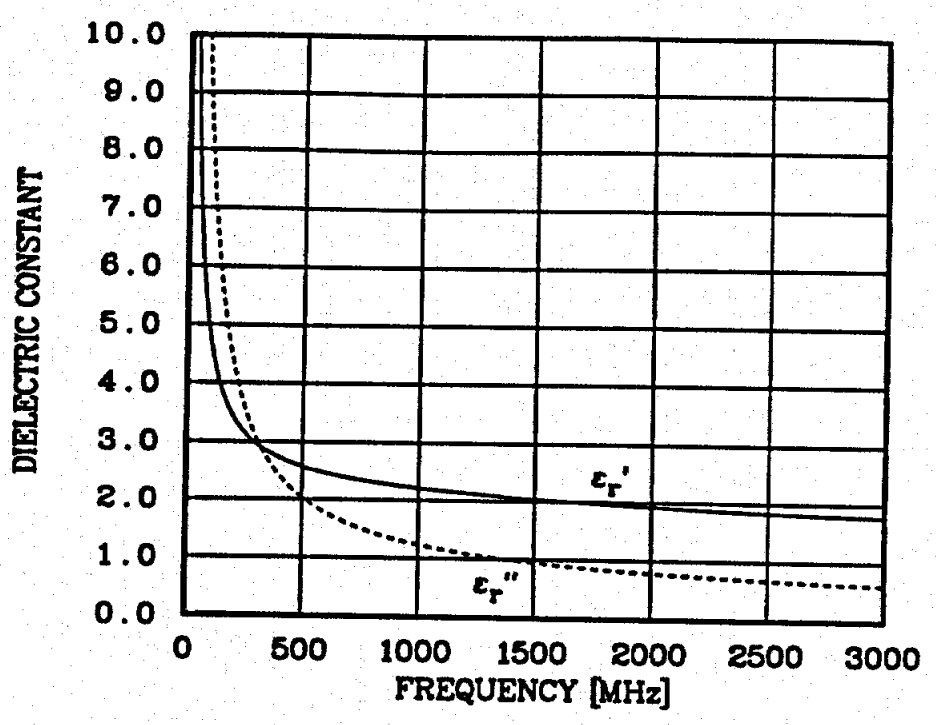

(a) dielectric constants.

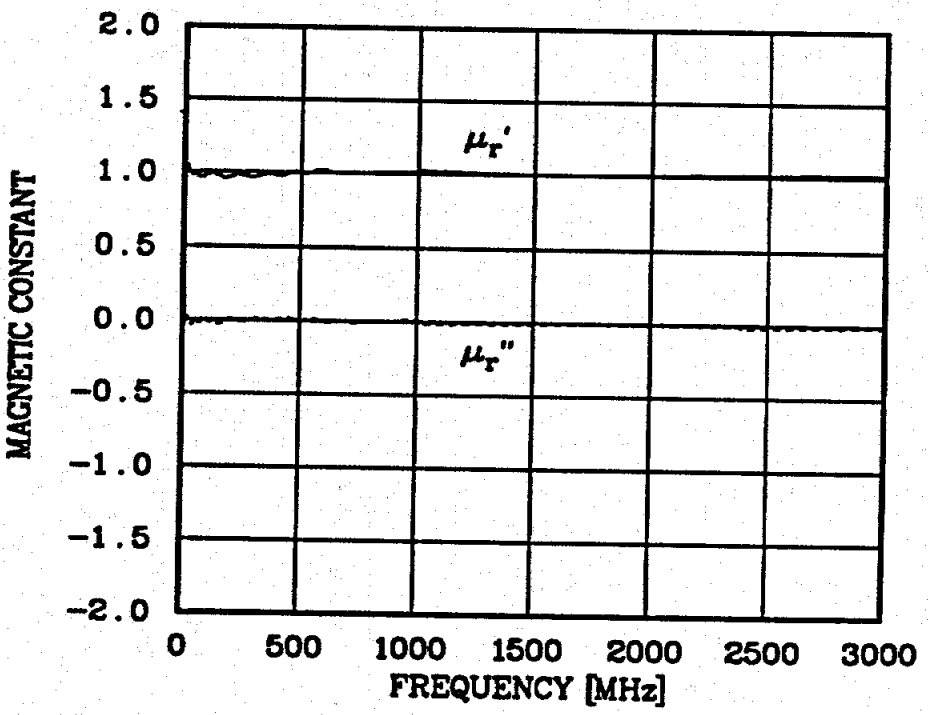

(b) magnetic constants.

Figure 3.5: Measured dielectric and magnetic constants of the wedge absorber.

results. As expected, the magnetic constants are almost $1. - j0.$ for all frequencies because the absorber consists of carbon and urethane foam and no magnetic materials. In addition, the measured dielectric constants have been verified through a cavity measurement[59],[60] for several frequency points.

3.5 Numerical Results

The computer code that was written based on the formulation given in sections 3.2 and 3.3 was checked by computing the reflection coefficient of a flat dielectric slab backed by a perfect conductor. The period of the flat slab can be chosen arbitrarilly and we chose 0.2 wavelength for the calculation. The number of nodes used in this analysis was at least 20 per one wavelength. The comparison of reflection coefficients for forward incidence and side incidence with analytical solutions is made in Figure 3.6. The plots (a) and (b) show the reflectivity for E-polarized and H-polarized cases, respectively. As is seen in the plots, the reflectivities computed with our code agree almost exactly with the analytical results.

Next, the algorithm was applied to the periodic lossy wedge absorber. The model of the wedge absorber is the one from the anechoic chamber of the University of Michigan. The cross section and the dimensions of the 8-inch wedge absorber are shown in Figure 3.7. The computed specular reflection coefficients of this wedge for forward incidence are shown in Figure 3.8. This figure shows that the wedge absorber is good above 1000 MHz with reflection coefficients less than -20 dB for both E and H-polarized incident waves up to 60 degrees of incidence angle. At 500 MHz, the absorber performance is only -10 dB. Figure 3.9 shows the scattered field pattern of the wedge absorber for normal incidence at 1 GHz.

For side incidence waves, the back scattering patterns of the wedge absorber are

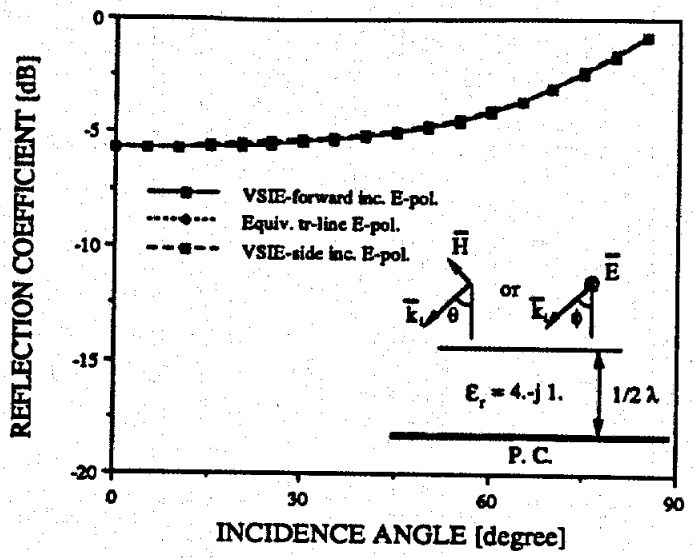

(a) E-polarization

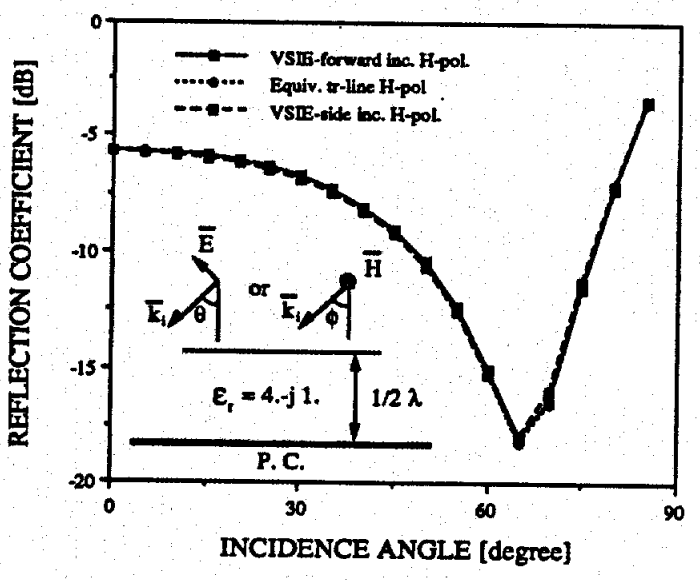

(b) H-polarization

Figure 3.6: Comparison of specular reflection coefficients of VSIE solution with those of equivalent transmission line solution.


θ_{wedge}
θ_{wedge}
25 cm
5 cm
y_1
y_2
y_3
y_4
y_5
y_6
y_7
y_8
y_9
y_{10}
y_{11}
y_{12}
y_{13}
y_{14}
y_{15}
y_{16}
y_{17}
y_{18}
y_{19}
y_{20}
y_{21}
y_{22}
y_{23}
y_{24}
y_{25}
y_{26}
y_{27}
y_{28}
y_{29}
y_{30}
y_{31}
y_{32}
y_{33}
y_{34}
y_{35}
y_{36}
y_{37}
y_{38}
y_{39}
y_{40}
y_{41}
y_{42}
y_{43}
y_{44}
y_{45}
y_{46}
y_{47}
y_{48}
y_{49}

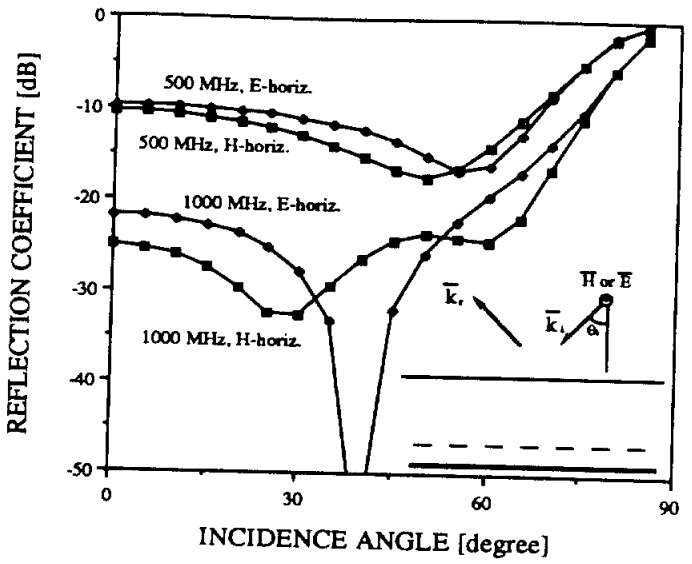

Figure 3.8: Specular reflection coefficient from periodic wedges for forward incident wave.

the effects of absorbers at high frequency do not need to be considered. Also, since the antenna wires are passing over the absorber horizontally, the currents on the wires are affected only by the horizontal electric field. (See Figure 3.11.) Therefore only the TE (or E-horizontal) incident waves are important to our purpose and were considered here. In Chapter V, the equivalent lossy layer that was obtained in this chapter will be used to simulate the absorber of an anechoic chamber.

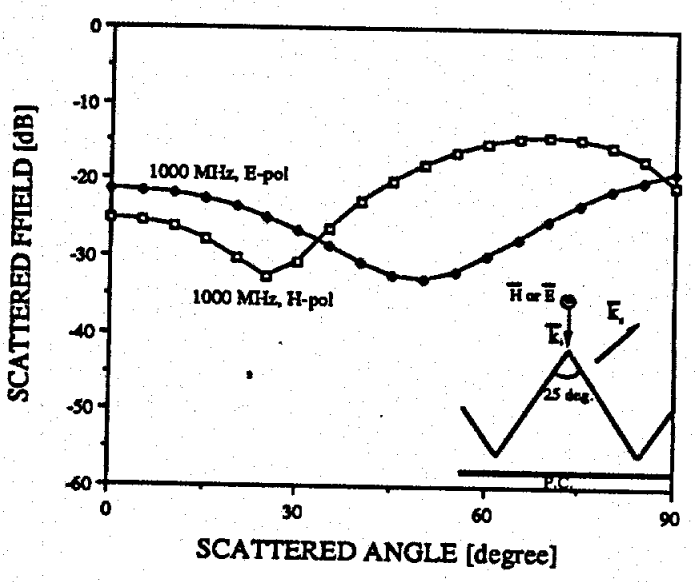

Figure 3.9: Bistatic scattering pattern of a unit cell for normal incidence.

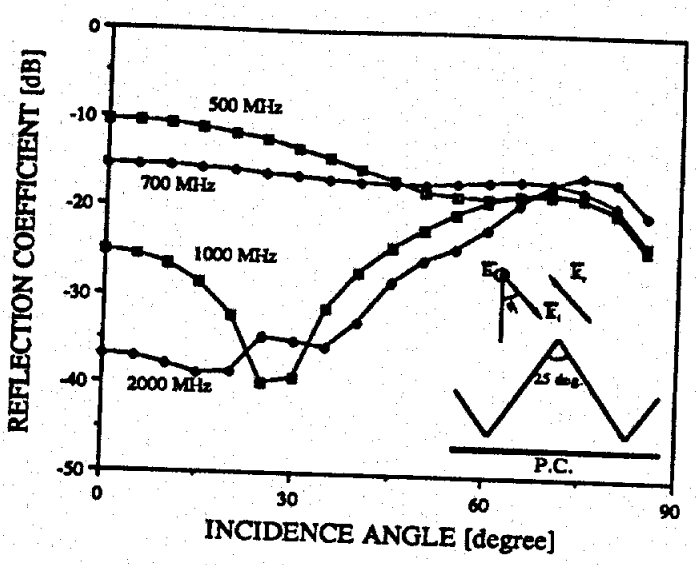

(a) E-polarization

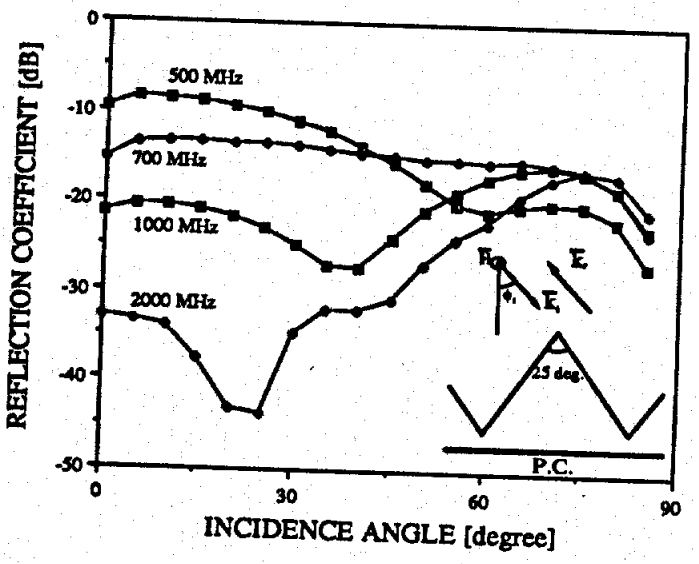

(b) H-polarization

Figure 3.10: Backscattering from a unit cell for side incidence.

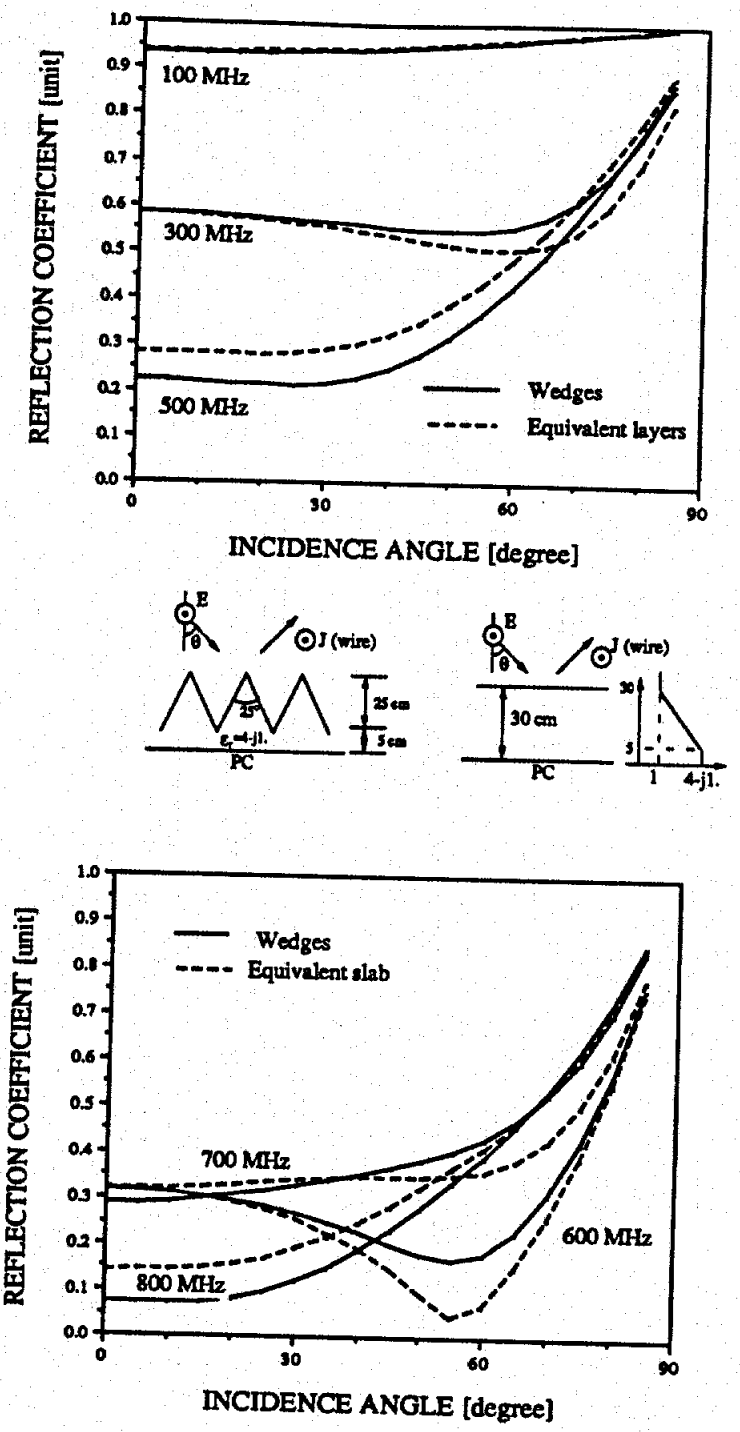

Figure 3.11: Comparison of specular reflection coefficients between the wedge absorber and equivalent layer backed by a conductor (E-horizontal).

CHAPTER IV

ANALYSIS OF DIPOLE ANTENNA NEAR LOSSY LAYERS

4.1 Introduction

To determine the effect of the anechoic chamber on the wire antenna, the dipole antenna above an absorbing layer is analyzed in this chapter. The lossy layer has linear dielectric constant profile with respect to its depth and is backed by a perfect conductor. This configuration is used to simulate the absorbing material and the shielded chamber walls. The analysis of the dipole antenna over a lossy layer is used to estimate how the absorbing material in the anechoic chamber affects the wire antennas.

The analysis of the dipole antenna over a lossy layer requires an appropriate Green's function. The Green's function that is applicable to a radiator over a uniform lossy half space ground was first introduced by A. Sommerfeld in 1909[61]-[63]. Since then, L. Brekhovskikh[62] has formulated the fields for a continuous one dimensional inhomogeneous half space using an adequate Riccatti Equation. J. Wait [63] and J. Kong [64] derived the fields due to dipole antennas over an isotropic and anisotropic stratified media, respectively, in a compact form using a propagation matrix.

When calculating the fields using the Green's function, one faces the problem

of evaluating the Sommerfeld type integral. This type of integral can not be evaluated analytically and it requires a huge amount of computing time for numerical integration. The fact that the integrand has poles and branch cuts makes the evaluation even more complicated. To overcome these difficulties, Miller et al.[65],[66] suggested the use of the plane wave reflection coefficient approximation(RCA) for a vertical and a horizontal dipole antenna located in free space near the interface with a lossy half space. This approximation provides results with accuracy within 10 percent for a vertical dipole and 20 percent for a horizontal dipole at approximately 1 percent of the computing time required by more rigorous computational approaches. Karwowski and Michalski[67] modified the RCA method by using the reflection coefficient in the evaluation of the magnetic vector potential rather than the electric field of the dipole. The modified RCA gives more accurate results than the original one when the antenna is close to the interface. Parhami et al. [68], Michalski[69], and Michalski et al.[70] evaluated the Sommerfeld integral numerically along the steepest descent path passing through the saddle point, as is done in the asymptotic approximation of the integrals. When a branch point is captured in the process of the contour deformation, the branch cut path integration is added to the steepest descent path integral. Tsang et al.[71] formulated the fast Fourier transform algorithm to evaluate the integrals via proper decomposition of the integrand. Mohsen[72] suggested other possible decompositions of the integrand for the FFT algorithm. Katehi and Alexopoulos[73] developed an efficient analytic-numeric real axis integration technique for an embedded dipole in a dielectric slab. In this technique, they divided the integration interval into two ranges. The first interval, which is the main portion of the integral, is evaluated numerically and the second interval, which is the tail portion, is evaluated with the combination of numerical

and analytical integration. Lindell and Alanen[74],[75] presented an exact image theory for the Sommerfeld half space problem with vertical and horizontal current sources. Using the exact image, the fields can be calculated within 0.2 % error with computing time comparable to that of RCA. However, the exact image for a layered medium has not been found yet and is not applicable in our case.

In section 4.2, the Green's function is derived for an electric dipole over a stratified anisotropic medium backed by a perfect conductor by following Kong's approach. In section 4.3, the method of moments is applied to a thin wire antenna with the Green's function. The key to a successful application of the integral equation techniques for solving wire antenna problems involving the lossy half space is the effective and accurate computation of the Sommerfeld integral. The evaluation of the Sommerfeld integral is performed using the fast Fourier transform algorithm, which is one of the fastest and most exact methods. In section 4.4, the computation results for a vertical and a horizontal half wavelength dipole are presented.

4.2 Field Equation

The geometry of the problem under consideration is shown in Figure 4.1. The source is assumed to be located at the origin and the ground plane is layered with anisotropic media and backed by a perfect conductor. The Maxwell's equations in source free region are

$$\nabla \times \vec{E} = -j\omega\bar{\bar{\mu}} \cdot \vec{H} \tag{4.1}$$

$$\nabla \times \vec{H} = j\omega\bar{\bar{\epsilon}} \cdot \vec{E} \tag{4.2}$$

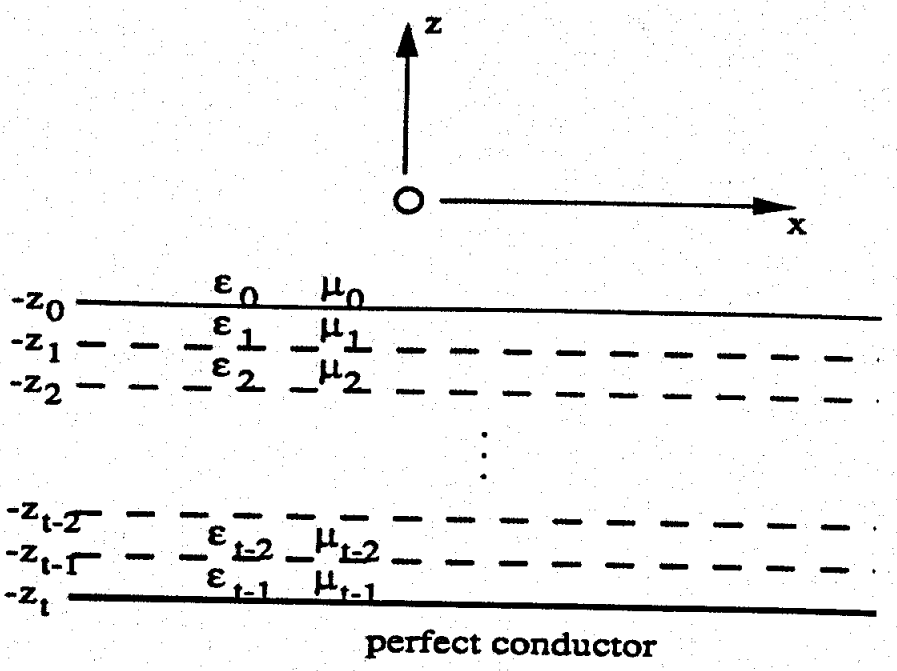

Figure 4.1: Geometry of the dipole over a layered slab backed by a conductor.

$$\bar{\bar{\epsilon}} = \begin{bmatrix} \epsilon & & \\ & \epsilon & \\ & & \epsilon_z \end{bmatrix} \tag{4.3}$$

$$\bar{\bar{\mu}} = \begin{bmatrix} \mu & & \\ & \mu & \\ & & \mu_z \end{bmatrix} \tag{4.4}$$

where $\bar{\bar{\mu}}$ and $\bar{\bar{\epsilon}}$ are uniaxial permeability and permittivity tensors, respectively.[1] The tensor $\bar{\bar{\epsilon}}$ contains information about the dielectric constant and the conductivity of the medium, that is , $\bar{\bar{\epsilon}} = \bar{\bar{\epsilon}}' - j\bar{\bar{\epsilon}}''$ where $\bar{\bar{\epsilon}}'' = \bar{\bar{\sigma}}/\omega$.

Employing cylindrical coordinates, (ρ, ϕ, z), the longitudinal electric and magnetic components, which are denoted by E_z and H_z, are used to derive TE and TM

[1]The tensor formulation has been introduced here for generality and later the tensors are replaced by scalars.

waves. By taking the $\hat{z}$ component of Eq.(4.2) in view of $\bar{\bar{\epsilon}}$ given by Eq.(4.3), employing Eq.(4.1) to eliminate transverse magnetic field components, and using the fact that $\nabla \cdot \vec{E} = (1-a)\partial E_z/\partial z$, the equation for the longitudinal component of the electric field is

$$(\nabla_t^2 + a\frac{\partial^2}{\partial z^2} + k^2 a)E_z = 0 \tag{4.5}$$

In the same manner, the wave equation for the magnetic field is

$$(\nabla_t^2 + b\frac{\partial^2}{\partial z^2} + k^2 b)H_z = 0 \tag{4.6}$$

In Eq.(4.5) and Eq.(4.6),

$$\begin{aligned} k &= \omega\sqrt{\mu\epsilon} \\ a &= \epsilon_z/\epsilon \\ b &= \mu_z/\mu \end{aligned}$$

and

$$\nabla_t^2 = \frac{1}{\rho}\frac{\partial}{\partial\rho}(\rho\frac{\partial}{\partial\rho}) + \frac{1}{\rho^2}\frac{\partial^2}{\partial\phi^2}$$

is the transverse Laplacian operator expressed in cylindrical coordinates. It is seen from Eq.(4.5) and Eq.(4.6) that E_z and H_z are decoupled, which would not be true if the $\bar{\bar{\mu}}$ and $\bar{\bar{\epsilon}}$ tensors contain off-diagonal elements. Thus a TM mode is derivable from E_z and a TE mode from H_z since the total waves can be decomposed uniquely into TE and TM modes. The transverse electric and magnetic components can be obtained in terms of the longitudinal components of the fields, E_z and H_z, which are characterized as TM and TE waves, respectively.

By introducing the plane wave expansion as

$$E_z^{TM} = \int_{-\infty}^{\infty} dk_\rho E_z(k_\rho)$$

and

$$H_z^{TE} = \int_{-\infty}^{\infty} dk_\rho H_z(k_\rho)$$

the transverse components are related to $E_z(k_\rho)$ and $H_z(k_\rho)$ by

$$E_t(k_\rho)^{TM} = \frac{1}{k_\rho^2}\nabla_t \frac{\partial E_z(k_\rho)}{\partial z}, \text{ and } H_t(k_\rho)^{TM} = j\frac{\omega\epsilon}{k_\rho^2}\nabla_t \times \hat{z}E_z(k_\rho)$$

$$H_t(k_\rho)^{TE} = \frac{1}{k_\rho^2}\nabla_t \frac{\partial H_z(k_\rho)}{\partial z}, \text{ and } E_t(k_\rho)^{TE} = -j\frac{\omega\mu}{k_\rho^2}\nabla_t \times \hat{z}H_z(k_\rho)$$

In cylindrical coordinates, the solutions of E_z and H_z to the wave equations, Eq.(4.5) and Eq.(4.6), are well known. By choosing the wave solutions which are outgoing in the $\hat{\rho}$ direction and traveling or standing in the $\hat{z}$ direction, the solutions in the i^{th} layer are constructed with a fixed separation constant, n, as,

$$E^{TM} = \int_{-\infty}^{\infty} dk_\rho \begin{bmatrix} j\frac{k_z^e}{k_\rho}(A_i e^{jk_z^e z} - B_i e^{-jk_z^e z})H_n^{(2)'}(k_\rho\rho)S_n^{TM}(\phi) \\ j\frac{k_z^e}{k_\rho^2\rho}(A_i e^{jk_z^e z} - B_i e^{-jk_z^e z})H_n^{(2)}(k_\rho\rho)S_n^{TM'}(\phi) \\ (A_i e^{jk_z^e z} + B_i e^{-jk_z^e z})H_n^{(2)}(k_\rho\rho)S_n^{TM}(\phi) \end{bmatrix} \quad (4.7)$$

$$H^{TM} = \int_{-\infty}^{\infty} dk_\rho \begin{bmatrix} j\frac{\omega\epsilon}{k_\rho^2\rho}(A_i e^{jk_z^e z} + B_i e^{-jk_z^e z})H_n^{(2)}(k_\rho\rho)S_n^{TM'}(\phi) \\ -j\frac{\omega\epsilon}{k_\rho}(A_i e^{jk_z^e z} + B_i e^{-jk_z^e z})H_n^{(2)'}(k_\rho\rho)S_n^{TM}(\phi) \\ 0 \end{bmatrix} \quad (4.8)$$

$$E^{TE} = \int_{-\infty}^{\infty} dk_\rho \begin{bmatrix} -j\frac{\omega\mu}{k_\rho^2}(C_i e^{jk_z^m z} + D_i e^{-jk_z^m z})H_n^{(2)}(k_\rho\rho)S_n^{TE'}(\phi) \\ j\frac{\omega\epsilon}{k_\rho}(C_i e^{jk_z^m z} + D_i e^{-jk_z^m z})H_n^{(2)'}(k_\rho\rho)S_n^{TE}(\phi) \\ 0 \end{bmatrix} \quad (4.9)$$

$$H^{TE} = \int_{-\infty}^{\infty} dk_\rho \begin{bmatrix} j\frac{k_z^m}{k_\rho}(C_i e^{jk_z^m z} - D_i e^{-jk_z^m z})H_n^{(2)'}(k_\rho\rho)S_n^{TE}(\phi) \\ j\frac{k_z^m}{k_\rho^2\rho}(C_i e^{jk_z^m z} - D_i e^{-jk_z^m z})H_n^{(2)}(k_\rho\rho)S_n^{TE'}(\phi) \\ (C_i e^{jk_z^m z} + D_i e^{-jk_z^m z})H_n^{(2)}(k_\rho\rho)S_n^{TE}(\phi) \end{bmatrix} \quad (4.10)$$

where

$$k_z^e = \sqrt{k^2 - k_\rho^2/a}$$

$$k_z^m = \sqrt{k^2 - k_\rho^2/b}$$

and each row element denotes the ρ, ϕ and z component, respectively. The $H_n^{(2)}$ is the n^{th} order Hankel function of the second kind. $S_n(\phi)$ stands for the sinusoidal function of ϕ and primes on $H_n^{(2)}(k_\rho \rho)$ and $S_n(\phi)$ denote differentiation with respect to their arguments. In Eqs.(4.7) through (4.10), the first term of each integrand can be considered as a direct field from the source, while the second term is a reflected field by the ground. The k_ρ dependent functions A_i, B_i, C_i, and D_i are to be determined by the appropriate boundary conditions.

The boundary conditions at all interfaces require all tangential electromagnetic field components to be continuous for all ρ and ϕ. For the TM waves these boundary conditions at the interface, z_i, are

$$k_{iz}^e\{A_i e^{-jk_{iz}^e z_i} - B_i e^{jk_{iz}^e z_i}\} = k_{(i+1)z}^e\{A_{i+1} e^{-jk_{(i+1)z}^e z_{i+1}} - B_{i+1} e^{jk_{(i+1)z}^e z_{i+1}}\} \quad (4.11)$$

$$\epsilon_i\{A_i e^{-jk_{iz}^e z_i} + B_i e^{jk_{iz}^e z_i}\} = \epsilon_{(i+1)}\{A_{i+1} e^{-jk_{(i+1)z}^e z_{i+1}} + B_{i+1} e^{jk_{(i+1)z}^e z_{i+1}}\} \quad (4.12)$$

By defining a_i and b_i as

$$a_i = A_i \exp(-jk_{iz}^e z_i) \text{ and } b_i = B_i \exp(jk_{iz}^e z_i),$$

the following propagation matrix equation can be derived from Eq.(4.11) and Eq.(4.12).

$$\begin{pmatrix} a_i \\ b_i \end{pmatrix} = M_i^{i+1} \begin{pmatrix} a_{i+1} \\ b_{i+1} \end{pmatrix} \quad (4.13)$$

where

$$M_i^{i+1} = \frac{1}{2}\begin{pmatrix} \epsilon(+)_i^{i+1} e(+)_i^e & \epsilon(-)_i^{i+1} e(-)_i^e \\ \epsilon(-)_i^{i+1} e(+)_i^e & \epsilon(+)_i^{i+1} e(-)_i^e \end{pmatrix}$$

$$\epsilon(\pm)_q^p = \left(\frac{\epsilon_p}{\epsilon_q} \pm \frac{k_{pz}^e}{k_{qz}^e}\right)$$

$$e(\pm)_i^e = \exp[\mp jk_{(i+1)z}^e (z_i - z_{i+1})]$$

$$k_{iz}^e = \sqrt{k_i^2 - k_\rho^2/a}$$

and the $\pm$ sign of k_z^e should be chosen so that the imaginary part of k_z^e is negative. Thus we can write

$$\begin{pmatrix} a_0 \\ b_0 \end{pmatrix} = M_0^1 M_1^2 \cdots M_{i-1}^i \begin{pmatrix} a_i \\ b_i \end{pmatrix} = \begin{pmatrix} M_{11} & M_{12} \\ M_{21} & M_{22} \end{pmatrix} \begin{pmatrix} a_i \\ b_i \end{pmatrix}$$

With R^{TM} representing the reflection coefficient at the interface between air and the slab or

$$a_0 = A_0 \exp(-jk_{0z}^e z_0) \text{ and } b_0 = R^{TM} A_0 \exp(jk_{0z}^e z_0)$$

the reflection coefficient is written as

$$\begin{aligned} R^{TM} &= \frac{B_0}{A_0} = \frac{b_0}{a_0} \exp(j2k_{0z}^e z_0) \\ &= \frac{M_{21} + M_{22} b_i/a_i}{M_{11} + M_{12} b_i/a_i} \exp(j2k_{0z}^e z_0) \end{aligned} \tag{4.14}$$

In the case of the lossy dielectric layers backed by a perfect conductor, $b_i/a_i = 1$ for TM wave.

The same procedure can be applied to the TE case with c_i and d_i which are defined as

$$c_i = C_i \exp(-jk_{iz}^m z_i) \text{ and } d_i = D_i \exp(jk_{iz}^m z_i)$$

and the following equations are obtained.

$$\begin{pmatrix} c_i \\ d_i \end{pmatrix} = N_i^{i+1} \begin{pmatrix} c_{i+1} \\ d_{i+1} \end{pmatrix} \tag{4.15}$$

where

$$\begin{aligned} N_i^{i+1} &= \frac{1}{2} \begin{pmatrix} \mu(+)_i^{i+1} e(+)_i^e & \mu(-)_i^{i+1} e(-)_i^e \\ \mu(-)_i^{i+1} e(+)_i^e & \mu(+)_i^{i+1} e(-)_i^e \end{pmatrix} \\ \mu(\pm)_q^p &= \left(\frac{\mu_p}{\mu_q} \pm \frac{k_{pz}^m}{k_{qz}^m}\right) \\ e(\pm)_i^e &= \exp\left[\mp jk_{(i+1)z}^m (z_i - z_{i+1})\right] \\ k_{iz}^m &= \sqrt{k_i^2 - k_\rho^2/b} \end{aligned}$$

and the reflection coefficient of TE wave, R^{TE}, is found as

$$\begin{aligned} R^{TE} &= \frac{D_0}{C_0} = \frac{d_0}{c_0}\exp(j2k_{0z}^m z_0) \\ &= \frac{N_{21} + N_{22}d_t/c_t}{N_{11} + N_{12}d_t/c_t}\exp(j2k_{0z}^m z_0) \end{aligned} \tag{4.16}$$

where

$$N_0^1 N_1^2 \cdots N_{t-1}^t = \begin{pmatrix} N_{11} & N_{12} \\ N_{21} & N_{22} \end{pmatrix}$$

and $d_t/c_t = -1$ for TE wave on the perfect conductor. Alternatively, the reflection coefficients can be obtained through an appropriate Riccati equation, which may be more accurate for a continuous dielectric profile [62]. Since the A_0 and B_0, and C_0 and D_0, are related via the reflection coefficients in Eqs.(4.14) and (4.16), once the magnitude of the direct fields, A_0 and C_0, are known, the reflected field can be obtained.

For a $\hat{z}$ directed dipole in a homogeneous space, the magnitudes of the $\hat{z}$ component of electric and magnetic fields, which are A_0 and C_0, are given as

$$A_0 = -\frac{Ilk_\rho^3}{8\pi\omega\epsilon k_z} \tag{4.17}$$

$$C_0 = 0 \tag{4.18}$$

using the relation

$$\frac{Il}{4\pi}\frac{\exp(-jkr)}{r} = \frac{-jIl}{8\pi}\int_{-\infty}^{\infty} dk_\rho \frac{k_\rho}{k_z^e} H_0^{(2)}(k_\rho\rho)e^{\pm jk_z z} \tag{4.19}$$

The vertical dipole, therefore, excites only TM modes since $C_0 = 0$. For a vertical dipole over a lossy medium, there is no ϕ dependence so that $S_n(\phi) = 1$, which means $n = 0$. With imposed radiation condition, the fields can be constructed as

$$E^{TM} = \int_{-\infty}^{\infty} dk_\rho \left(\frac{-Il}{8\pi\omega\epsilon}\right) \begin{bmatrix} -jk_\rho^2(e^{\pm jk_z^e z} + R^{TM}e^{-jk_z^e z})H_0^{(2)'}(k_\rho\rho) \\ 0 \\ \frac{k_\rho^3}{k_z^e}(e^{\pm jk_z^e z} + R^{TM}e^{-jk_z^e z})H_o^{(2)}(k_\rho\rho) \end{bmatrix} \tag{4.20}$$

$$H^{TM} = \int_{-\infty}^{\infty} dk_\rho \left(\frac{Il}{8\pi}\right) \begin{bmatrix} 0 \\ j\frac{k_\rho^2}{k_z^e}(e^{\pm jk_z^e z} + R^{TM}e^{-jk_z^e z})H_n^{(2)'}(k_\rho\rho) \\ 0 \end{bmatrix} \tag{4.21}$$

and $E^{TE} = H^{TE} = 0$.

For a horizontal ($\hat{x}$ directed) dipole in a homogeneous space, using the same relationship as in Eq.(4.19), one can show the magnitude of the $\hat{z}$ component electric field and magnetic fields, A_0 and C_0, to be

$$\begin{aligned} A_0 &= \pm j\frac{Ilk_\rho^2}{8\pi\omega\epsilon} \\ C_0 &= -j\frac{Ilk_\rho^2}{8\pi k_z} \\ S_1^{TM} &= \cos\phi \\ S_1^{TE} &= -\sin\phi \end{aligned}$$

For a $\hat{y}$ directed dipole, the field magnitudes can be obtained by simply changing the coordinates by 90 degrees. The horizontal dipole excites both TM and TE waves and the total fields are the sum of TM and TE fields. The fields are expressed from Eqs.(4.7) through (4.10) as

$$E^{TM} = \int_{-\infty}^{\infty} dk_\rho \left(\frac{Il}{8\pi\omega\epsilon}\right) \begin{bmatrix} jk_z^e k_\rho(e^{\pm jk_z^e z} - R^{TM}e^{-jk_z^e z})H_1^{(2)'}(k_\rho\rho)\cos\phi \\ \frac{k_z^e}{\rho}(e^{\pm jk_z^e z} - R^{TM}e^{-jk_z^e z})H_1^{(2)}(k_\rho\rho)\sin\phi \\ -k_\rho^2(\pm e^{\pm jk_z^e z} - R^{TM}e^{-jk_z^e z})H_1^{(2)}(k_\rho\rho)\cos\phi \end{bmatrix} \tag{4.22}$$

$$H^{TM} = \int_{-\infty}^{\infty} dk_\rho \left(\frac{Il}{8\pi}\right) \begin{bmatrix} -\frac{1}{\rho}(\pm e^{\pm jk_z^e z} - R^{TM}e^{-jk_z^e z})H_1^{(2)}(k_\rho\rho)\sin\phi \\ -k_\rho(\pm e^{\pm jk_z^e z} - R^{TM}e^{-jk_z^e z})H_1^{(2)'}(k_\rho\rho)\cos\phi \\ 0 \end{bmatrix} \tag{4.23}$$

$$E^{TE} = \int_{-\infty}^{\infty} dk_\rho \left(\frac{Il\omega\mu}{8\pi}\right) \begin{bmatrix} -\frac{1}{k_z^m \rho}(e^{\pm jk_z^m z} + R^{TE} e^{-jk_z^m z}) H_1^{(2)}(k_\rho \rho)\cos\phi \\ \frac{k_\rho}{k_z^m}(e^{\pm jk_z^m z} + R^{TE} e^{-jk_z^m z}) H_1^{(2)'}(k_\rho \rho)\sin\phi \\ 0 \end{bmatrix} \quad (4.24)$$

$$H^{TE} = \int_{-\infty}^{\infty} dk_\rho \left(j\frac{Il}{8\pi}\right) \begin{bmatrix} jk_\rho(\pm e^{\pm jk_z^m z} + R^{TE} e^{-jk_z^m z}) H_1^{(2)'}(k_\rho \rho)\sin\phi \\ j\frac{1}{\rho}(\pm e^{\pm jk_z^m z} + R^{TE} e^{-jk_z^m z}) H_1^{(2)}(k_\rho \rho)\cos\phi \\ -\frac{k_\rho^2}{k_z^m}(e^{jk_z^m z} + R^{TE} e^{-jk_z^m z}) H_1^{(2)}(k_\rho \rho)\sin\phi \end{bmatrix} \quad (4.25)$$

The $\pm$ signs in the above field equations is $+$ if $z < 0$ and $-$ if $z > 0$ so that the radiation condition is satisfied for the direct field.

4.3 Numerical Implementation and Evaluation of Sommerfeld Integral

In order to obtain the current distribution and the input impedance of the dipole antenna over lossy dielectric layers backed by a perfect conductor, the method of moment is used. As is well known, the electric field integral equation for a thin wire antenna is

$$E_w^s(r) = \int_l I(r')(G^d(r;r') + G^r(r;r'))dl' = -E_w^{inc}(r) \quad (4.26)$$

where superscript s and inc denote scattered and incident field, respectively. The subscript w is z for a $\hat{z}$ directed dipole, which will be called a vertical dipole, and x for an $\hat{x}$ directed dipole, which will be called a horizontal dipole. $I(r')$ is the current at r' and l is the length of the dipole. The kernels, $G^d(r;r')$ and $G^r(r;r')$, are Green's functions for direct and reflected waves, respectively. For a vertical dipole over an isotropic layered medium, the kernels are obtained from the $\hat{z}$ component of Eq.(4.20) as

$$G^d(r;r') = (k_0^2 + \frac{\partial^2}{\partial z^2})\frac{1}{4\pi\omega\epsilon_0 r}\exp(-jk_0 r)$$

$$G^r(r;r') = \int_0^\infty dk_\rho \frac{k_\rho^3}{4\pi\omega\epsilon k_z^e} R^{TM} \exp(-jk_z|z-z'|) J_0(k_\rho\rho)$$

For a horizontal dipole over an isotropic layered medium, the kernels are obtained from the $\hat{x}$ components of Eqs.(4.22) and (4.24) as

$$G^d(r;r') = (k_0^2 + \frac{\partial^2}{\partial x^2}) \frac{1}{4\pi\omega\epsilon_0 r} \exp(-jk_0 r) \tag{4.27}$$

$$G^r(r;r') = \int_0^\infty dk_\rho \frac{k_\rho k_z}{4\pi\omega\epsilon} \exp(-jk_z|z-z'|) \{R^{TM}[\frac{J_1(k_\rho\rho)}{k_\rho\rho} - J_0(k_\rho\rho)] + R^{TE} \frac{k^2}{k_\rho k_z^2 \rho} J_1(k_\rho\rho)\} \tag{4.28}$$

where

$$r = \sqrt{(x-x')^2 + (y-y')^2 + (z-z')^2}$$
$$\rho = \sqrt{(x-x')^2 + (y-y')^2}$$

In the above equations, $a = b = 1$ is imposed so that $k_z = k_z^e = k_z^m$.

Discretizing the dipole and applying the Galerkin's method with sinusoidal basis function for the current expansion, a set of linear equations are obtained from Eq.(4.26) as

$$\sum_{j=1}^{j=N} \left(a_{ij}^d + a_{ij}^r\right) I_j = b_i$$

where

$$a_{ij}^d = \int_{w_{i-1}}^{w_{i+1}} \int_{w_{j-1}}^{w_{j+1}} f_i(w) f_j(w') G^d(w;w') dw' dw \tag{4.29}$$
$$a_{ij}^r = \int_{w_{i-1}}^{w_{i+1}} \int_{w_{j-1}}^{w_{j+1}} f_i(w) f_j(w') G^r(w;w') dw' dw \tag{4.30}$$
$$b_i = \int_{w_{i-1}}^{w_{i+1}} f_i(w) E_w^i(w) dw \tag{4.31}$$

In the above, $i = 1, 2, \cdots, N$ where N is a total number of nodes. I_j denotes the current on the node j which will be solved for. The basis function, $f_n(w)$, is a

sinusoidal function and is defined as

$$f_n(w) = \begin{cases} \sin k_0(w - w_{n-1}) / \sin k_0(w_n - w_{n-1}) & \text{if } w_{n-1} < w < w_n \\ \sin k_0(w_{n+1} - w) / \sin k_0(w_{n+1} - w_n) & \text{if } w_n < w < w_{n+1} \\ 0 & \text{otherwise} \end{cases}$$

The coefficient elements for the direct field (Eq.(4.29)), and the forcing elements (Eq.(4.31)), can be evaluated as is done in the usual method of moment technique[76]. However, the evaluation of a reflected field coefficient element (Eq.(4.30)), is quite complicated and requires a huge amount of computing time since the kernel for the reflected wave includes another infinite integral. When evaluating a^r_{ij} for the case of a vertical dipole(TM), one obtains the following form by changing the order of integration.

$$a^r_{ij} = \int_0^\infty J_0(k_\rho \rho) K_{ij}(k_\rho) dk_\rho \tag{4.32}$$

where

$$K_{ij}(k_\rho) = \frac{-jk_\rho^3}{4\pi\omega\epsilon k_z} R^{TM} \int_{z_{i-1}}^{z_{i+1}} \int_{z_{j-1}}^{z_{j+1}} f_i(z) f_j(z') \exp(-jk_z|z - z'|) dz' dz.$$

When evaluating the integral of Eq.(4.32) using an FFT algorithm, both sides of Eq.(4.32) are multiplied by $exp(\nu_R k_\rho) exp(-\nu_R k_\rho)$ to obtain

$$a^r_{ij} = \int_0^\infty T_{ij}(k_\rho) exp(-\nu_R k_\rho) J_0(k_\rho \rho) dk_\rho \tag{4.33}$$

where $T_{ij}(k_\rho) = K_{ij}(k_\rho) exp(\nu_R k_\rho)$. By introducing the discrete Fourier transform of $T_{ij}(k_\rho)$ as

$$\begin{aligned} T_{ij}(k_\rho) &= \frac{1}{M\Delta k_\rho} \sum_{m=-M/2}^{M/2-1} t_{ij}(f_n) \exp(-j2\pi f_n k_\rho) \\ t_{ij}(f) &= \int_{-\infty}^{\infty} T_{ij}(k_\rho) \exp(j2\pi f_n k_\rho) dk_\rho, \end{aligned} \tag{4.34}$$

where $\Delta k_\rho \simeq 1/2F$, and F is the Nyquist frequency[77], Eq.(4.33) becomes

$$\begin{aligned} a_{ij}^r &= \frac{1}{M\Delta k_\rho} \sum_{m=-M/2}^{M/2-1} t_{ij}(f_n) \int_0^\infty exp(-\nu_R k_\rho) J_0(k_\rho \rho) dk_\rho \\ &= \frac{1}{M\Delta k_\rho} \sum_{m=-M/2}^{M/2-1} t_{ij}(f_n) \frac{1}{\sqrt{\nu^2+\rho^2}} \end{aligned} \tag{4.35}$$

where $\nu = \nu_R + j2\pi f_n = \nu_R + j2\pi n/(M\Delta k_\rho)$. In the above equations, M is the total number of sampling points which is a certain integral power of 2 (i.e., $2^1, 2^2, 2^3$, etc). The integration of Eq.(4.35) was evaluated using the following integration formula[78].

$$\int_0^\infty exp(-\nu k_\rho) J_n(k_\rho \rho) dk_\rho = \frac{\rho^n [\sqrt{\nu^2+\rho^2} - \nu]^n}{\sqrt{\nu^2+\rho^2}}$$

when $\nu = \nu_R + j\nu_I$ and for $Re(\nu + j\rho) > 0$. The expansion coefficient $t_{ij}(f)$ in Eq.(4.34) is easily obtained using the FFT algorithm available in [79].

The total number of sampling points, M, should be chosen so that the value of function $T_{ij}(k_\rho)$ is small enough to be neglected in the range $k_\rho > M\Delta k_\rho$. The increment, Δk_ρ, must be chosen considering the effect of the pole that appears in the function $T_{ij}(k_\rho)$. If the upper half space is slightly conductive, which corresponds to that the imaginary part of k_0 is not perfectly zero, the Δk_ρ can be smaller than the distance of the branch point from the real axis on the complex k_ρ plane. If the imaginary part of k_0 is perfectly zero, the Δk_ρ must be chosen in such a way that one of the data points coincides with the branch point and such that Δk_ρ is smaller than the distance of the pole or branch point closest to the real axis on the complex k_ρ plane.

In the case of a horizontal dipole that creates both TM and TE, a similar procedure is applied to evaluate a_{ij}^r and it is omitted here.

4.4 Numerical Results

In order to verify the algorithm, the driving point impedance of a half wavelength dipole over a perfect conducting plane is computed and compared with results obtained from NEC code. Figure 4.2 shows the comparison of input impedances of a horizontal dipole and Figure 4.3 for a vertical dipole. In these figures, the impedances are normalized with the input impedance of the dipoles in free space. The results are in good agreement as seen in the figures.

The dipole over a lossy layer with perfect conductor backing is then analyzed using our code to estimate the effect of lossy layers on wire antennas. Since the layer is used to simulate the pyramidal or wedge absorber of the anechoic chamber, a linearly varying dielectric constant profile is appropriate (see chapter III) for the layer. The input impedances of a horizontal dipole are computed as a function of layer thickness and are shown in Figure 4.4 when it is located 0.1 and 0.5 wavelengths above the layer. The dielectric constant used in this computation is 1. (free space) at the top and $4. - j0.3$ at the bottom of the layer. The impedances are very sensitive to the thickness of the layer when the dipole is located 0.1 wavelengths above the layer. When the dipole is at 0.5 wavelengths above the layer, the impedance becomes less sensitive and approaches the free space impedance if the thickness is larger than one wavelength.

Figure 4.5 shows the input impedances of vertical dipole as a function of layer thickness when the center of dipole is 0.3 and 0.5 wavelengths above the layer. The vertical dipole is affected much less by the lossy slab than the horizontal dipole is. The input impedance of a vertical dipole is almost that of free space if the thickness of the layer is greater than 0.5 wavelengths.

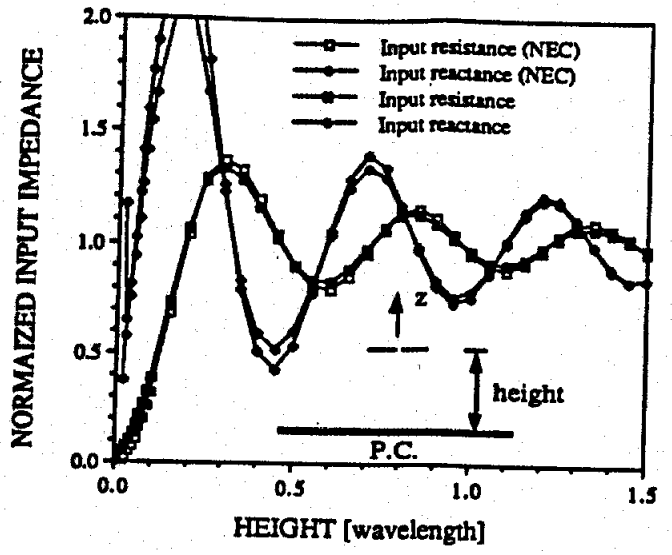

Figure 4.2: Input impedance of the horizontal half wavelength dipole over a P.C. as a function of height.

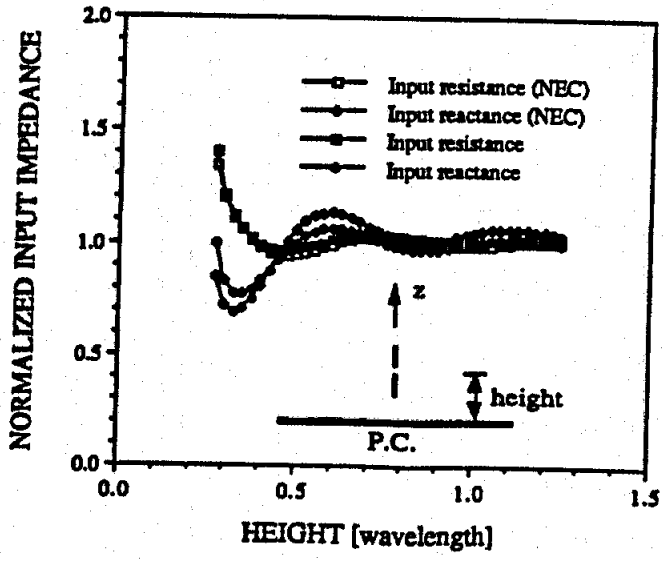

Figure 4.3: Input impedance of the vertical half wavelength dipole over a P.C. as a function of height.

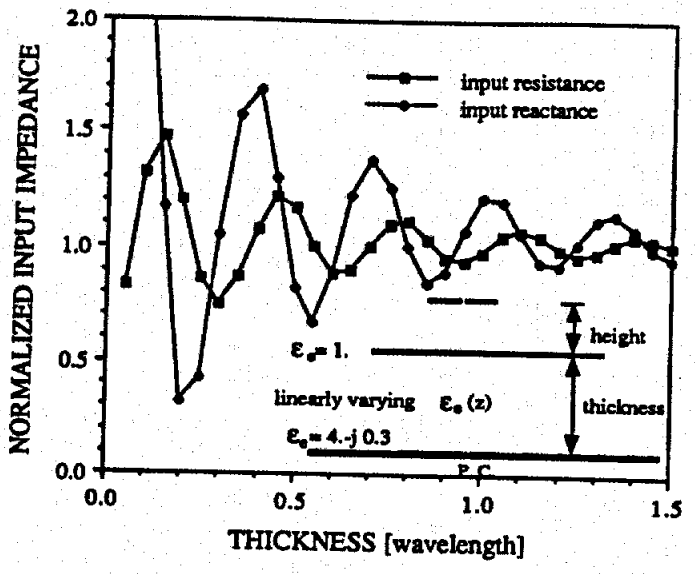

(a) height = 0.1 wavelength

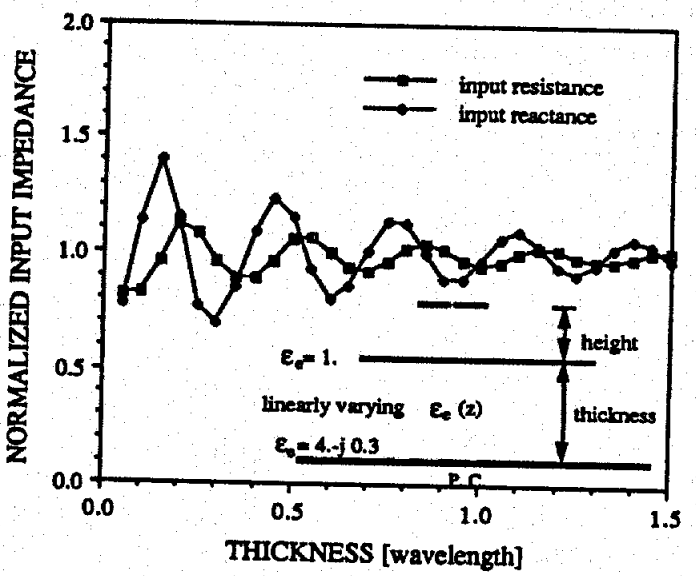

(b) height = 0.5 wavelength

Figure 4.4: Input impedance of the horizontal half wavelength dipole over a lossy dielectric layer as a function of thickness.

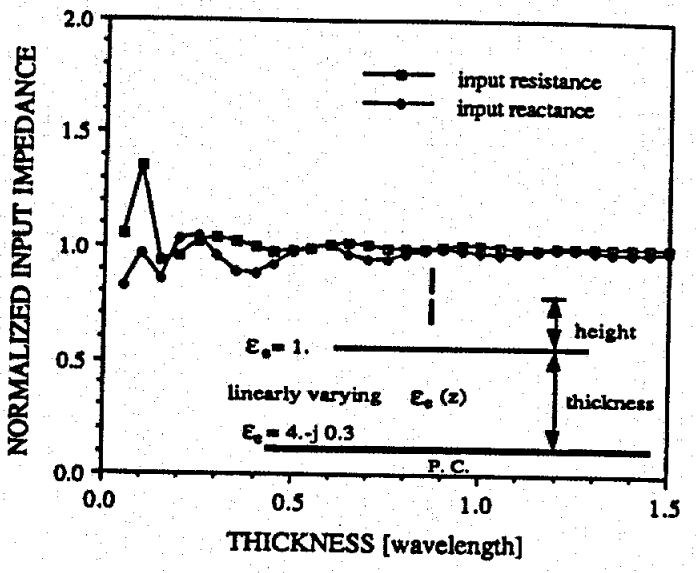

(a) height = 0.3 wavelength

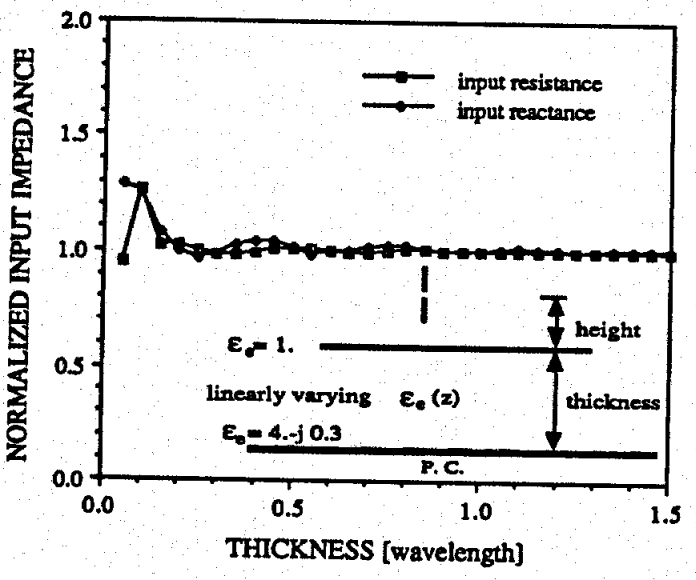

(b) height = 0.5 wavelength

Figure 4.5: Input impedance of the vertical half wavelength dipole over a lossy dielectric layer as a function of thickness.

CHAPTER V

3-D FINITE ELEMENT SOLUTION OF FOUR-WIRE ANTENNA IN TAPERED ANECHOIC CHAMBER

5.1 Introduction

Due to the complex geometry, the four-wire antenna in an anechoic chamber is almost impossible to analyze without using numerical techniques. For the free space analysis of the four-wire antenna, the method of moments(MOM) was employed with a free space Green's function and this was presented in Chapter II and in [80],[81]. However, when the antenna is inside a chamber, a new Green's function associated with the chamber and lossy absorbers is required. Unfortunately, such a Green's function cannot be obtained due to the complex geometry of the chamber. The use of the free space Green's function instead of the new Green's function would require an extremely large number of unknowns, including fields in the chamber, in absorbers, as well as on the wires, that it would be quite difficult, if not impossible, to manage and solve. As an alternative, a three-dimensional finite element method (FEM)[82]-[86] is employed to study the four-wire antenna in a tapered anechoic chamber. Even though the total number of unknown variables in the finite element formulation is larger than that in the method of moments, the system matrix

the FEM is extremely sparse and easier to solve than the impedance matrix of the MOM, which is full. This makes the analysis of the four-wire antenna in the chamber feasible.

The finite element technique has been a popular tool in most engineering applications as well as in microwave engineering due to its flexibility and versatility[82]-[90]. In applying the finite element technique to wave problems, the solutions have been known to include nonphysical spurious results[87]-[91]. To eliminate these spurious results, a combined method formulated with transverse field components has been developed[89]. However, this is not valid for three-dimensional problems, and for these a penalty function method has been used successfully[90].

In this chapter, we describe the analysis of the four-wire antenna in a tapered anechoic chamber using a three-dimensional finite element technique. Section 5.2 derives global system equations from Maxwell's equations. In setting up the equations, two types of formulations are available in the finite element technique. One is the variational formulation[92], which uses the concept of minimizing the total energy in the system[90]. The other one is the weighted residual formulation, which uses the concept of minimizing an error introduced by approximating a solution[85]. Both formulations result in the same system equations. In section 5.2, a weighted residual formulation is used. Then, in section 5.3, the system equations are discretized into element system equations for each element. For this discretization, two kinds of shape functions, linear and quadratic, are considered. Section 5.4 describes the method of assembling and solving the system equations. To assemble and solve the system matrix, a frontal technique is employed. In section 5.5, the four-wire antenna is solved when it is in the tapered anechoic chamber and the results are presented.

5.2 Finite Element Formulation

In a linear homogeneous medium, when an electric current density $\vec{J}$ is applied, the point(local) form of Maxwell's equations for electric field, $\vec{\mathcal{E}}$, and magnetic field, $\vec{\mathcal{H}}$ are given as

$$\nabla \times \vec{\mathcal{E}}(\vec{r}) = -j\omega\mu\vec{\mathcal{H}}(\vec{r}) \tag{5.1}$$

$$\nabla \times \vec{\mathcal{H}}(\vec{r}) = j\omega\epsilon\vec{\mathcal{E}}(\vec{r}) + \vec{J}(\vec{r}) \tag{5.2}$$

where μ and ϵ are the uniform permeability and permittivity at point $\vec{r}$, respectively.

Vector Helmholtz or wave equations for electric and magnetic fields are obtained by applying curl operations on Eqs.(5.1) and (5.2) to give

$$\nabla \times \nabla \times \vec{\mathcal{E}}(\vec{r}) - k^2\vec{\mathcal{E}}(\vec{r}) = -j\omega\mu\vec{J}(\vec{r}) \tag{5.3}$$

$$\nabla \times \nabla \times \vec{\mathcal{H}}(\vec{r}) - k^2\vec{\mathcal{H}}(\vec{r}) = \nabla \times \vec{J} \tag{5.4}$$

where k is a propagation constant expressed as $k = \omega\sqrt{\mu\epsilon}$. When electric(or magnetic) fields are obtained by solving Eq.(5.3) (or Eq.(5.4)) with appropriate boundary conditions, the magnetic(or electric) fields are easily obtained from Eq.(5.1)(or Eq.(5.2)).

When solving the governing equation, one must consider the composition of the domain. If the domain consists of different dielectric materials, but of the same permeability, the use of Eq.(5.4) is more convenient than that of Eq.(5.3) because every component of the magnetic field is continuous in the domain. The use of Eq.(5.3) for the same domain is not as convenient since the normal electric field component to the different dielectric interfaces is not continuous and may require special attention. Since the four-wire antenna system in the anechoic chamber consists of several dielectric material classes, such as loading resistance and absorbers, Eq.(5.4) is chosen

and solved for magnetic vector fields.

In general, for a complex geometry, it is difficult to obtain an exact solution that satisfies Eq.(5.4) with proper boundary conditions. However, the solution can be expressed in a form of infinite summation of independent basis (or trial) functions with appropriate coefficients. An approximate solution, $\vec{H}(\vec{r})$, can be obtained by using a finite number of summations instead of infinite summations and written as

$$\vec{\mathcal{H}}(\vec{r}) \simeq \vec{H}(\vec{r}) = \sum_{m=1}^{M} \vec{H}_m N_m(\vec{r}) \tag{5.5}$$

where $\vec{\mathcal{H}}(\vec{r})$ is the exact solution, $N_m(\vec{r})$ are the expansion function, and $\vec{H}_m$ are the coefficients to be computed to obtain a good approximation. The basis function set should be chosen so as to ensure that the approximation is improved with increased number, M, of basis functions used. One obvious condition for the convergence of this approximation is that the approximate solution, $\vec{H}(\vec{r})$, can adequately represent any exact solution, $\vec{\mathcal{H}}(\vec{r})$ as $M \to \infty$.

The coefficients, $\vec{H}_m; m = 1, \cdots, M$, are determined by the following weighted residual process. This process begins by introducing a residual (or error), $\vec{R}_V(\vec{r})$, in a domain volume that is defined as

$$\vec{R}_V(\vec{r}) = \nabla \times \nabla \times \vec{H}(\vec{r}) - k^2 \vec{H}(\vec{r}) - \nabla \times \vec{J} \tag{5.6}$$

On conducting boundary surfaces, residuals, $\vec{R}_{S_e}(\vec{r})$ and $\vec{R}_{S_m}(\vec{r})$, are defined as

$$\vec{R}_{S_e}(\vec{r}) = \nabla \times \vec{H}(\vec{r}) \times \hat{n} \text{ on electric conducting surfaces}$$

$$\vec{R}_{S_m}(\vec{r}) = \vec{H}(\vec{r}) \times \hat{n} \text{ on magnetic conducting surfaces}$$

where $\hat{n}$ is an outward normal unit vector to the boundary surfaces. The domain residual comes from Eq.(5.4) and the boundary residuals are constructed to satisfy

the boundary conditions

$$\nabla \times \vec{H}(\vec{r}) \times \hat{n} = 0 \text{ on a perfect electric conducting surface} \quad (5.7)$$

$$\vec{H}(\vec{r}) \times \hat{n} = 0 \text{ on a perfect magnetic conducting surface} \quad (5.8)$$

One can introduce other residuals for other types of boundary surfaces. In this thesis only the above two types of boundary conditions are considered. That is, the boundary surface, S, of closed domain volume, V, is expressed as $S = S_e + S_m$.

Note that the residuals are also functions of position. As $\vec{R}(\vec{r})$ becomes zero everywhere, the approximate solution becomes the exact solution. Therefore, the summation of integrals of the residuals over the domain and boundaries, weighted in different ways, is required to be zero, that is,

$$\begin{aligned} &\int_V \vec{W}_l(\vec{r}) \cdot \vec{R_V}(\vec{r}) dV + \int_{S_e} \vec{W}_l^e(\vec{r}) \cdot \vec{R_{S_e}}(\vec{r}) dS + \int_{S_m} \vec{W}_l^m(\vec{r}) \cdot \vec{R_{S_m}}(\vec{r}) dS \equiv \\ &\int_V \vec{W}_l(\vec{r}) \cdot (\nabla \times \nabla \times \vec{H}(\vec{r}) - k^2 \vec{H}(\vec{r}) - \nabla \times \vec{J}) dV \\ + &\int_{S_e} \vec{W}_l^e(\vec{r}) \cdot \nabla \times \vec{H}(\vec{r}) \times \hat{n} dS + \int_{S_m} \vec{W}_l^m(\vec{r}) \cdot \vec{H}(\vec{r}) \times \hat{n} dS = 0 \end{aligned} \quad (5.9)$$

where $l = 1, 2, \cdots, M$. In the above equation, $\vec{W}_l(\vec{r}); l = 1, 2, \cdots, M$ is a set of independent weighting vectors in the domain and the superscripts e and m of $\vec{W}_l(\vec{r})$ denote the electric and the magnetic perfect conducting boundaries, respectively. For each l, three independent weighting vectors are required to make the weighted residual vectors identically zero. By imposing the three independent weighting vectors, three equations for each l are obtained.

To meet the convergence requirement, Eq.(5.9) must be satisfied for all l as $M \rightarrow \infty$. This is true when $\vec{R}(\vec{r}) \rightarrow 0$ at all points of the domain and boundary. Using a vector identity and Gauss theorem, the first term in the parenthesis of Eq.(5.9)

becomes

$$\int_V \vec{W}_l(\vec{r})\cdot\nabla\times\nabla\times\vec{H}(\vec{r})dV = \oint_S \nabla\times\vec{H}(\vec{r})\times\vec{W}_l(\vec{r})\cdot\hat{n}dS + \int_V(\nabla\times\vec{H}(\vec{r}))\cdot(\nabla\times\vec{W}_l(\vec{r}))dV \tag{5.10}$$

This form is often called a "weak form". Using the vector identity, the surface integral of Eq.(5.10) is rewritten as

$$\oint_S \nabla\times\vec{H}(\vec{r})\times\vec{W}_l(\vec{r})\cdot\hat{n}dS = -\int_{S_e} \nabla\times\vec{H}(\vec{r})\times\hat{n}\cdot\vec{W}_l(\vec{r})dS + \int_{S_m} \nabla\times\vec{H}(\vec{r})\cdot\vec{W}_l(\vec{r})\times\hat{n}dS \tag{5.11}$$

and by combining Eqs.(5.10), (5.11), and (5.9) and choosing $\vec{W}_l^e(\vec{r}) = \vec{W}_l(\vec{r})$ and $\vec{W}_l^m(\vec{r}) = -\vec{W}_l(\vec{r})$, one obtains

$$\int_V\{(\nabla\times\vec{H}(\vec{r}))\cdot(\nabla\times\vec{W}_l(\vec{r})) + k^2\vec{W}_l(\vec{r})\cdot\vec{H}(\vec{r}) - \vec{W}_l(\vec{r})\cdot\nabla\times\vec{J}\}dV = 0 \tag{5.12}$$

Eq.(5.12) is a resultant global system equation.

It is well known that Eq.(5.12) has spurious solutions[88]-[91]. In order to avoid such solutions, a penalty method is used by adding to Eq.(5.12) a least squares constraint satisfying $div\vec{H} = 0$ so that the governing equations are explicitly the Helmholtz equation plus the vanishing of $div\vec{H}$. By adding the constraint in a least squares sense, Eq.(5.12) becomes

$$\begin{aligned}&\int_V\{\ (\nabla\times\vec{H}(\vec{r}))\cdot(\nabla\times\vec{W}_l(\vec{r})) + k^2\vec{W}_l(\vec{r})\cdot\vec{H}(\vec{r}) + s(\nabla\cdot\vec{H}(\vec{r}))(\nabla\cdot\vec{W}_l(\vec{r}))\ \}\ dV \\ &= \int_V \vec{W}_l(\vec{r})\cdot\nabla\times\vec{J}\ dV\end{aligned} \tag{5.13}$$

where s is a penalty number that represents how heavily the constraint is imposed.

One thing to note in using the penalty method is the choice of an appropriate penalty number since the imposition of a constraint can be compared with changing of natural boundary conditions of the equation by introducing an additional appropriate integrand. If the penalty number is not chosen properly, the solution may not be a

physical one. One advantage of using the penalty method is that it does not increase the matrix order, and the additional computation time is negligible.

There exist a large number of possible choices for the weighting vector set. The most popular weighting functions are, as Galerkin originally used, the basis functions themselves, that is,

$$\vec{W}_l = N_l^x(\vec{r})\hat{x} + N_l^y(\vec{r})\hat{y} + N_l^z(\vec{r})\hat{z} \tag{5.14}$$

In order to make the weighted residual vectors identically zero, three independent weighting vectors for each l are necessarily required, with which the dot operations on the residual vectors are zero (see Eq.(5.9)). For this, one can simply choose three independent weighting vectors for the same l as

$$\vec{W}_l = N_l^p(\vec{r})\hat{p} \tag{5.15}$$

where p is x, y, and z. Applying the expanded expression of Eq.(5.5) and Galerkin's weighting vector of Eq.(5.14) into the Eq.(5.13), the following equation is obtained.

$$\begin{aligned}
\sum_{m=1}^{M}\int_V \{\ & H_m^x[\frac{\partial}{\partial z}N_m(\frac{\partial}{\partial z}N_l^x - \frac{\partial}{\partial x}N_l^z) + \frac{\partial}{\partial y}N_m(\frac{\partial}{\partial y}N_l^x - \frac{\partial}{\partial x}N_l^y) \\
&+ s\frac{\partial}{\partial x}N_m(\frac{\partial}{\partial x}N_l^x + \frac{\partial}{\partial y}N_l^y\frac{\partial}{\partial z}N_l^z) + k^2N_mN_l^x] \\
&+ H_m^y[\frac{\partial}{\partial x}N_m(\frac{\partial}{\partial x}N_l^y - \frac{\partial}{\partial y}N_l^x) + \frac{\partial}{\partial z}N_m(\frac{\partial}{\partial z}N_l^y - \frac{\partial}{\partial y}N_l^z) \\
&+ s\frac{\partial}{\partial y}N_m(\frac{\partial}{\partial x}N_l^x + \frac{\partial}{\partial y}N_l^y\frac{\partial}{\partial z}N_l^z) + k^2N_mN_l^y] \\
&+ H_m^z[\frac{\partial}{\partial y}N_m(\frac{\partial}{\partial y}N_l^z - \frac{\partial}{\partial z}N_l^y) + \frac{\partial}{\partial x}N_m(\frac{\partial}{\partial x}N_l^z - \frac{\partial}{\partial z}N_l^x) \\
&+ s\frac{\partial}{\partial z}N_m(\frac{\partial}{\partial x}N_l^x + \frac{\partial}{\partial y}N_l^y\frac{\partial}{\partial z}N_l^z) + k^2N_mN_l^z] \ \}\ dV \\
= \int_V & [N_l^x(\nabla\times\vec{J})_x + N_l^y(\nabla\times\vec{J})_y + N_l^z(\nabla\times\vec{J})_z]\ dV
\end{aligned} \tag{5.16}$$

where $(\nabla\times\vec{J})_p$ denotes the $\hat{p}$ component of $(\nabla\times\vec{J})$ and H_m^p represents $\hat{p}$ component of H_m. For each l, Eq.(5.16) is divided into 3 equations for each independent weighting

vector of Eq.(5.15). One of the three equations is Eq.(5.16) where $N_l^x = N_l$ with $N_l^y = N_l^z = 0$ and the other two are Eq(5.16) where $N_l^y = N_l$ with $N_l^x = N_l^z = 0$, and $N_l^z = N_l$ with $N_l^x = N_l^y = 0$. By solving Eq.(5.16) with appropriate boundary conditions for a given geometry, an approximate solution set is obtained.

Before closing this section, let us rewrite the boundary conditions in terms of the coefficients of Eq.(5.5). If a node n is on the magnetic conducting boundary, the fields at $\vec{r}_n$ must satisfy Eq.(5.8). That is,

$$\vec{H}(\vec{r_n}) \times \hat{n} = \sum_{m=1}^{M} \vec{H}_m N_m(\vec{r}_n) \times \hat{n} = \vec{H}_n \times \hat{n} = 0 \tag{5.17}$$

when

$$N_m(\vec{r}_n) = \begin{cases} 1 & \text{if } m = n \\ 0 & \text{if } m \neq n \end{cases} \tag{5.18}$$

Therefore, $\vec{H}_n \times \hat{n} = 0$ can be used for the boundary condition of Eq.(5.8). For the boundary condition on the electric conducting boundary, Eq.(5.7) is rewritten as

$$\vec{H}(\vec{r}) \cdot \hat{n} = 0 \tag{5.19}$$

since $\nabla \times \vec{H}(\vec{r})$ is perpendicular to $\vec{H}(\vec{r})$. Therefore, for a node n located on the electric conducting boundary, the boundary condition to be enforced is $\vec{H}_n \cdot \hat{n} = 0$ when $N_m(\vec{r}_n)$ satisfies Eq.(5.18).

5.3 Finite Element Discretization and Basis Functions

For a numerical implementation of Eq.(5.16), the integration must be discretized by subdividing V into smaller volumes, V^e. The shape of the discretized volume can be a tetrahedron, triangular prism, hexahedron, etc. This smaller volume is called an "element" and each element has its nodal points; $r_n, n = 1, 2, \cdots, M^n$ where M^n is the number of nodes of one element. In order for the coefficient, H_n, to represent

the unknown field at the nodal point n, the value of the basis function is chosen so that $N_m(\vec{r_n}) = 1$ if $\vec{r}_n = \vec{r}_m$ and $N_m(\vec{r}) = 0$ if $\vec{r}_n \neq \vec{r}_m$. In elements containing a node m, the nodal basis function $N_m(\vec{r})$ is a nonzero function, while in elements not containing a node m, $N_m(\vec{r})$ is a zero function. Therefore, the global basis function is expressed as

$$N_m(\vec{r}) = \begin{cases} N_m^e(\vec{r}) & \text{if element } e \text{ contains node } m \\ 0 & \text{if element } e \text{ does not contain node } m \end{cases} \tag{5.20}$$

where $N_m^e(\vec{r})$ is a basis function defined only in the e^{th} element. The element basis function $N_m^e(\vec{r})$ can be a linear, a quadratic, or a higher order function.

Thus, Eq.(5.16) is discretized and rewritten as

$$\begin{aligned} \sum_{e=1}^{M^e}\sum_{m=1}^{M^n}\int_{V^e} \{ & H_m^x[\frac{\partial}{\partial z}N_m^e(\frac{\partial}{\partial z}N_l^{x,e} - \frac{\partial}{\partial x}N_l^{z,e}) + \frac{\partial}{\partial y}N_m^e(\frac{\partial}{\partial y}N_l^{x,e} - \frac{\partial}{\partial x}N_l^{y,e}) \\ & + s\frac{\partial}{\partial x}N_m^e(\frac{\partial}{\partial x}N_l^{x,e} + \frac{\partial}{\partial y}N_l^{y,e}\frac{\partial}{\partial z}N_l^{z,e}) + k^2N_m^eN_l^{x,e}] \\ & + H_m^y[\frac{\partial}{\partial x}N_m^e(\frac{\partial}{\partial x}N_l^{y,e} - \frac{\partial}{\partial y}N_l^{x,e}) + \frac{\partial}{\partial z}N_m^e(\frac{\partial}{\partial z}N_l^{y,e} - \frac{\partial}{\partial y}N_l^{z,e}) \\ & + s\frac{\partial}{\partial y}N_m^e(\frac{\partial}{\partial x}N_l^{x,e} + \frac{\partial}{\partial y}N_l^{y,e}\frac{\partial}{\partial z}N_l^{z,e}) + k^2N_m^eN_l^{y,e}] \\ & + H_m^z[\frac{\partial}{\partial y}N_m^e(\frac{\partial}{\partial y}N_l^{z,e} - \frac{\partial}{\partial z}N_l^{y,e}) + \frac{\partial}{\partial x}N_m^e(\frac{\partial}{\partial x}N_l^{z,e} - \frac{\partial}{\partial z}N_l^{x,e}) \\ & + s\frac{\partial}{\partial z}N_m^e(\frac{\partial}{\partial x}N_l^{x,e} + \frac{\partial}{\partial y}N_l^{y,e}\frac{\partial}{\partial z}N_l^{z,e}) + k^2N_m^eN_l^{z,e}] \} \, dV \\ = & \int_{V_e}[N_l^{x,e}(\nabla\times\vec{J}^e)_x + N_l^{y,e}(\nabla\times\vec{J}^e)_y + N_l^{z,e}(\nabla\times\vec{J}^e)_z] \, dV \end{aligned} \tag{5.21}$$

where M^e is the total number of elements and the superscript e denotes the e^{th} element.

If the basis functions defining geometry and function are the same, the elements are called isoparametric. In the isoparametric elements, the coordinates x, y, z as well as $\vec{H}(x,y,z)$ are expressed as

$$\vec{H}(x,y,z) = \sum_{m=1}^{M_n} N_m^e(x,y,z)\vec{H}_m$$

$$
\begin{aligned}
x &= \sum_{m=1}^{M_n} N_m^e(x,y,z)x_m \\
y &= \sum_{m=1}^{M_n} N_m^e(x,y,z)y_m \\
z &= \sum_{m=1}^{M_n} N_m^e(x,y,z)z_m \qquad (5.22) \\
1 &= \sum_{m=1}^{M_n} N_m^e(x,y,z) \qquad (5.23) \\
& \qquad (5.24)
\end{aligned}
$$

In most finite element formulations, a tetrahedral and a rectangular (brick) element with linear basis functions are commonly used because of their simplicity in formulation. However, the use of rectangular brick elements is restricted when applied to a non-rectangular geometrical shape. Also, the use of a linear basis function requires a large number of elements and nodes when the domain includes a radiator or when the field in the domain changes rapidly. In this section, a linear basis function for tetrahedral elements and a quadratic basis function for hexahedral elements are described for use in later sections.

5.3.1 Tetrahedral Element with Linear Basis Functions

A tetrahedral element is one of the commonly used elements in the three-dimensional finite element technique because this element has an appropriate shape to construct any three-dimensional geometry with the least approximation. Figure 5.1 shows a tetrahedral element with consistent node ordering. The ordering of nodal numbers j, k, l, m of Figure 5.1 follows a "right hand" rule. For this, the first three nodes are numbered in an counterclockwise manner when viewed from the last one.

The linear basis function of node j for the tetrahedral element e is expressed as

$$N_j^e = \frac{1}{6V^e}(a_j + b_j x + c_j y + d_j z) \qquad (5.25)$$

with

$$6V^e = det\begin{vmatrix} 1 & x_j & y_j & z_j \\ 1 & x_k & y_k & z_k \\ 1 & x_l & y_l & z_l \\ 1 & x_m & y_m & z_m \end{vmatrix}$$

and

$$a_j = (+1)^j det\begin{vmatrix} x_k & y_k & z_k \\ x_l & y_l & z_l \\ x_m & y_m & z_m \end{vmatrix} \qquad b_j = (-1)^j det\begin{vmatrix} 1 & y_k & z_k \\ 1 & y_l & z_l \\ 1 & y_m & z_m \end{vmatrix}$$

$$c_j = (-1)^j det\begin{vmatrix} x_k & 1 & z_k \\ x_l & 1 & z_l \\ x_m & 1 & z_m \end{vmatrix} \qquad d_j = (-1)^j det\begin{vmatrix} x_k & y_k & 1 \\ x_l & y_l & 1 \\ x_m & y_m & 1 \end{vmatrix}$$

where the value, V^e, represents the volume of the tetrahedron.

One of the advantages in the use of linear basis function is that the integration over a volume can be performed analytically[84]. Applying the basis functions of Eq.(5.25) to Eq.(5.21) and integrating over the element volume, element system equations for e^{th} element are obtained. The element system equations consist of the following 12 linear equations with 12 unknown coefficients (three magnetic field components for each of the four nodes).

$$\sum_{m=1}^{4} \frac{1}{36V^e} \left[H_m^x(sb_m b_l + d_m d_l + c_m c_l) + H_m^y(sc_m b_l - b_m c_l) + H_m^z(sd_m b_l - b_m d_l)\right]$$
$$-k^2 H_m^x V_1 = (\nabla \times \vec{J})_x V_e/4$$

$$\sum_{m=1}^{4} \frac{1}{36V^e} \left[H_m^x(sb_m c_l - c_m b_l) + H_m^y(sc_m c_l + b_m b_l + d_m d_l) + H_m^z(sd_m c_l - c_m d_l)\right]$$
$$-k^2 H_m^y V_1 = (\nabla \times \vec{J})_y V_e/4$$

$$\sum_{m=1}^{4} \frac{1}{36V^e} \left[H_m^x(sb_m d_l - d_m b_l) + H_m^y(sc_m d_l - d_m c_l) + H_m^z(sd_m d_l + c_m c_l + b_m b_l)\right.$$
$$-k^2 H_m^z V_1 = (\nabla \times \vec{J})_z V_e/4$$

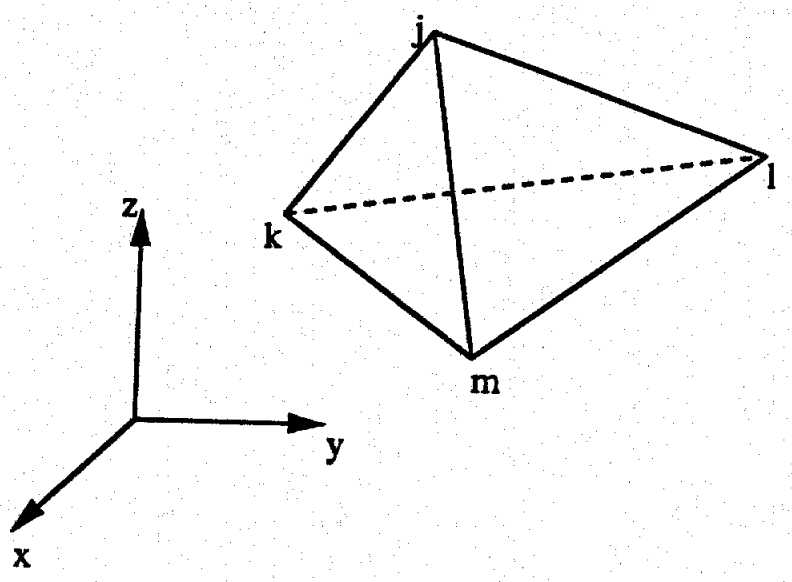

Figure 5.1: A tetrahedral volume element. The numbering of the nodes are consistent so that the first three nodes are numbered counter-clockwise when viewed from the last one.

where

$$V_l = \begin{cases} V^e/10 & \text{if } m = n \\ V^e/20 & \text{if } m \neq n \end{cases}$$

with $l = 1, 2, 3, 4$. Each equation in the above set corresponds to each of the independent weighting vector of Eq.(5.15) with $p = x, y$, and z, respectively. These element system equations are assembled for all the elements to generate the global system equations.

5.3.2 Hexahedral Elements with Quadratic Basis Functions

When the domain includes a source or a radiator inside, the use of linear basis functions would require many elements around the radiator. For this kind of problem, a quadratic or a higher order basis function is much more efficient than the linear one. A disadvantage of higher order basis function is that the integration cannot be

performed analytically and requires a numerical technique that requires longer time to generate the element system matrix. This numerical integration time, however, is negligible compared to the time required for solving system equations. In this section, a hexahedral element with quadratic basis function is described.

Figure 5.2 shows the general hexahedral element with 20 nodes (8 corner nodes and 12 mid side nodes) in cartesian coordinates and transformed coordinates. Any shape of a hexahedron in cartesian coordinates can be uniquely mapped into transformed coordinates using a shape function transformation. In the transformed coordinates, the hexahedron is a rectangular brick as shown in the figure. In both coordinates, the shape functions should satisfy $N_m = 1$ at node m and $N_m = 0$ at other nodes. Therefore, in isoparametric elements, one can write

$$\begin{aligned}
\vec{H}(x,y,z) &= \sum_{m=1}^{M_n} N'^e_m(x,y,z)\vec{H}_m = \sum_{m=1}^{M_n} N^e_m(\xi,\eta,\zeta)\vec{H}_m \\
x &= \sum_{m=1}^{M_n} N'^e_m(x,y,z)x_m = \sum_{m=1}^{M_n} N^e_m(\xi,\eta,\zeta)\xi_m \\
y &= \sum_{m=1}^{M_n} N'^e_m(x,y,z)y_m = \sum_{m=1}^{M_n} N^e_m(\xi,\eta,\zeta)\eta_m \\
z &= \sum_{m=1}^{M_n} N'^e_m(x,y,z)z_m = \sum_{m=1}^{M_n} N^e_m(\xi,\eta,\zeta)\zeta_m
\end{aligned} \tag{5.26}$$

where N'^e_m and N^e_m denote the element basis function in cartesian and transformed coordinates, respectively. In general, the element basis functions in cartesian coordinates are not easy to obtain in a compact form due to the irregular shape of the element. However, the basis functions in transformed coordinates are easily obtained as

$$N_m = \frac{1}{8}(1+\xi\xi_m)(1+\eta\eta_m)(1+\zeta\zeta_m)(\xi\xi_m+\eta\eta_m+\zeta\zeta_m-2) \tag{5.27}$$

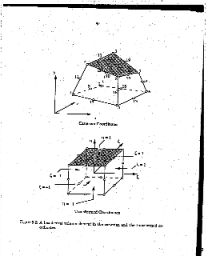

Cubical Coordinates

Cylindrical Coordinates

Elliptic Cylindrical Coordinates

Ellipsoidal Coordinates

Hyperbolic Cylindrical Coordinates

Oblate Spheroidal Coordinates

Paraboloidal Coordinates

Prolate Spheroidal Coordinates

Spherical Coordinates

Toroidal Coordinates

for corner nodes and

$$N_m = \begin{cases} \frac{1}{4}(1-\xi^2)(1+\eta\eta_m)(1+\zeta\zeta_m) & \text{for } \xi_m = 0, \eta_m = \pm 1, \zeta_m = \pm 1 \\ \frac{1}{4}(1+\xi\xi_m)(1-\eta^2)(1+\zeta\zeta_m) & \text{for } \xi_m = \pm 1, \eta_m = 0, \zeta_m = \pm 1 \\ \frac{1}{4}(1+\xi\xi_m)(1+\eta\eta_m)(1-\zeta^2) & \text{for } \xi_m = \pm 1, \eta_m = \pm 1, \zeta_m = 0 \end{cases} \tag{5.28}$$

for mid-side nodes where the coordinates are shown in Figure 5.2.

Although the basis functions for each node are given in Eqs.(5.27) and (5.28), the differentiation and integration of the functions in cartesian coordinates are required to generate the system equation of Eq.(5.21). The differentiation in cartesian coordinates is obtained using the rule of partial differentiation. Differentiating with respect to the transformed coordinates and writing in matrix form, one can obtain

$$\begin{Bmatrix} \frac{\partial N_m^e}{\partial \xi} \\ \frac{\partial N_m^e}{\partial \eta} \\ \frac{\partial N_m^e}{\partial \zeta} \end{Bmatrix} = \begin{bmatrix} \frac{\partial x}{\partial \xi} & \frac{\partial y}{\partial \xi} & \frac{\partial z}{\partial \xi} \\ \frac{\partial x}{\partial \eta} & \frac{\partial y}{\partial \eta} & \frac{\partial z}{\partial \eta} \\ \frac{\partial x}{\partial \zeta} & \frac{\partial y}{\partial \zeta} & \frac{\partial z}{\partial \zeta} \end{bmatrix} \begin{Bmatrix} \frac{\partial N_m^e}{\partial x} \\ \frac{\partial N_m^e}{\partial y} \\ \frac{\partial N_m^e}{\partial z} \end{Bmatrix} \equiv \mathbf{J} \begin{Bmatrix} \frac{\partial N_m^e}{\partial x} \\ \frac{\partial N_m^e}{\partial y} \\ \frac{\partial N_m^e}{\partial z} \end{Bmatrix} \tag{5.29}$$

where $\mathbf{J}$ denotes the Jacobian matrix. In the above relation, the left hand side can be evaluated directly from Eqs.(5.27) and (5.28). The Jacobian matrix is found explicitly from the relation of Eq.(5.26) as a function of the transformed coordinate variables and written as

$$\mathbf{J} \doteq \begin{bmatrix} \sum \frac{\partial N_m}{\partial \xi}\xi_m & \sum \frac{\partial N_m}{\partial \xi}\eta_m & \sum \frac{\partial N_m}{\partial \xi}\zeta_m \\ \sum \frac{\partial N_m}{\partial \eta}\xi_m & \sum \frac{\partial N_m}{\partial \eta}\eta_m & \sum \frac{\partial N_m}{\partial \eta}\zeta_m \\ \sum \frac{\partial N_m}{\partial \zeta}\xi_m & \sum \frac{\partial N_m}{\partial \zeta}\eta_m & \sum \frac{\partial N_m}{\partial \zeta}\zeta_m \end{bmatrix} \tag{5.30}$$

The cartesian derivatives can be obtained by inverting the Jacobian matrix and written as

$$\begin{Bmatrix} \frac{\partial N_m}{\partial x} \\ \frac{\partial N_m}{\partial y} \\ \frac{\partial N_m}{\partial z} \end{Bmatrix} = \mathbf{J}^{-1} \begin{Bmatrix} \frac{\partial N_m}{\partial \xi} \\ \frac{\partial N_m}{\partial \eta} \\ \frac{\partial N_m}{\partial \zeta} \end{Bmatrix} \tag{5.31}$$

By performing this, the cartesian variables (x, y, z) of the integrand in Eq.(5.21) have been replaced by the transformed variables (ξ, η, ζ).

The volume integration with respect to the cartesian coordinates is also transformed to the integration with respect to the transformed coordinates using

$$dx\ dy\ dz = |\mathbf{J}|\ \mathrm{d}\xi\ \mathrm{d}\eta\ \mathrm{d}\zeta \tag{5.32}$$

where $|\mathbf{J}|$ is the determinant of the Jacobian matrix.

Provided that the inverse of $\mathbf{J}$ can be found, the integral form of Eq.(5.21) can be written as

$$\int_{-1}^{1}\int_{-1}^{1}\int_{-1}^{1} \mathbf{G}(\xi,\eta,\zeta)\mathrm{d}\xi\mathrm{d}\eta\mathrm{d}\zeta \tag{5.33}$$

where $\mathbf{G}(\xi, \eta, \zeta)$ contains the the integrand of Eq.(5.21) in terms of transformed coordinates including the determinant of Eq.(5.32).

Therefore, by transforming the coordinates, a simple form of the integration is obtained that is carried out over a unit rectangular brick whatever the shape in the cartesian coordinates is. However, the explicit form of $\mathbf{G}$ cannot be obtained and thus a numerical integration technique is required. For this, a Gaussian Quadrature technique[84], which is commonly used in the finite element technique, is chosen. The integration of Eq.(5.33) is replaced by a summation as

$$\begin{aligned}&\int_{-1}^{1}\int_{-1}^{1}\int_{-1}^{1} \mathbf{G}(\xi,\eta,\zeta)\mathrm{d}\xi\mathrm{d}\eta\mathrm{d}\zeta \\ &= \sum_{m=1}^{n}\sum_{j=1}^{n}\sum_{i=1}^{n} w_i w_j w_m \mathbf{G}(\xi_\mathrm{i},\eta_\mathrm{j},\zeta_\mathrm{m})\end{aligned} \tag{5.34}$$

where n is the number of integrating points and w is weighting coefficients. The number of integrating points in each direction is chosen to be the same although this is not necessary. For the quadratic basis function, the chosen number of integrating points in each direction is three and thus the total integrating points in a volume

are 27. The positions of the points in each direction are chosen with $-1/\sqrt{3}, 0, 1/\sqrt{3}$ and their weighting coefficients are $5/9, 8/9, 5/9$.

By performing the integration of Eq.(5.34) numerically, the element system equations are obtained. The global system equations are obtained by assembling these element system equations for all the elements.

5.4 Element Assembly and Equation Solving

In order to obtain solutions by the finite element method, one is eventually faced with the task of solving a large set of simultaneous, linear algebraic equations. When solving the large system equations numerically, one can use direct or iterative methods. The iteration method is faster and has less error than the direct method provided that a convergence factor, which is different in different system equations, can be obtained. Since it is not an easy task to find the convergence factor, especially in large system equations, a direct method may be preferred in some cases.

In our analysis, a frontal technique, which uses a direct method, is used to perform the element assembly and equation solving at the same time[86],[94],[95]. The frontal algorithm is a special method that is suitable for the finite element technique. This algorithm assembles the finite element system equations into global system equations and solves for the unknowns using Gaussian elimination simultaneously, and then performs a back-substitution process. It requires less storage, fewer arithmetic operations, and smaller peripheral equipment when compared to other direct solving routines.

The basic idea of the frontal algorithm[94] is that it assembles the equations and eliminates the variables at the same time. As soon as the coefficients of an equation are completely assembled from the contributions of all relevant elements,

the equation is transferred to back-up storage and the corresponding variable is eliminated. Therefore, the complete global system matrix is never formed during the process.

At a certain step during the process when a new element is assembled, a coefficient matrix for variables, which are yet to be eliminated, remains in the core memory. These equations, their corresponding nodes and degrees of freedom, are termed the front. The number of unknowns in the front is the frontwidth. This frontwidth changes during the assembly and reduction process and the average front-width determines the maximum size of problem that can be solved using this method.

In the frontal method, the ordering of elements is important while the nodal numbering is irrelevant. The reason for this is that the life time of a node in the front depends on the element numbering, not the node numbering. Therefore, the element numbering must be done so as to reduce the life time and thus the frontwidth. Another efficient method is a band solution, which requires the entire global matrix to be assembled first and begins to solve it with Gaussian elimination process. The frontal method, however, is a more efficient method, especially in three-dimensional problems[86].

The anechoic chamber geometry that will be solved has a long length compared to its width and height. This geometry enables one to reduce the frontwidth even if it has a large number of unknowns. Therefore, the frontal technique is suitable for this geometry.

For an overview of the frontal algorithm, a flow chart is shown in Figure 5.3.

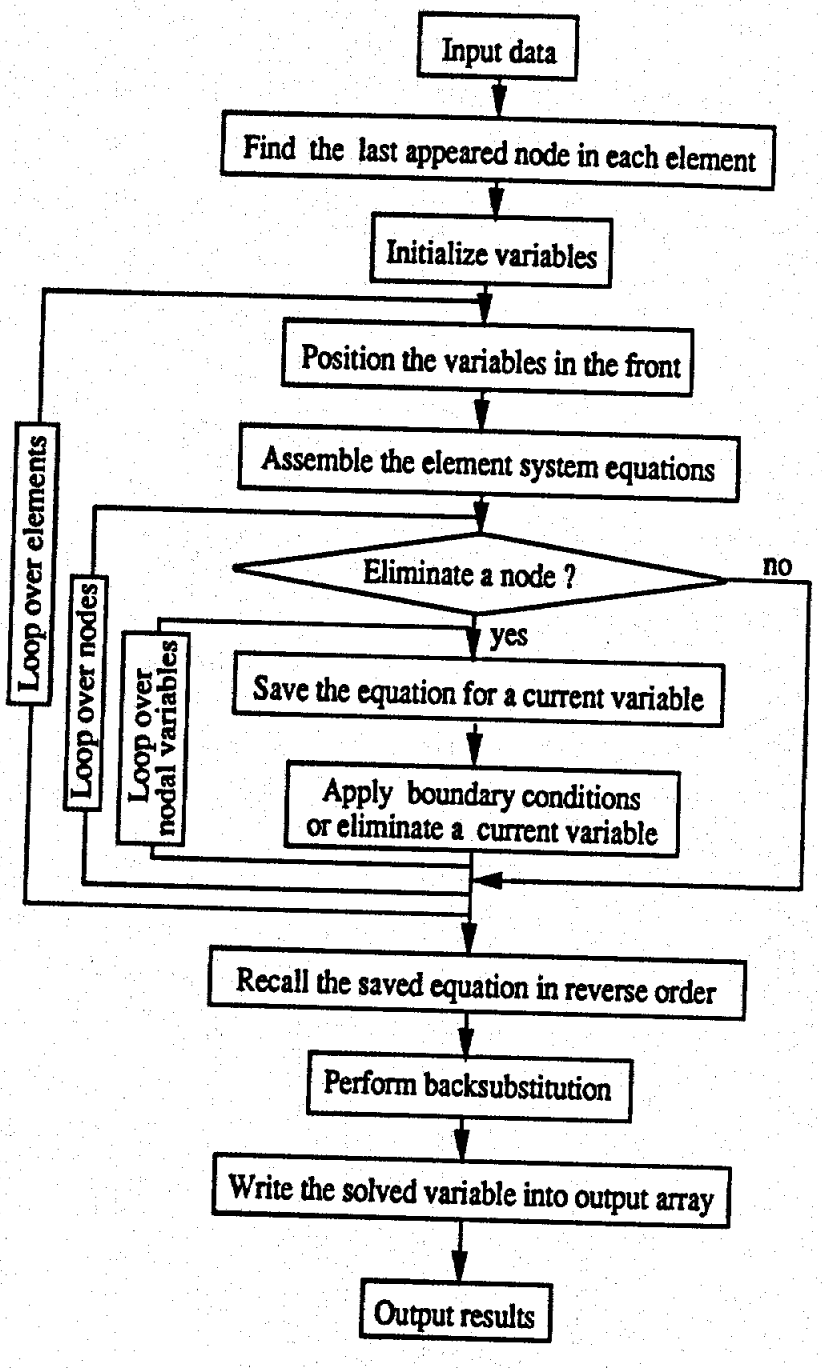

Figure 5.3: Flow chart of frontal technique.

5.5 Modeling and Numerical Results

5.5.1 Modeling

Figure 5.4 shows the anechoic chamber model with the four-wire antenna adapted for the finite element analysis. Since the chamber with the four-wire antenna has a symmetric structure, the analysis for the first quadrant of the chamber is sufficient. In the first quadrant of the chamber, an image plane is at the bottom and a symmetry plane at the left side for the vertically polarized excitation. The top and right side planes are perfect electric conductors covered with absorbers. An electric perfect conductor with absorber is used for the back wall except in the area where the wire is terminated. The front plane is modeled to be a perfect electric conductor without absorber. For such geometry the following boundary conditions are applied:

$\vec{H} \cdot \hat{n} = 0$ on a perfect electric conductor

(chamber walls and image plane)

$\vec{H} \times \hat{n} = 0$ on a perfect magnetic conductor(symmetry plane).

For the excitation of the antenna, a magnetic frill source model is used at the feed of the wire. For this, the magnetic field vectors are given at nodes around the wire at the feed so as to circulate the wire uniformly. This means that a constant current source is applied to excite the wire.

An exact model of the real chamber would require too many unknowns to compute with the available computer system. Therefore, the chamber is modified to reduce the number of nodes. The real absorbers on the walls are a wedge type in the tapered region and a pyramidal type at the quiet zone and backwall of the chamber. These absorbers are replaced with equivalent layers so that the layers have similar reflection properties to the absorber for the plane-wave incidence[93]. In the equivalent layers

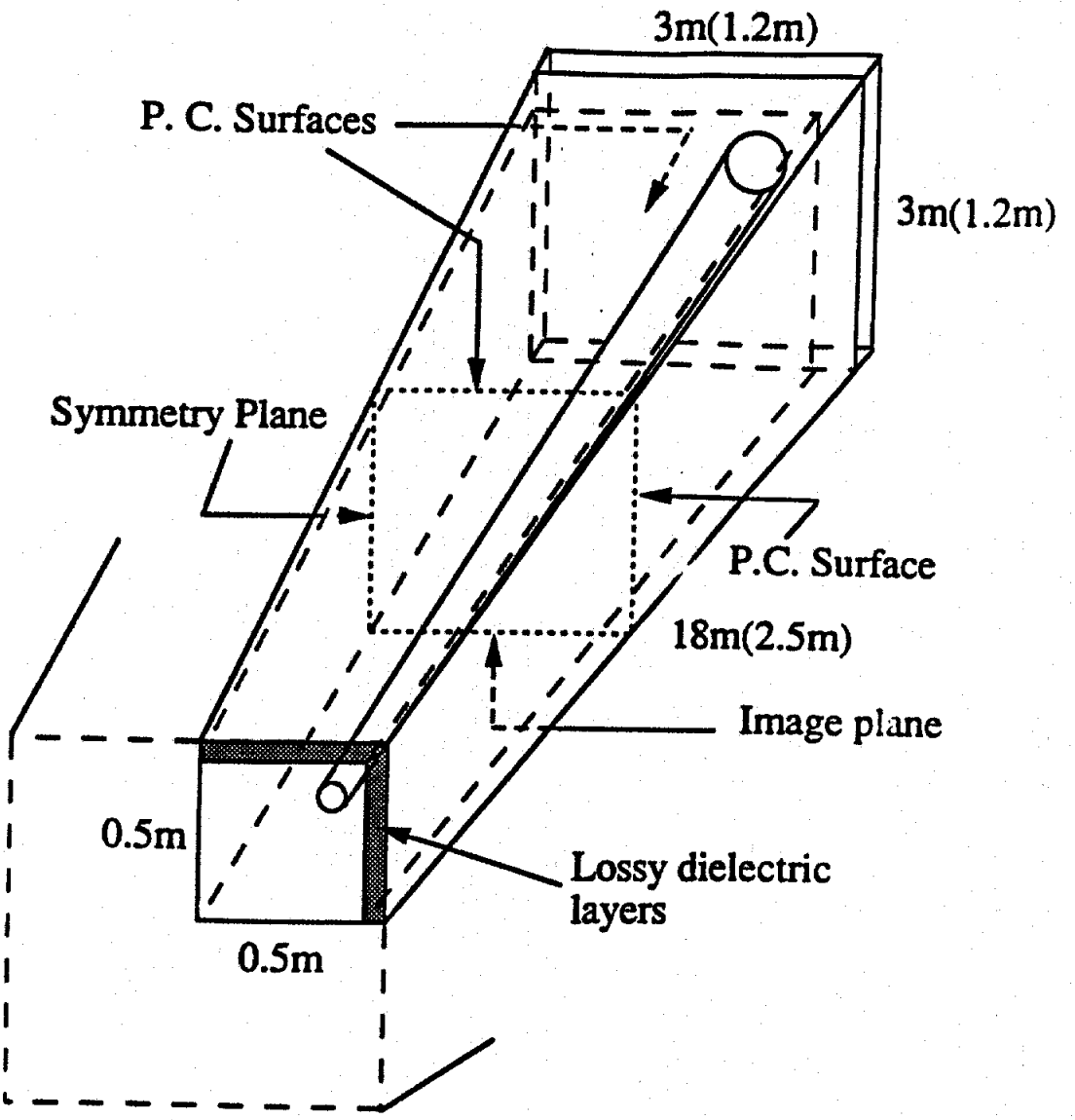

Figure 5.4: Modeling of the first quadrant of anechoic chamber with four-wire system. Absorbers are substituted with equivalent dielectric slabs that have similar reflection properties. Numbers in parentheses are dimensions for reduced size chamber.

the dielectric constant, ϵ_r^l, of layer l is given as

$$\epsilon_r^l = f^l(\epsilon_r - 1) + 1 \tag{5.35}$$

where f^l is the volume fraction of absorbing material at layer l and ϵ_r is the measured dielectric constant of the absorber. At the bottom of the absorbers, the volume fraction is one and at the top it is zero. Since the volume fraction varies linearly from top to bottom of the absorber, the dielectric constant of the equivalent layers has linearly varying profile from $\epsilon_r^l = 1$ to $\epsilon_r^l = \epsilon_r$, respectively. In this simulation, only two layers of equal thickness are used as the equivalent layers to reduce the unkowns. The dielectric constant of the layer close to the wall is the value measured in Chapter III. The layer adjacent to the air has the dielectric constant of $(1 + \epsilon_r)/2$. In Chapter III, several comparisons of the reflectivity between the absorber and the equivalent layers were made. Although the reflection coefficients of these equivalent layers are not exactly the same as those of the real absorbers, the effects of the equivalent absorbers on the response of the antenna are expected to be similar.

The other significant change is the size of the wire. The diameter of the real wire is four millimeters. It is important in the finite element technique that the sizes of adjacent elements should not change abruptly. If they change abruptly, the technique would generate serious numerical errors. With this in mind, the use of four millimeter diameter wire would require a huge number of elements for modeling the chamber of three meter width and height. Therefore, in order to reduce the number of elements, the diameter of the wire is assumed to be 7.5 centimeters at the feed point and tapered to 50 centimeters at the back wall. As a matter of fact, the chamber with wires is expected to guide a TEM wave at low frequencies(below several hundred megahertz). Therefore, the use of the thick wire is a justifiable assumption considering that the original goal of this analysis is to observe the low

frequency response.

In this chapter, two types of elements are considered for the analysis of the chamber with the four-wire antenna. One is a tetrahedral element with linear basis function and the other is a hexahedral element with a mid-side quadratic basis function. Since the use of the first one requires too many nodes to solve the whole system, the reduced geometry has been used. The dimensions of the reduced chamber are shown in the parentheses of Figure 5.4. In this case, the total number of nodes is dependent on the geometry rather than on the frequency. The reason is that the number of elements around the radiator, which is wire in our case, must be at least ten in order to obtain a physical solution. The use of hexahedral elements with mid-side nodes can simulate the radiator with fewer elements. Therefore, the full size chamber can be accurately analyzed. In this case, the size of element is bigger than the tetrahedral element and hence the total number of nodes is dependent on the frequency. For a good solution, the number of nodes must be at least eight per wavelength.

The numerical experiments were performed to see the effects of the penalty number. If the penalty number is zero, the solution is nonphysical. We obtained a physical solutions for the penalty numbers between 0.1 and 1.

5.5.2 Numerical Results

In the finite element simulation with tetrahedral elements, 7168 nodes and 31000 tetrahedral elements are used for a reduced chamber geometry. Figure 5.5 shows the discretization of the cross section into hexahedral elements. Each hexahedral element is discretized again into five tetrahedral elements.

By solving the system equations, the magnetic fields are obtained at each node. The current distributions are then obtained from the magnetic fields at the wire

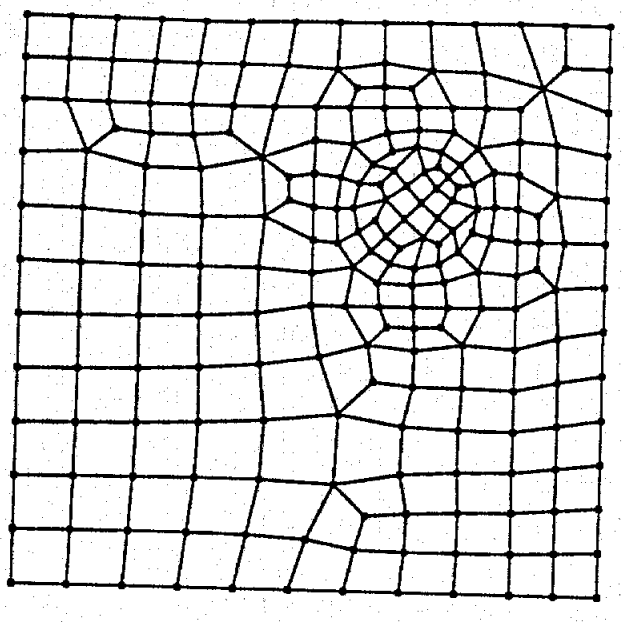

Figure 5.5: Discretization of cross section of the chamber with hexahedral elements. Each hexahedral element is divided into 5 tetrahedral elements.

surface from Ampere's law

$$I = \oint_l \vec{H}(\vec{r}) \cdot d\vec{l} \tag{5.36}$$

where the integration path l is around the wire following the right hand rule. Figures 5.6 through 5.8 show the current distribution on the wire for different terminations at 100, 150, and 300 MHz, respectively. These terminations include a short, an open, and a resistance loading. Figure 5.6 clearly shows the standing waves appropriate to the termination of the wire. For the open termination, the current at the end is zero and, for the short termination, it is maximum. When the 48 ohm resistance is used, the standing waves disappear. At 150 MHz similar behavior exists, but is less pronounced. It is interesting to note that the 48 ohm resistor, that worked very well at 100 MHz, is not effective here. This is not surprising, since the optimum loading, in general, is a function of frequency. At 300 MHz the termination barely affects the

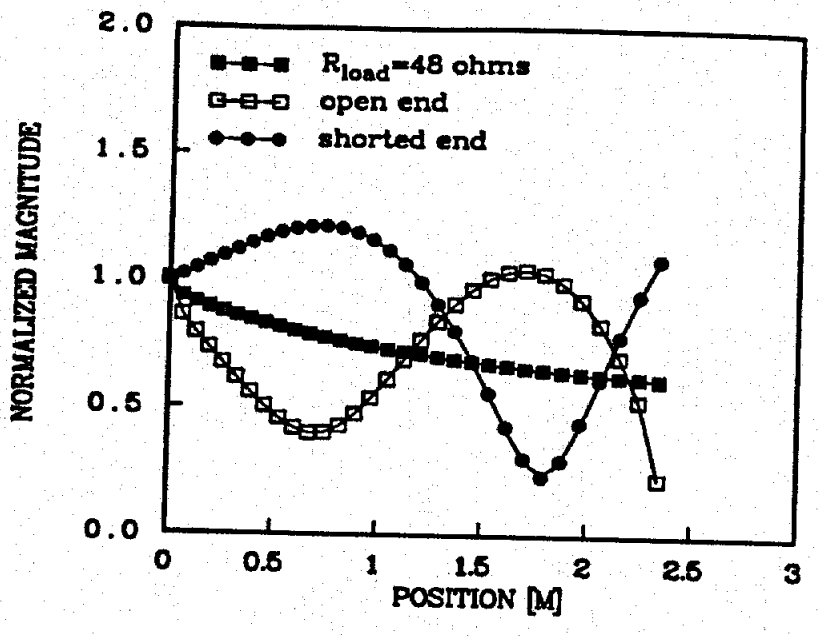

Figure 5.6: Current distribution on the wire at 100 MHz with different termination. The currents are normalized to the input current.

current on the wire because, at this frequency, the current has already decayed before reaching the end. Also, at the end, the absorber absorbs the remaining current that reaches the end.

Figure 5.9 shows the discretization with hexahedral elements with mid-side nodes. With these elements, the full size chamber is discretized into 1998 elements with 9359 nodes. The computed current distributions on the wire are shown in Figures 5.10 through 5.12 with a short termination to the back wall at 30, 50, and 70 MHz, respectively. In these figures, the solid lines represent the current magnitude normalized to the input current and the dotted lines represent the phase.

To obtain the field plots, the computed magnetic fields are assumed to be elliptically polarized at a given cross section of the chamber. Figure 5.13 shows the

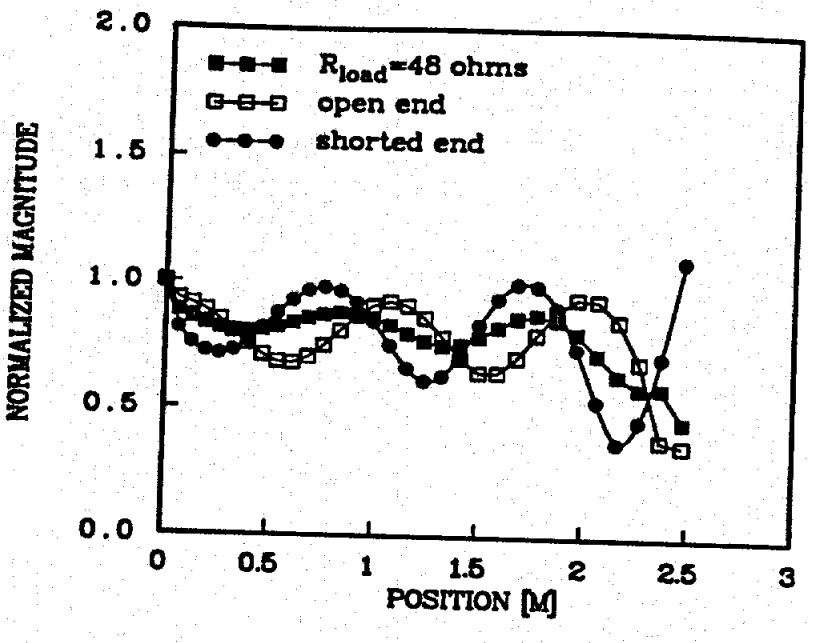

Figure 5.7: Current distribution on the wire at 150 MHz with different termination. The currents are normalized to the input current.

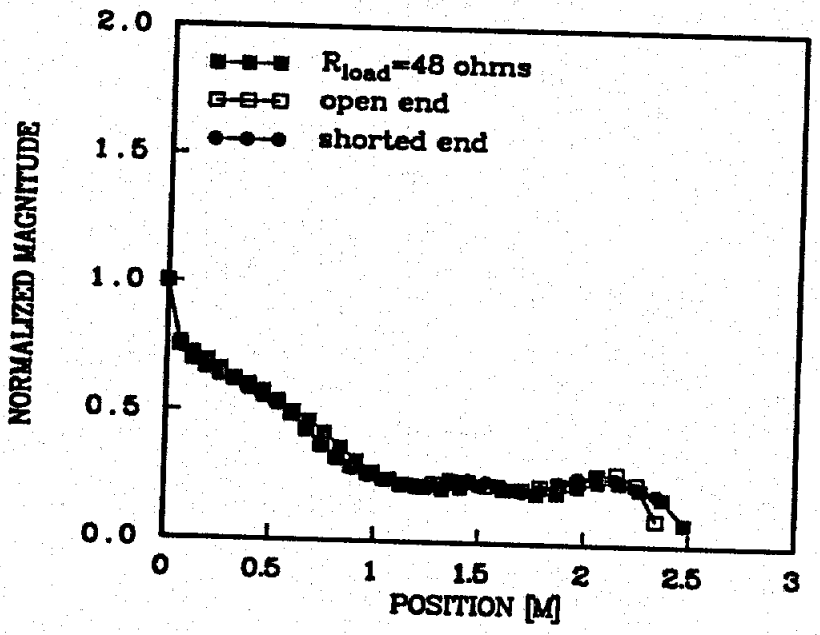

Figure 5.8: Current distribution on the wire at 300 MHz with different termination. The currents are normalized to the input current.

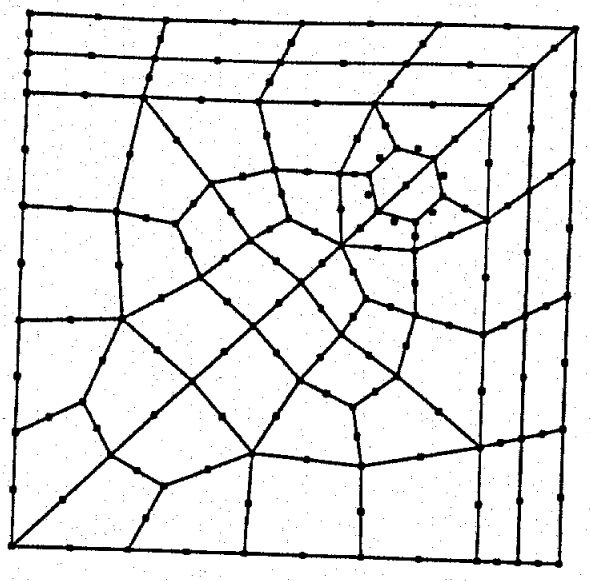

Figure 5.9: Discretization of the cross section of the chamber with hexahedral elements with mid-side nodes.

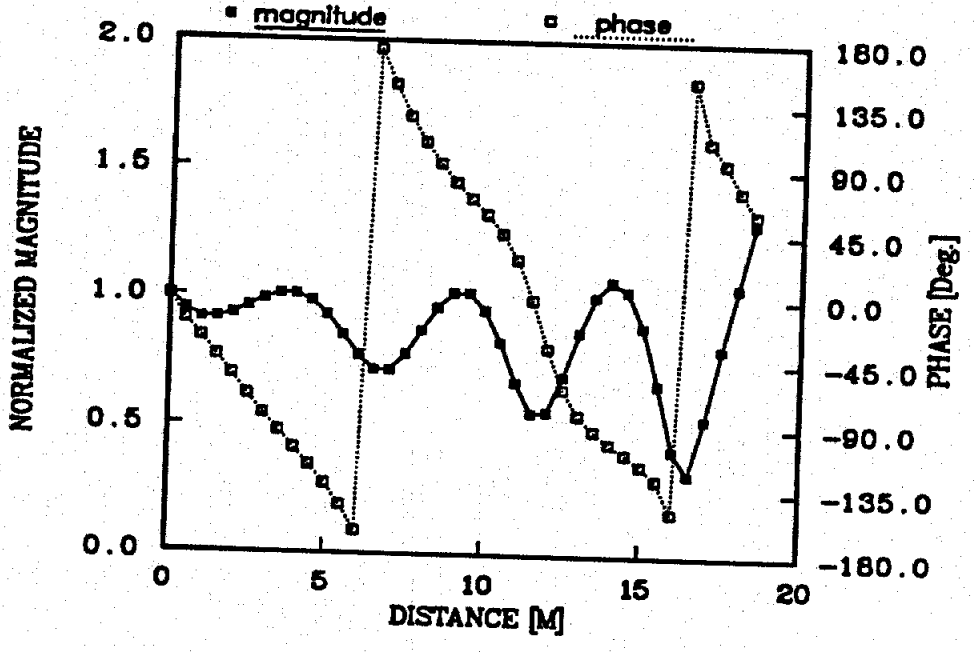

Figure 5.10: Current distribution at 30 MHz. The wires are terminated to the backwall with short. Hexahedral elements with mid-side nodes are used.

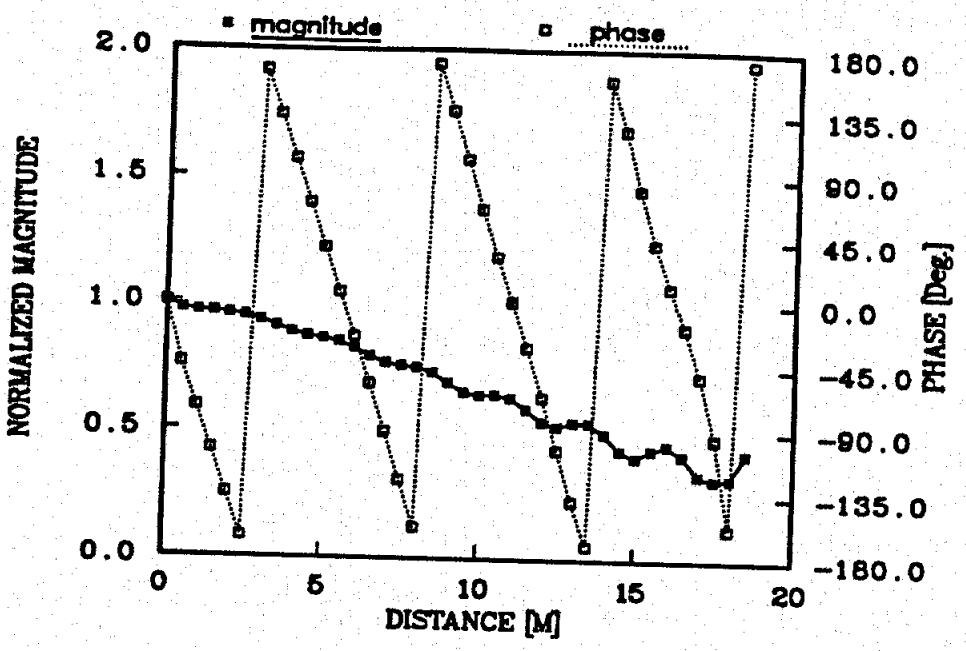

Figure 5.11: Current distribution at 50 MHz. The wires are terminated to the back-wall with short. Hexahedral elements with mid-side nodes are used.

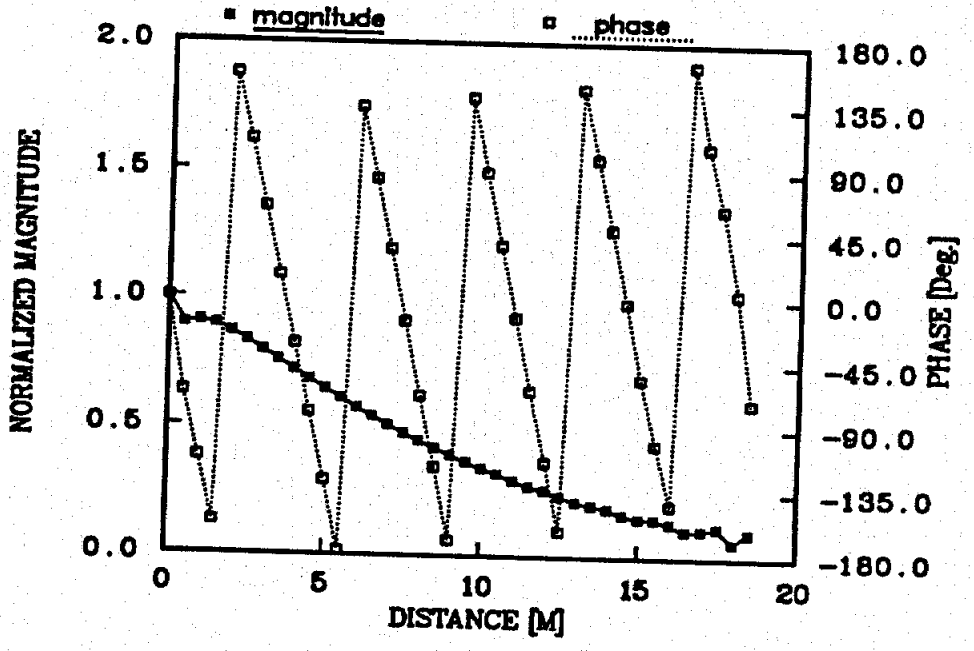

Figure 5.12: Current distribution at 70 MHz. The wires are terminated to the back-wall with short. Hexahedral elements with mid-side nodes are used.

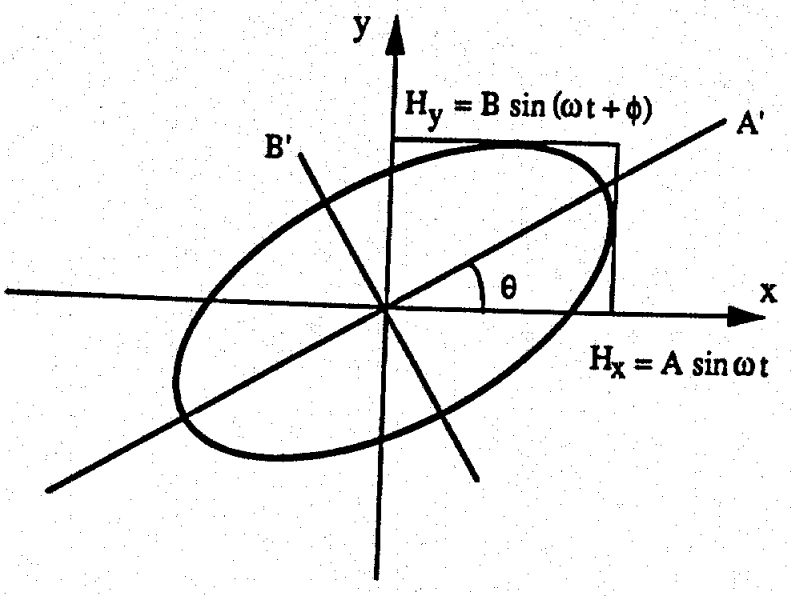

Figure 5.13: Elliptically polarized magnetic fields at a cross section of the chamber.

polarization ellipse. If the field components are expressed at a cross section as

$$H_x = A sin\omega t \tag{5.37}$$

$$H_y = B sin(\omega t + \phi) \tag{5.38}$$

the lengths of two axis of the ellipse, A' and B', are written as

$$A' = \frac{1}{\sqrt{B^2 cos^2\theta - AB cos\phi sin2\theta + A^2 sin^2\theta}} \tag{5.39}$$

$$B' = \frac{1}{\sqrt{B^2 sin^2\theta - AB cos\phi sin2\theta + A^2 cos^2\theta}} \tag{5.40}$$

where θ, the tilted angle of A' from x axis, is

$$\theta = \frac{1}{2} tan^{-1} \frac{2AB cos\phi}{A^2 - B^2}$$

The major axis of the ellipse is the longer one of A' and B' and the minor axis the shorter one.

With this expression, the computed magnetic fields are drawn in Figures 5.14 through 5.16 for 30, 50, and 70 MHz, respectively. Figure 5.17 shows the field

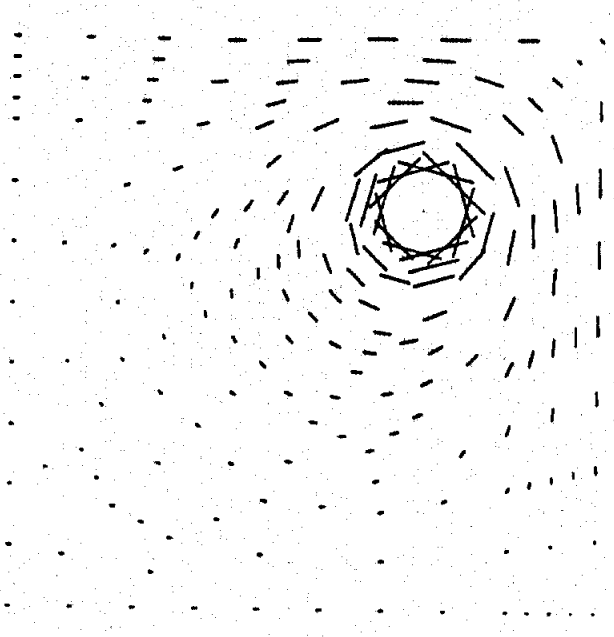

Figure 5.14: Field distribution at a cross section of 15 meter distance from feed point at 30 MHz. The wires are terminated to the backwall with a short. Hexahedral elements with mid-side nodes are used.

variation obtained by this analysis at 50 MHz. In the figure, (a) and (b) show the magnetic field intensity variation along the horizontal and vertical axis, respectively. The field intensities are normalized to the intensity at the center point. The plane used in these figures is the cross section at 14 meters from the feed. Figure 5.18 shows the field variation along the propagation direction at 50 MHz. The fields are normalized to the fields at 14 meters from the feed. As expected, the fields decrease as an inverse function of distance. According to these figures, the fields are uniform within $\pm$ 1 dB in the 0.5 meter radius spherical test area.

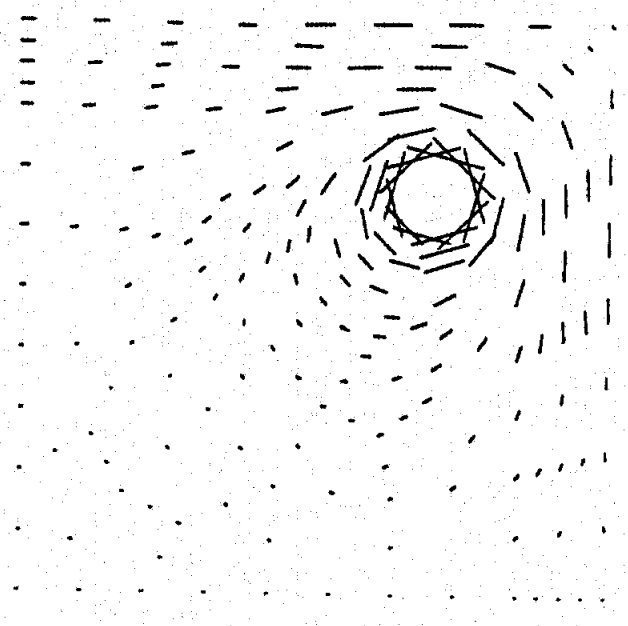

Figure 5.15: Field distribution at a cross section of 15 meter distance from feed point at 50 MHz. The wires are terminated to the backwall with a short. Hexahedral elements with mid-side nodes are used.

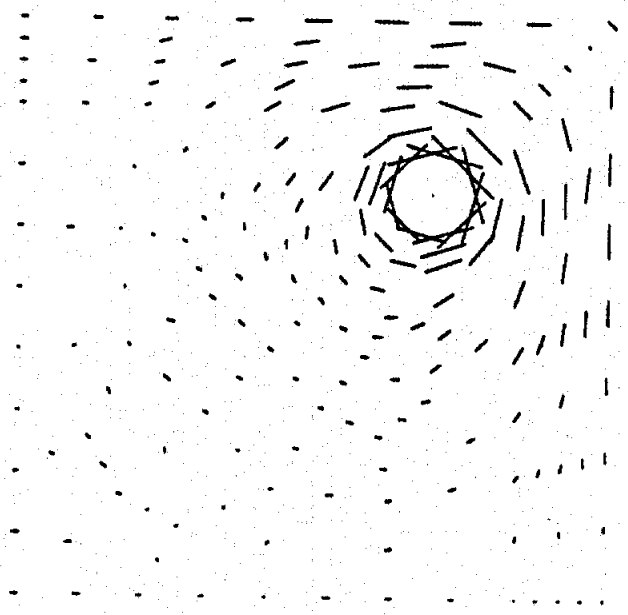

Figure 5.16: Field distribution at a cross section of 15 meter distance from feed point at 70 MHz. The wires are terminated to the backwall with a short. Hexahedral elements with mid-side nodes are used.

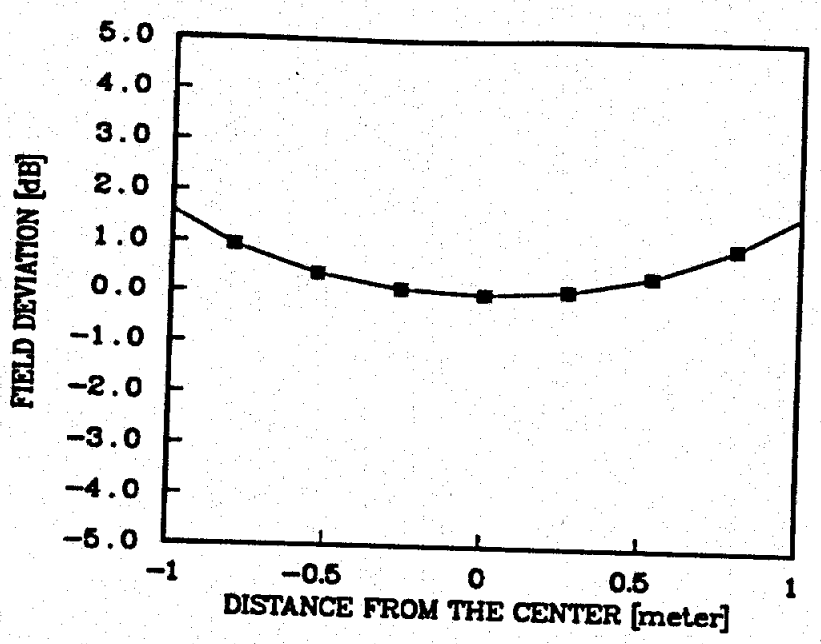

(a) Horizontal

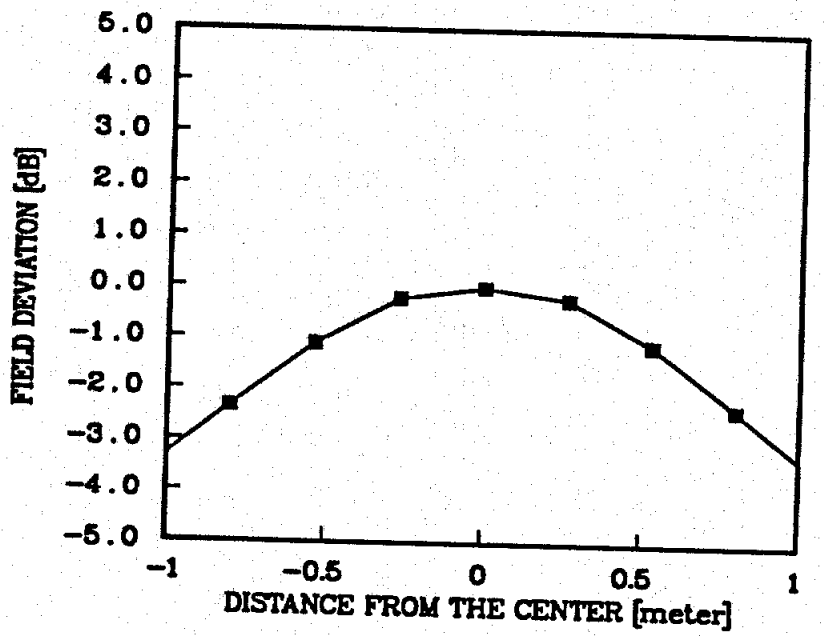

(b) Vertical

Figure 5.17: Field variation along the center line at 50 MHz.

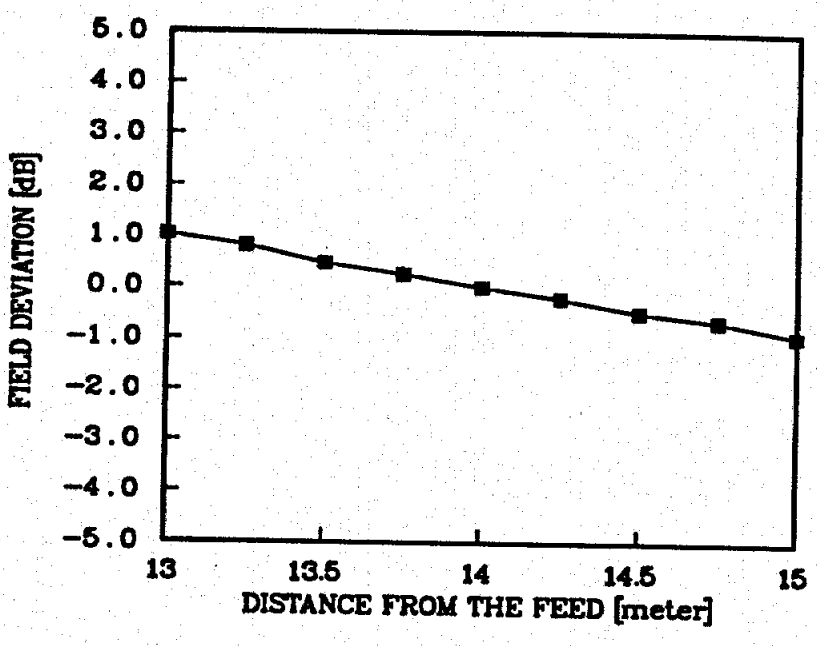

Figure 5.18: Field variation along the propagation direction at 50 MHz.

CHAPTER VI

IMPLEMENTATION AND MEASUREMENTS

The four-wire antenna was built and installed in the tapered anechoic chamber at the University of Michigan Radiation Laboratory. The performance of the antenna was tested by measuring the input impedances and the resultant field distributions. The antenna showed good performance in producing a uniform field at the test area and has a good impedance behavior over a broad frequency range. Using the four-wire antenna system, surface current measurements were conducted to demonstrate EMC capabilities[96]. In addition, electromagnetic reflection or backscattering measurements were performed to show the potential of this antenna for radar cross section (RCS) measurements in the low frequency regime.

Section 6.1 describes the construction of the four-wire antenna in the anechoic chamber. In section 6.2, electrical property measurements of the system are described and performed. For measuring the input impedance, a small four-wire antenna model was constructed and measured in free space. Also, the input impedance of the full size four-wire antenna was measured when it was installed in the chamber by measuring the S-parameters at the feed point. The field intensity in the test area was measured to show the uniformity of the field. In section 6.3, backscattering measurements are presented for a tilted cylinder. Surface current measurements are presented in

section 6.4 for induced surface currents on a model aircraft.

6.1 Installation of the Four-wires in Anechoic Chamber

Even though it has been analytically shown that the optimum arrangement of the four wires is not symmetrical[97], a symmetric arrangement was chosen. One of the reasons for this choice is that it allows the user to change the polarization of the antenna by simply changing the feed connections. Another reason is that the symmetric arrangement is more compatible with the square cross section of the anechoic chamber.

Figure 6.1 shows the drawing of the tapered anechoic chamber with a four-wire system and instrumentation set up for S_{11} or reflectivity measurement. The overall dimensions of the chamber are 5.4 meters wide, 18 meters long, and 5.4 meters high. The anechoic treatment consists of 1.8 meter deep pyramidal absorbers on the target endwall of the chamber; 0.6 meter and 0.45 meter deep pyramidal absorbers, and 0.3 meter wedge absorbers on the side walls, ceiling and floor surfaces of the 0.45 meter $\times$ 0.45 meter $\times$ 0.56 meter test region; and 0.45 meter deep pyramidal and 0.3 meter deep wedge absorbers on all surfaces of the tapered section. The 12.85 square meters of the test region floor surface are treated with 0.6 meter deep walkway absorber.

At the feed point, each wire of the four-wire system starts with a one meter long brass tube (4 mm diameter) followed by an outer shield conductor of RG-58/U coaxial cable, which has the same diameter as the brass tube. The top two wires are connected to one SMA connector with a "V" form and the bottom two wires to the other SMA connector symmetrically. The top and bottom wires also have the same "V" form with each other. The two SMA connectors are mounted on the metal plate as closely as possible (1.2 centimeters) in a vertical line. For the mechanical

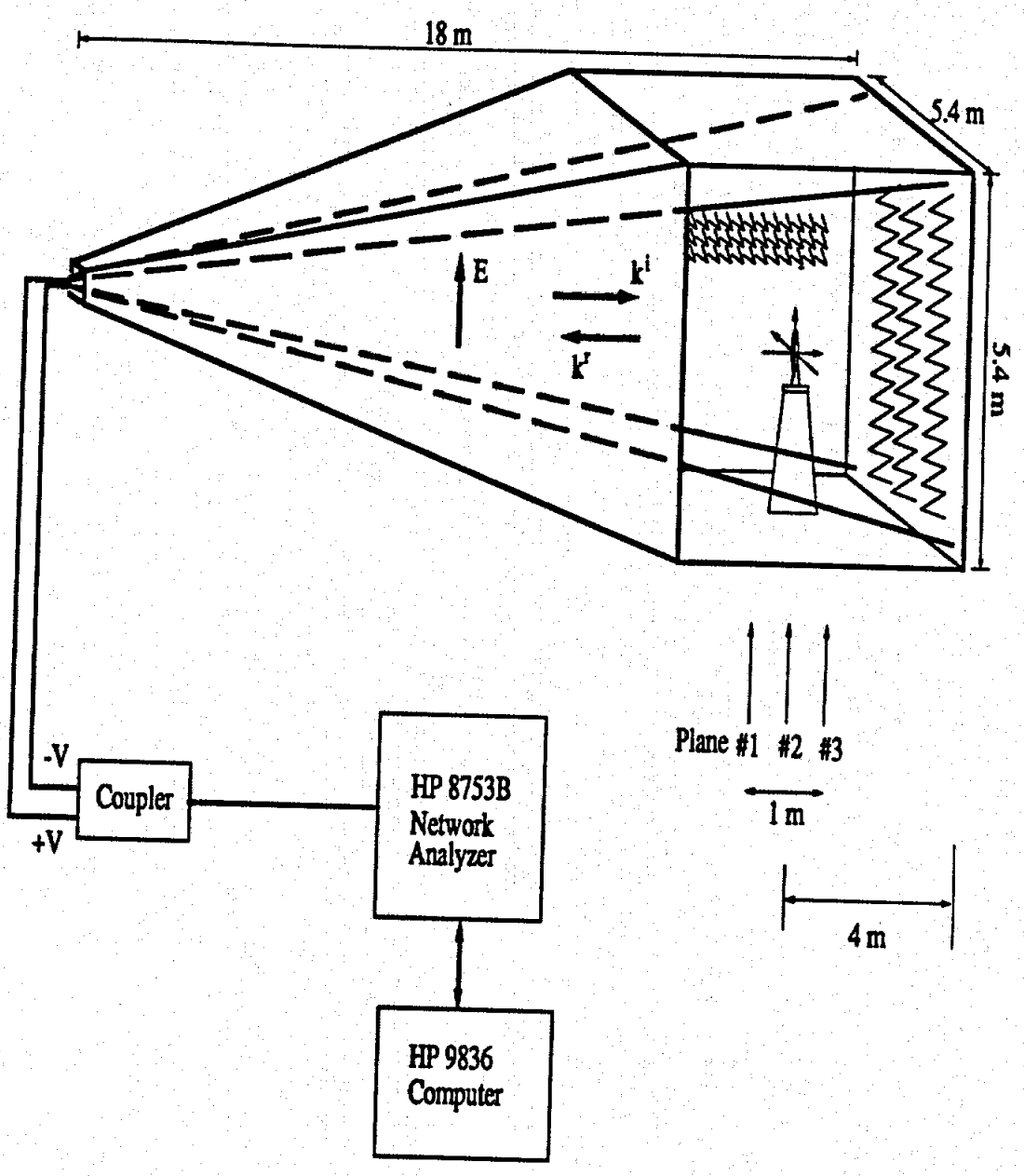

Figure 6.1: The tapered anechoic chamber with four-wire system with equipment set up for field and backscattering measurements.

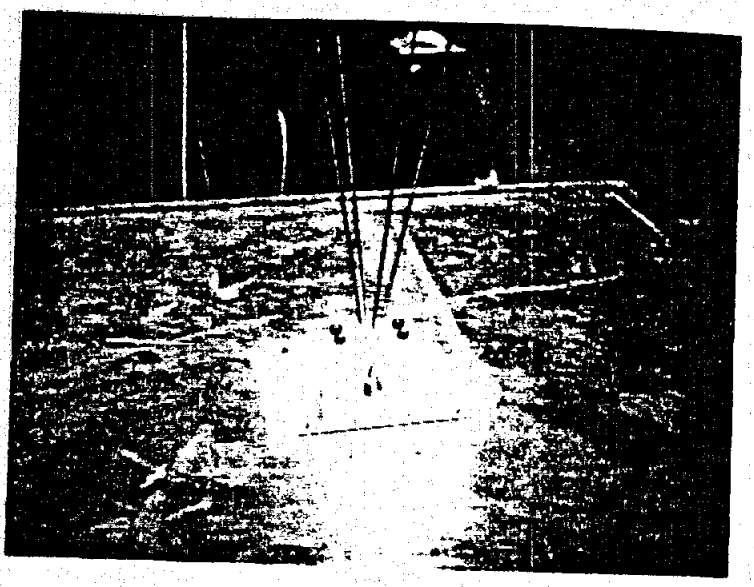

Figure 6.2: The four-wire antenna feed showing the support plexiglass block.

plate as closely as possible (1.2 centimeters) in a vertical line. For the mechanical support of the wires at the feed, a plexiglass block is drilled in a "V" form and tubes are inserted and glued into the holes. Figure 6.2 shows a photograph of the feed including the plexiglass block. In order to terminate the wires on the back wall, holes are drilled through the absorber and the back wall. The antenna wires are passed through these holes and secured. However, due to the 18 meter length of the wires, the wires droop about 50 centimeter at their midpoint. To correct this droop, two ropes are stretched along the top of the chamber and each wire is supported by two strings that are attached to these ropes. With these ropes, the droop is reduced to less than 3 cm in the radiation area of the wires. Figure 6.3 shows photographs taken inside the chamber. The upper photo shows the feed plate with the four wires coming out diagonally and the two ropes at the top. The lower photo shows the wire going through the back wall at the crevice (or the low spot) in the pyramids.

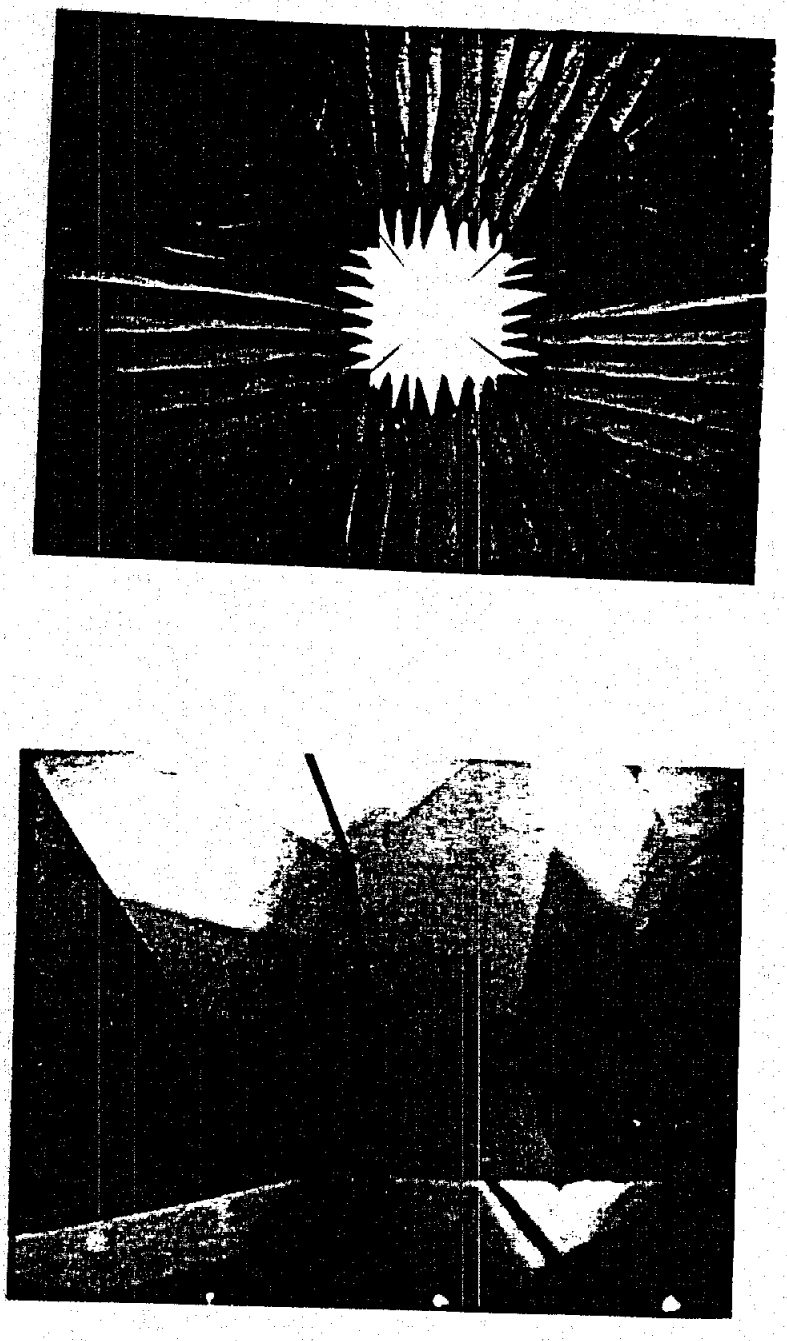

Figure 6.3: Photographs of the antenna wires in the chamber. Upper photo shows the feed point. Lower photo shows one of the wires going through the back wall.

6.2 Electrical Property Measurements

6.2.1 Input Impedance Measurements

The antenna input impedance was measured on two versions of the antenna. One is the antenna in free space using a ground plane configuration and thus needing only a half of the antenna (equivalent to monopole vs. dipole), and the other is the full antenna in the anechoic chamber.

Free Space Version

Using the same feed geometry, a smaller version of the four-wire antenna was constructed, but using an image plane. In this case, only half of the antenna with single port excitation is used. (This is like feeding and measuring a monopole when data for a dipole are desired.) This antenna has a single V-element fed through a SMA connector which is mounted on a ground plane (or image plane) as is shown in Figure 6.4. The angle of the V-element is 8.6 degrees and the angle between the V-element and ground plane is 4.3 degrees. The V-element consists of two brass tubes that are one meter in length and four millimeters in diameter. Impedance of the structure was measured on a network analyzer and the results are shown in Figure 6.5. The oscillations in the curves for R and X are caused by reflections from the ends of the wires. When the signal is range gated to remove the end reflections, the smooth curves are obtained. The real part shows about 80 ohms and the imaginary part is near 0 ohm. For the four-wire antenna, the impedance would be twice, or 160 ohms.

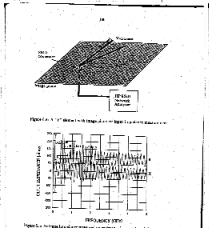

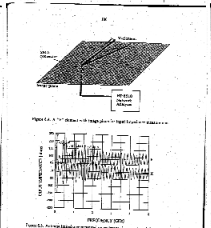

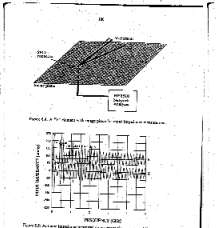

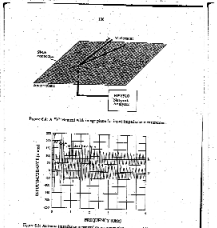

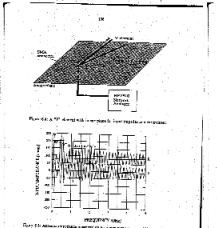

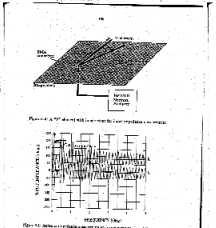

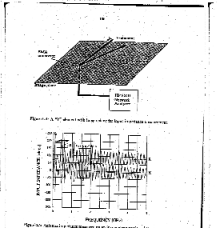

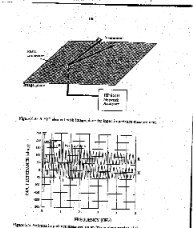

Four-wire Antenna in the Chamber

The input impedances of the four-wire antenna in the anechoic chamber was measured by measuring the two-port S-parameters of the antenna. Figure 6.6 shows the two port network representation of the four-wire system. In the operation of the antenna, ports 1 and 2 are excited with voltages of the same magnitude but with 180 degree phase difference. The antenna impedance is then twice the port impedance. Using a two-port measurement procedure, the impedance of an antenna driven differentially can be obtained as follows.

Assume both sources are matched and a's and b's represent the voltage waves when the circuit is excited in differential mode. The S-parameters are defined as done in the Hewlett Packard literature[57]. For the differential (and matched) excitation,

$$a_1 = -a_2$$

Then

$$b_1 = a_1 S_{11} + a_2 S_{12}$$

or

$$\frac{b_1}{a_1} = S_{11} - S_{12}$$

and thus, the port impedance is

$$Z_p = \frac{1 + S_{11} - S_{12}}{1 - S_{11} + S_{12}} Z_0$$

where Z_0 is 50 ohms. The antenna input impedance is then simply

$$Z_{in} = 2Z_p$$

Figure 6.7 shows the measured input impedance of the four-wire antenna in the anechoic chamber. This input impedance has similar behavior to that measured

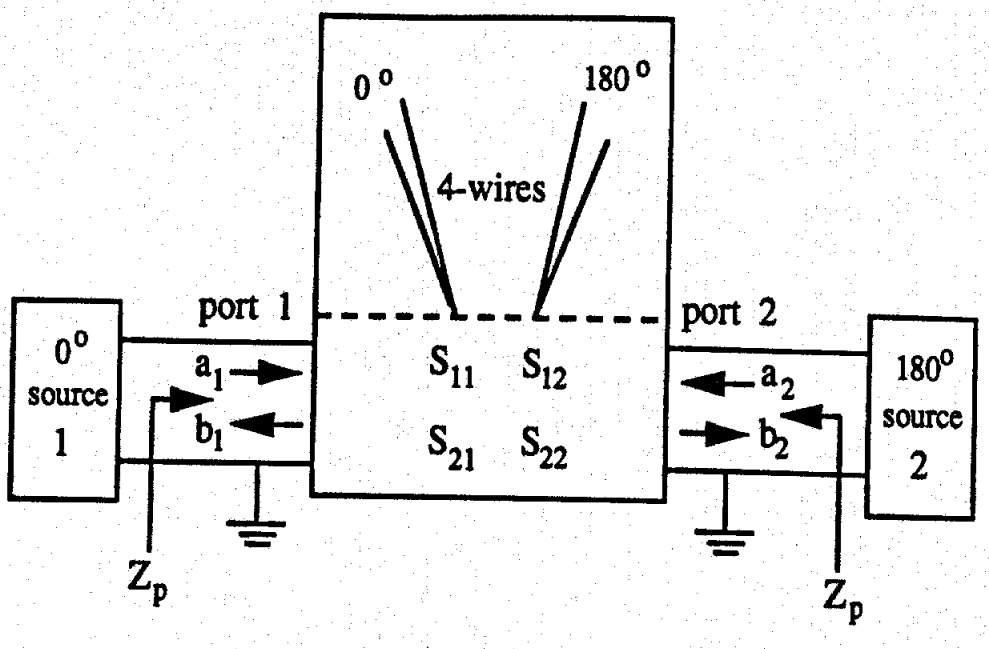

Figure 6.6: Two port representation of the four-wire antenna in the anechoic chamber.

from the antenna in free space, but there are also differences. The real part for the antenna in the chamber is about the same magnitude (100 ohms), but varies more with frequency. The major difference between the two antennas is that the chamber antenna has an inductive reactive component rather than zero reactance for the free space version. The difference could be attributed to a different reference plane in the calibration of the network analyzer. For the free space version antenna the reference plane was at the antenna base, whereas for the chamber antenna, the reference plane was at the connector. Of course, the chamber antenna is expected to have somewhat different impedance characteristics due to the interaction of the antenna with the chamber walls.

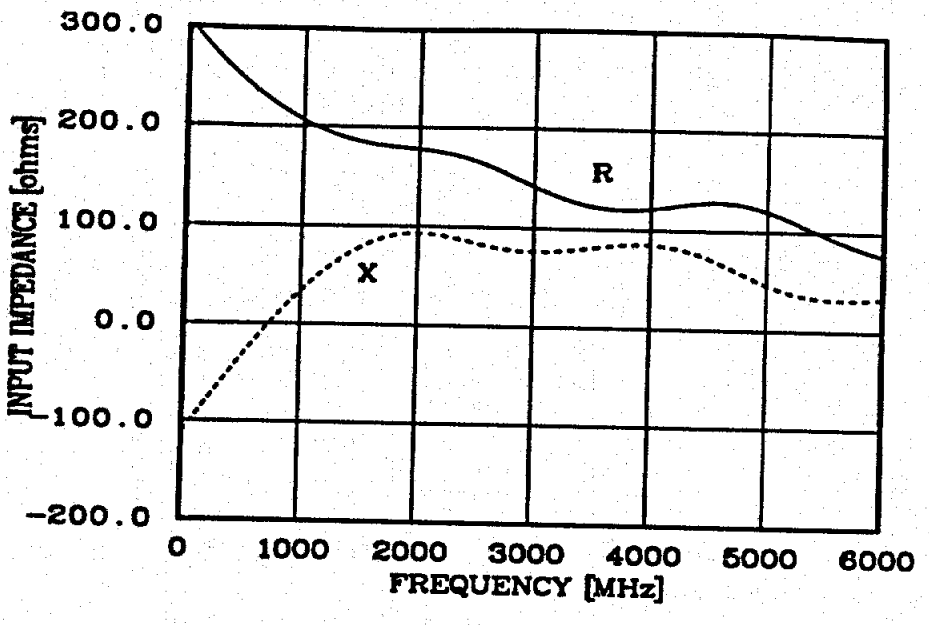

Figure 6.7: Measured input impedance of the four-wire antenna in the anechoic chamber.

6.2.2 Field Measurements

The monostatic radar equation is written[98] as

$$\frac{P_r}{P_t} = \frac{G^2\lambda^2\sigma}{(4\pi)^3 R^4} \tag{6.1}$$

where

P_r : power returned from target

P_t : power transmitted from antenna

G : antenna gain

λ : wavelength

σ : scattering cross section of target

R : distance from antenna to target.

The power density, S_s, of the incident wave on the scatterer is given by

$$S_s = \frac{P_t G}{4\pi R^2} \tag{6.2}$$

By substituting Eq.(6.2) into Eq.(6.1) for G, we obtain

$$P_r = \frac{\sigma\lambda^2}{4\pi P_t} S_s^2 \quad \text{or} \quad S_s = \sqrt{\frac{4\pi P_r P_t}{\sigma\lambda^2}} \tag{6.3}$$

According to Eq.(6.3), we see that the incident power density on a scatterer is proportional to the square root of the returned power, provided that the scatterer is characterized by Radar Cross Section σ. Consequently, the field distribution can be obtained by measuring the power returned from the target located at the corresponding scanning point.

Figure 6.8 shows the block diagram of the system set-up used for the field mapping measurements. A 0-180 degree hybrid coupler (0.1 MHz – 2000 MHz) was used to obtain the differential mode signal for the wires. The two top wires were fed at 0 degree phase and the two bottom wires were fed at 180 degree phase. Connectors were made using equal lengths of semirigid coaxial cables(L_1, L_2 in Figure 6.8) to preserve the signal balance. For the scatterer, a 12.875 inch diameter flat circular plate was used. The measurements were made with the HP8753B Network Analyzer, with the sweep frequency range set from 50 MHz to 1550 MHz.

Figure 6.9 shows the time domain response of the whole system, obtained by Fourier transforming the measured frequency domain data. The first peak, which is denoted with "A" in the figure, is due to the reflection at the coupler and the second peak, "B", is due to the reflection at the feed of the wires. A peak between "B" and "C" seemed to be due to the fire extinguishers on the ceiling of the chamber. The peaks denoted with "C" and "D" are due to the reflections at the backwall and the open ends of the wires, respectively. In this case, there was no loading applied at the end of the antenna wires. The wires were pulled through holes in the back wall, tied to anchors, but not electrically connected. By loading even with a lumped resistance, the last peak, "D", can be eliminated. Figure 6.10 shows the time domain response of

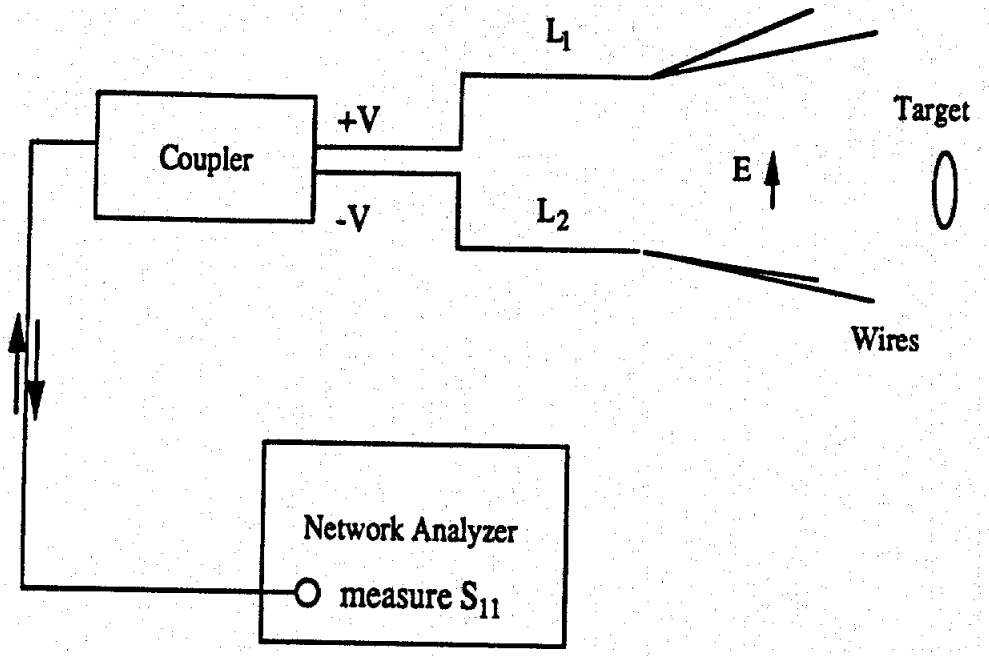

Network Analyzer	Hewlett Packard, 8753B
Coupler	Anzac, Model H-9
L1, L2	Lines adjusted for phase match
Wires	Brass Tube (1 m), plus
	Outer Conductor of RG-58/U
Target	12.875 inch Diameter Circular Plate

Figure 6.8: The block diagram of the four-wire system for field measurements.

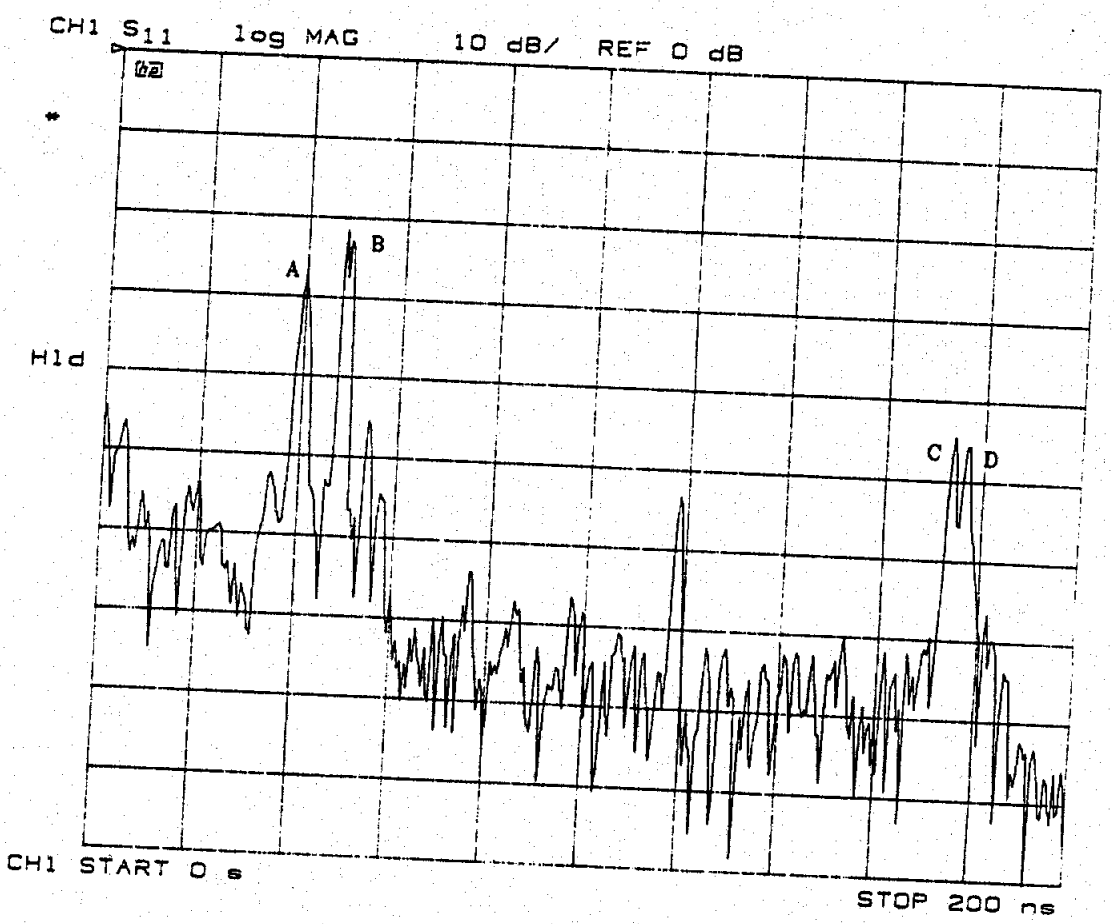

Figure 6.9: The time domain response of the four-wire system.

the system with a 120 ohm lumped loading resistance. The peak, "D", of Figure 6.9 has disappeared in Figure 6.10. Nevertheless, there still exist significant reflections at the feed of the antenna and the back wall of the chamber. The reflection at the back wall is due to the poor performance of the absorbers at low frequencies and is attributed to reflection of the space wave rather than the current on the wires.

Since the reflection from the target (12.875 inch diameter flat circular plate) is quite small compared to the other reflections, a special procedure is required. For this, the response of background is subtracted from the response with the target present. Figure 6.11 shows the time domain response after subtraction. By subtracting, a 30 dB signal to noise ratio is achieved in the time domain as shown in the figure by marker 1. Since the noise at the feed and coupler was still high (the first peaks in Figure 6.11), it was removed by software gating. The gate span was five nanoseconds and the gate shape was normal. The five nanosecond gate span was chosen to include the direct ray and the rays bounced off the walls. In the field measurements, the test area was scanned with the circular plate every 10 inches in horizontal, vertical, and propagation directions (80 in. $\times$ 60 in. $\times$ 30 in.). Figures 6.12 through 6.14 show the field variations in horizontal and vertical axes of three crosscuts that are shown in Figure 6.1. In each figure, the field intensities are normalized to the field at the center of the plane. These figures show the field distributions are uniform as expected. Within a 40 inch diameter circle in each plane, the field deviation is $\pm$ 0.5 dB for most frequencies.

In the propagation direction, the field intensities were measured along the center line of the chamber from 190 inches to 120 inches measured from the back wall. The intensities are normalized to that of 160 inches from the back wall and are shown in Figure 6.15. As is shown in the figure, the fields tend to decrease as an inverse

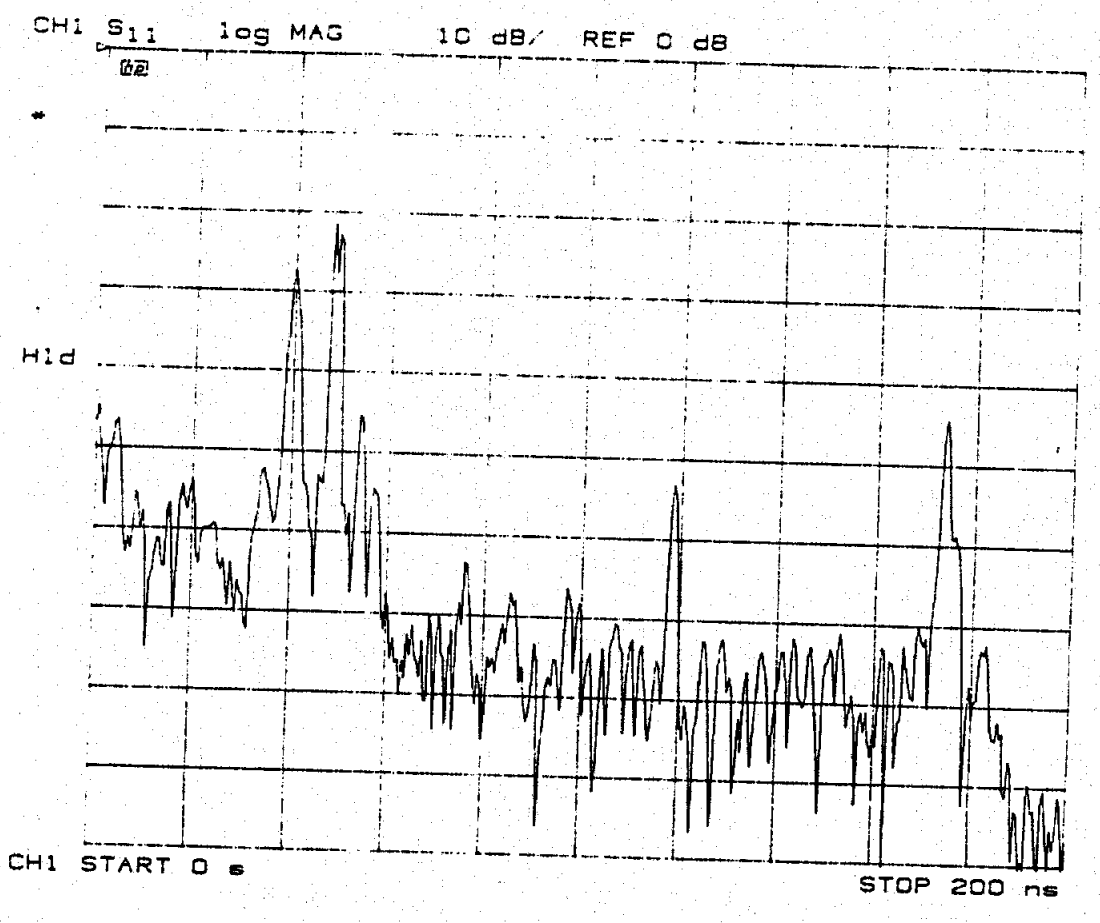

Figure 6.10: The time domain response of the four-wire system with 120 ohms loading at the end of wires.

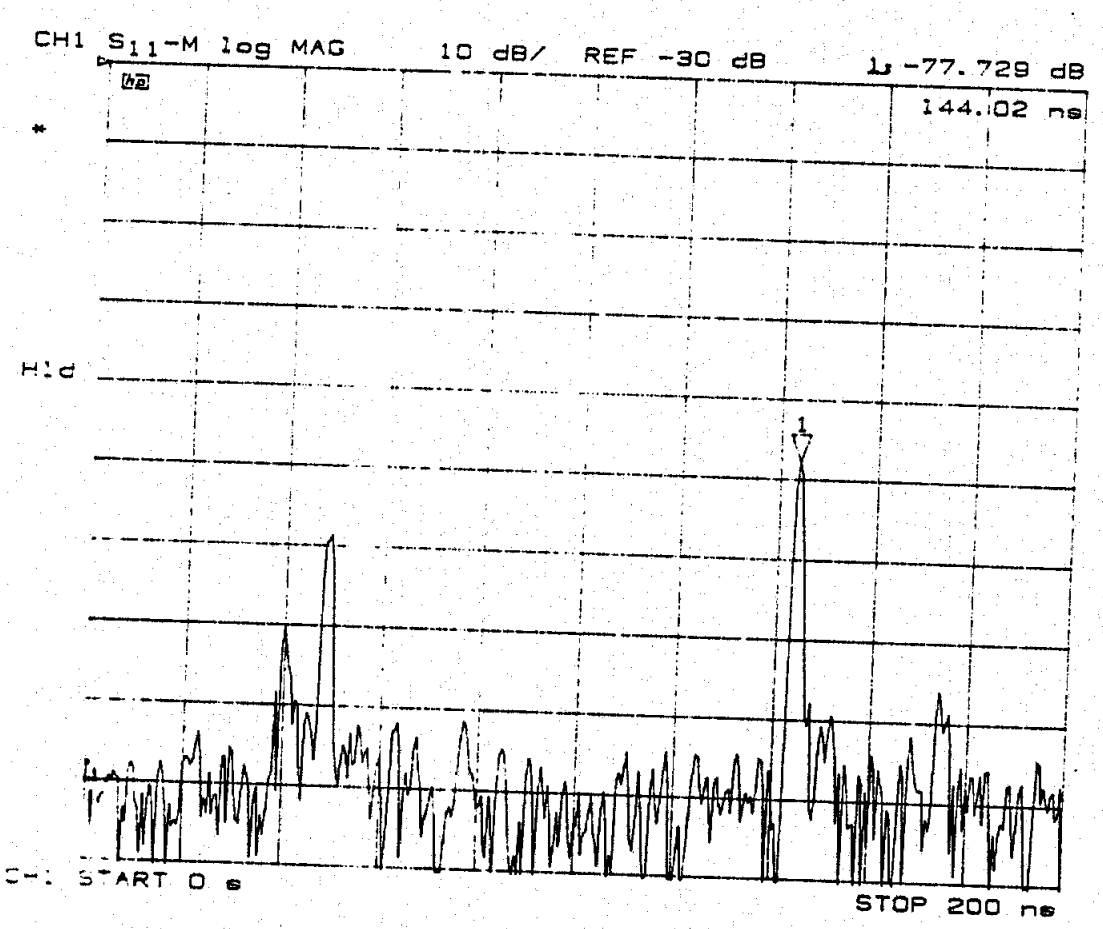

Figure 6.11: Subtracted signal by background in time domain.

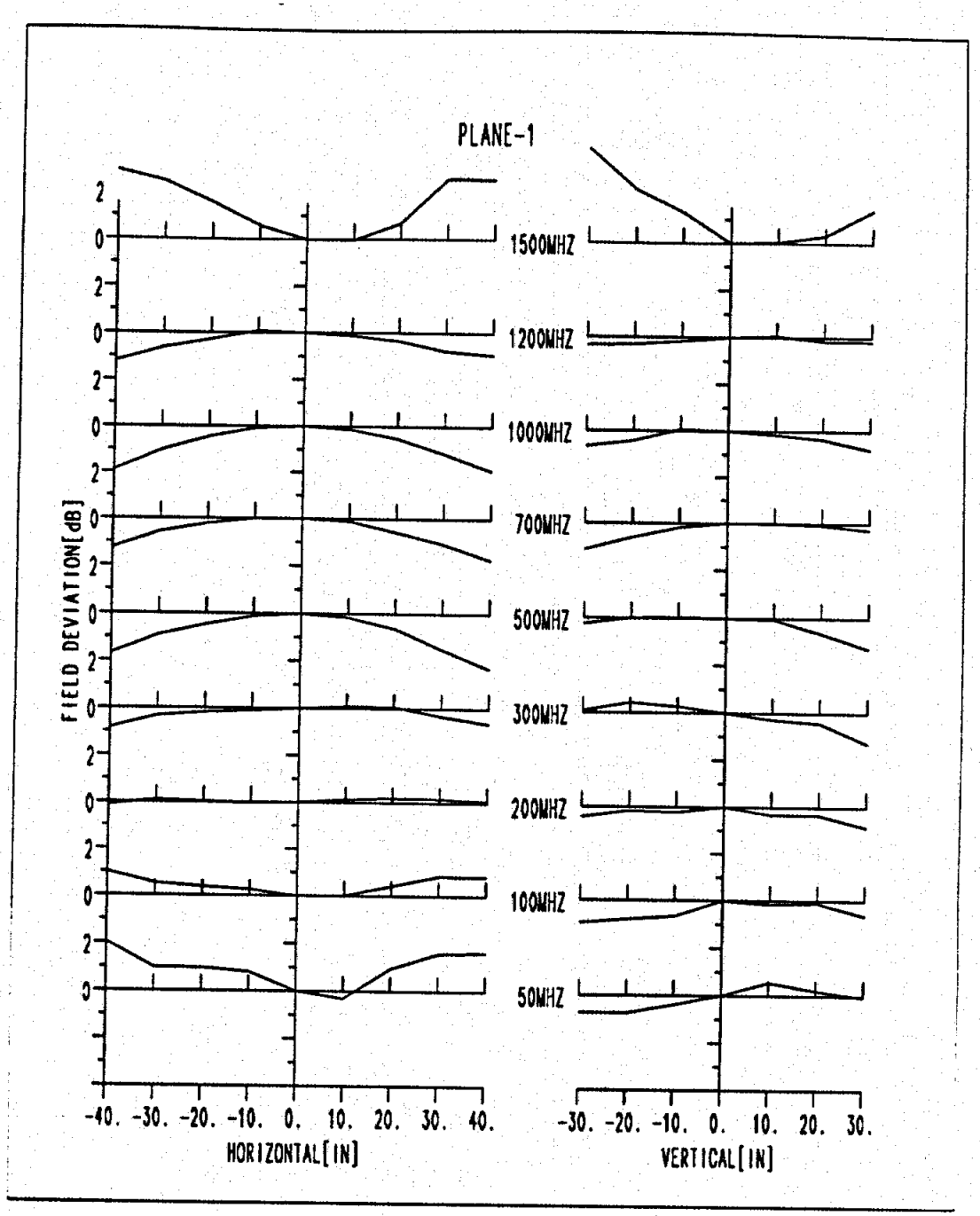

Figure 6.12: Measured field intensity in horizontal and vertical direction of plane 1 (normalized to the intensity at center point of plane 1).

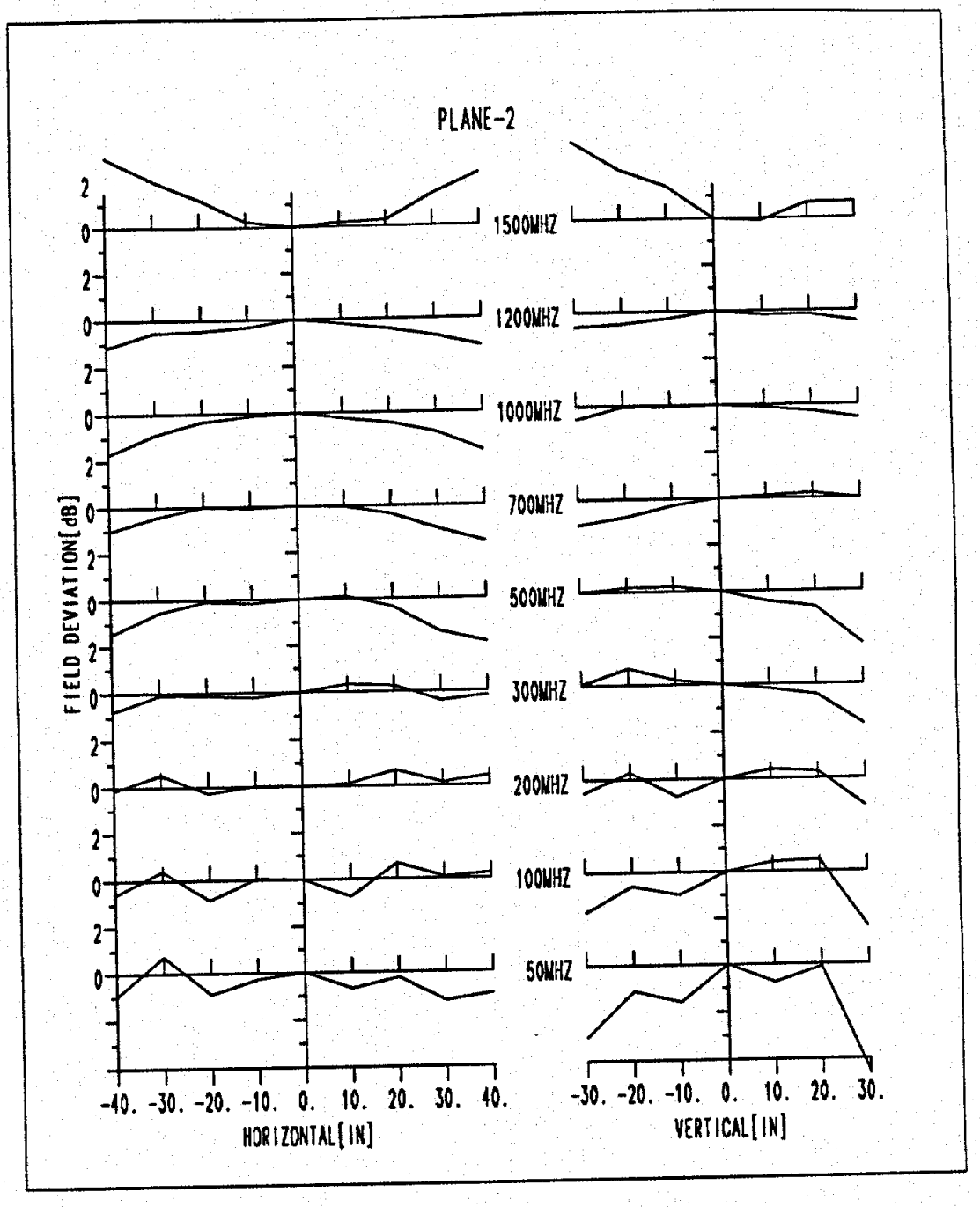

Figure 6.13: Measured field intensity in horizontal and vertical direction of plane 2 (normalized to the intensity at center point of plane 2).

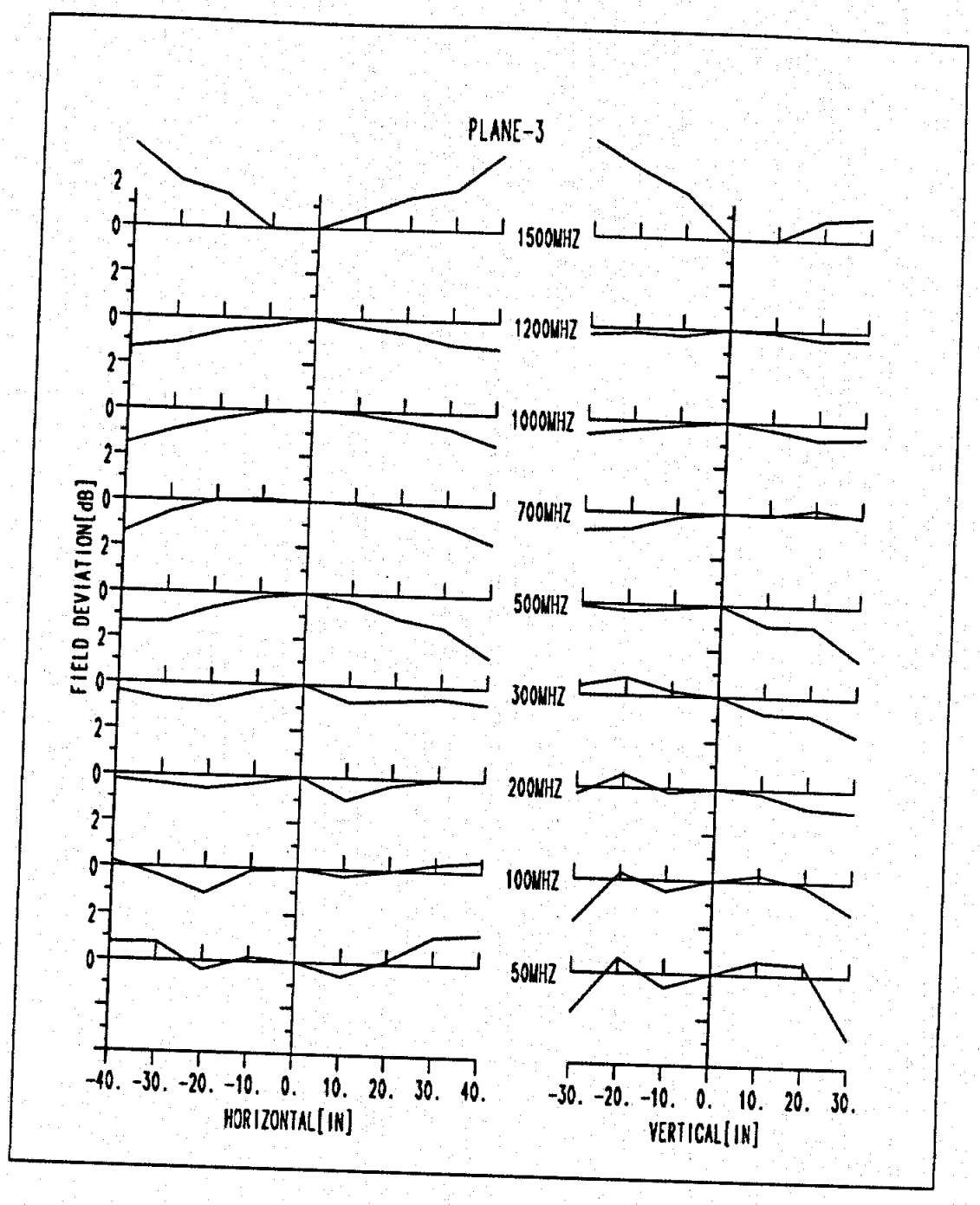

Figure 6.14: Measured field intensity in horizontal and vertical direction of plane 3 (normalized to the intensity at center point of plane 3).

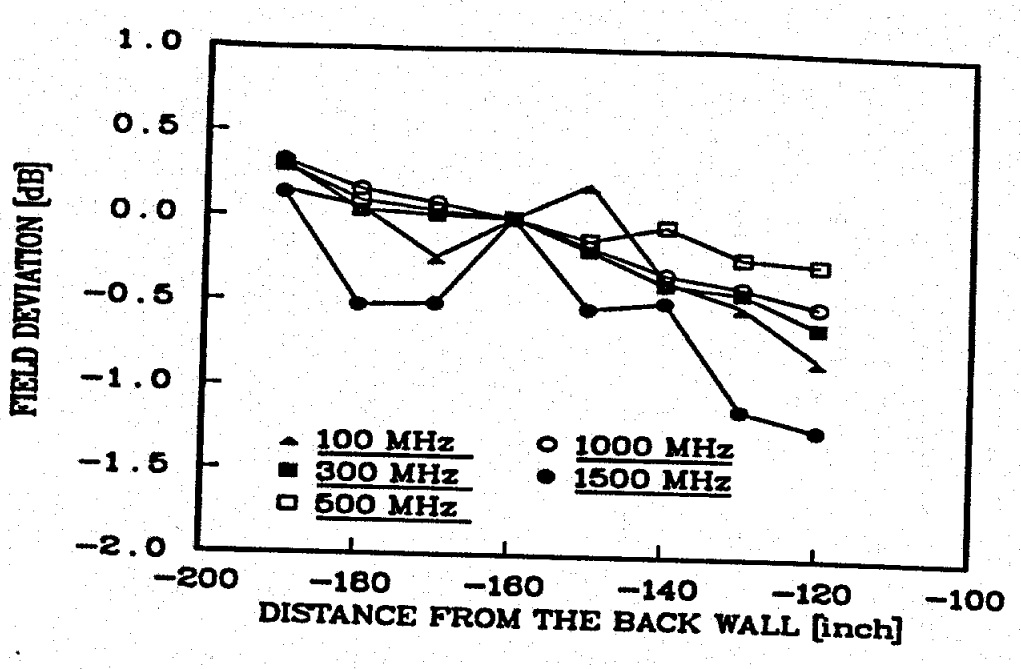

Figure 6.15: Measured field intensity in propagation direction (normalized with the intensity at center point).

function of distance from feed. Figures 6.12 through 6.15 reveal that the field is uniform within ± 1 dB in a 40 inch diameter sphere at the test area, the worst case being at 1500 MHz, the highest frequency measured.

6.3 Backscattering Measurements

In this section, the four-wire system is used to demonstrate its application for low frequency backscattering measurements. For the backscattering measurements, the same system as used for field mapping measurements was used (see Figure 6.8). A closed 21 inch high, 7 inch diameter aluminum cylinder was used as a scatterer. Measurements were made for various tilt angles as the tilted cylinder was rotated. Figure 6.16 shows the geometry of the cylinder showing the tilt and the rotating angles. The incident polarization was vertical. The measurements were performed for the tilt angles of 0, 30, 45, 60, and 90 degrees, separately. The cylinder was

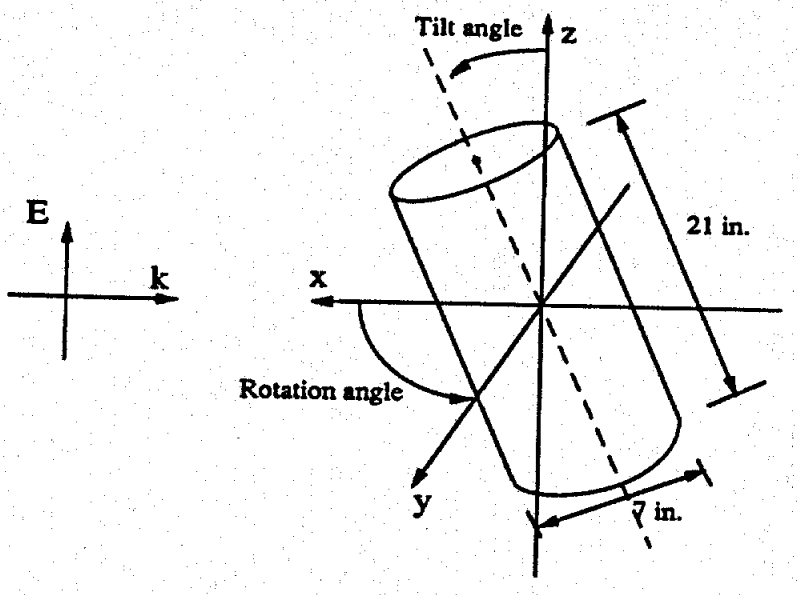

Figure 6.16: A geometry of cylinder used in backscattering measurement.

mounted on a styrofoam pedestal that was then mounted on an azimuthal rotator. The tilting of the cylinder was accomplished with styrofoam support wedges. For each tilt angle, the cylinder was rotated around the z axis and measured every five degrees. Calibration was performed with a 12 inch diameter sphere. The measured data were transferred to the HP9836 computer and processed according to the formula

$$\sigma_{cyl} = \frac{S_{11}^{cyl} - S_{11}^{back}}{S_{11}^{sph} - S_{11}^{back}} \sigma_{sph}^{mie} \tag{6.4}$$

where S_{11}^{cyl}, S_{11}^{back}, and S_{11}^{sph} are the measured S_{11} of the cylinder, the empty room and the sphere, respectively. The σ_{sph}^{mie} is the theoretical radar cross section of the sphere computed from the Mie series[99].

Figure 6.17 shows the radar cross section (RCS) of the cylinder, which is not tilted, as a function of rotating angle. In the figure, two frequencies are compared: 0.3 GHz with dotted line and 1 GHz solid line. The cylinder is rotated from -90 degrees to 90 degrees and measured at every five degrees. The RCS of the cylinder

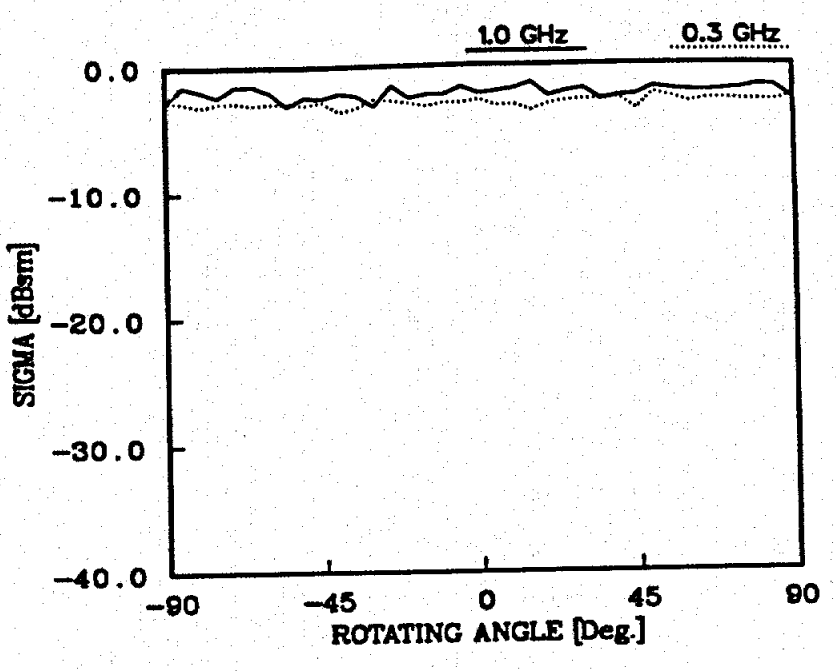

Figure 6.17: RCS of 0 degree tilted cylinder at 0.3 and 1 GHz.

is about -2.5 dBsm(dB square meters) at 1 GHz with $\pm$ 1 dB error and at 0.3 GHz, the RCS is about -3 dBsm with less error. Theoretically, the result should be a straight line. The error is attributed to the imperfect surface of the cylinder and different surface shapes of the sides of the styrofoam supports.

Figures 6.18 through 6.21 show the radar cross section of the cylinder with 30, 45, 60, and 90 degrees tilt angle, respectively, at both 0.3 and 1 GHz. The cylinder was rotated to 360 degrees and measured at every five degrees. When the cylinder is tilted to 30 degrees, the RCS at 1 GHz is very sensitive to the rotating angle while the RCS at 0.3 GHz is not. At 90 degrees tilt angle, the RCS of both frequencies have lobes but with different widths and levels. As a matter of fact, the five degree rotating step may be too large for the measurements, especially at 1 GHz. However, these are sample measurements to demonstrate the usefulness of the four-wire antenna

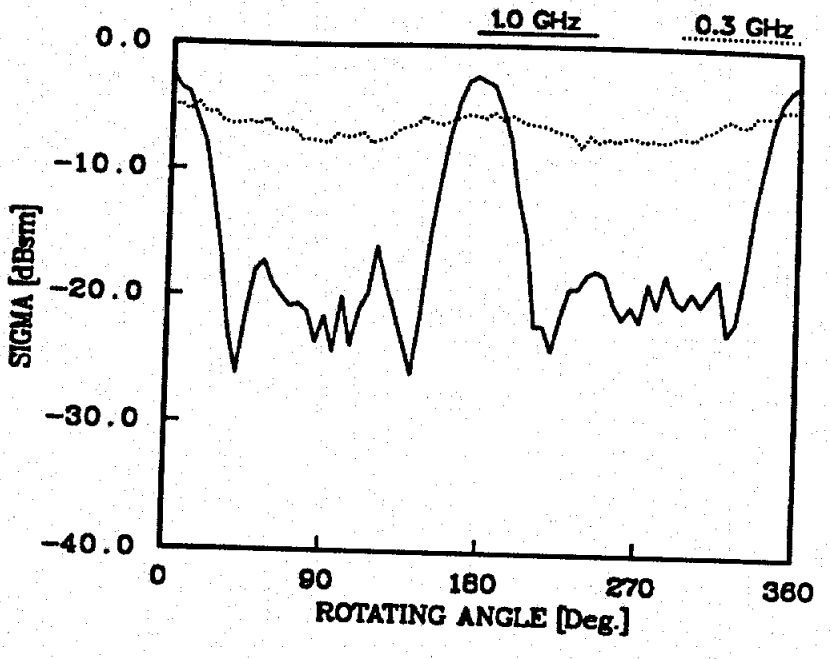

Figure 6.18: RCS of 30 degrees tilted cylinder at 0.3 and 1 GHz.

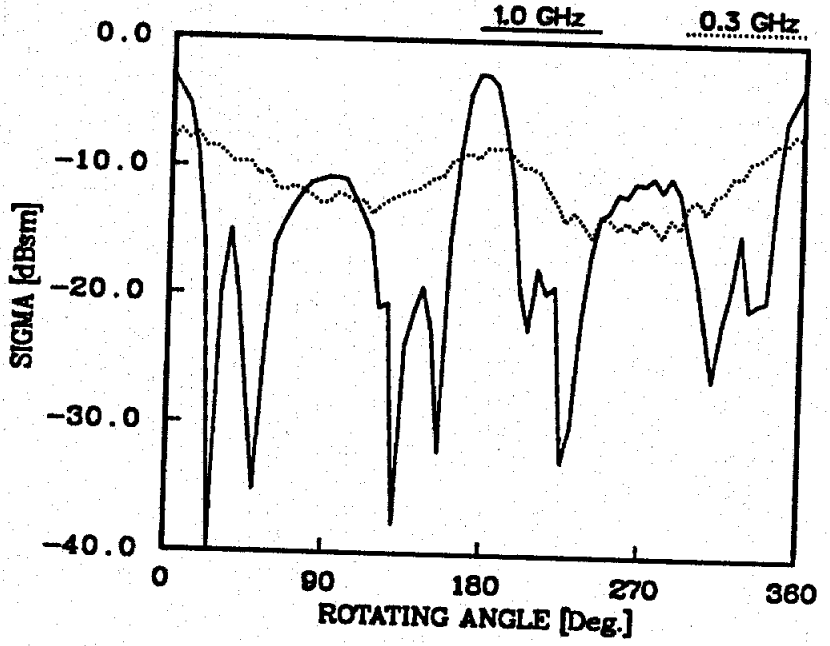

Figure 6.19: RCS of 45 degrees tilted cylinder at 0.3 and 1 GHz.

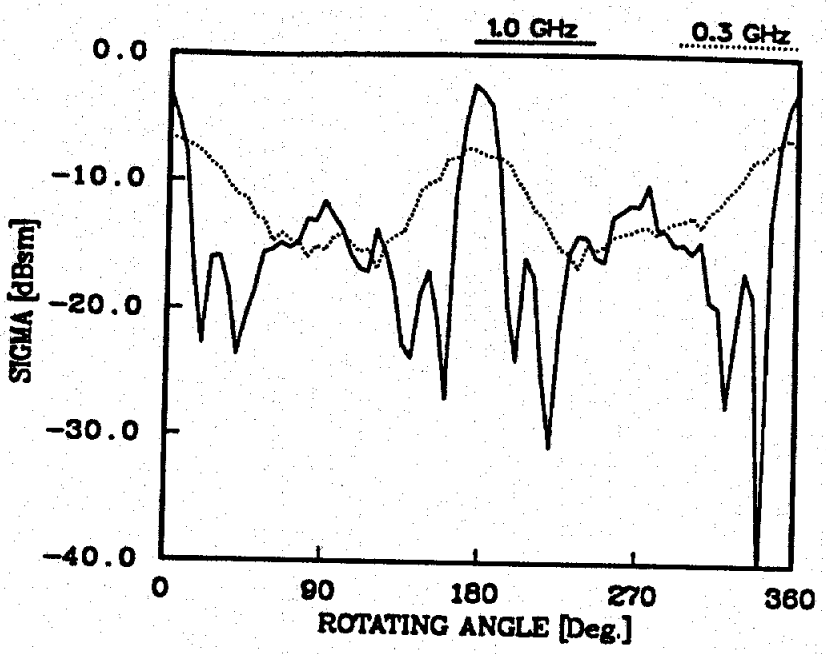

Figure 6.20: RCS of 60 degrees tilted cylinder at 0.3 and 1 GHz.

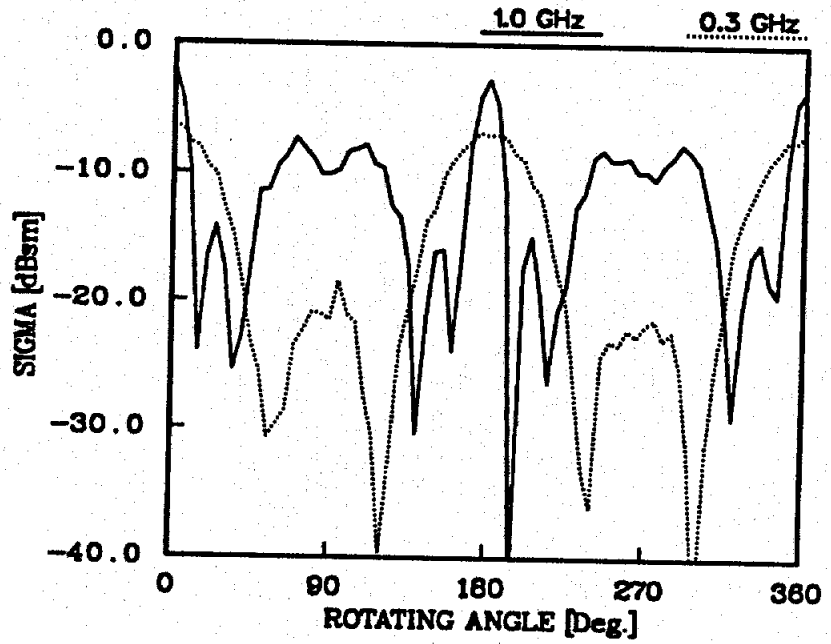

Figure 6.21: RCS of 90 degree tilted cylinder at 0.3 and 1 GHz.

6.4 Surface Currents Measurements

In this section, the surface current is measured again to demonstrate the application of the four-wire system in the EMC measurements. In these measurements, the broadband characteristic of the system is tested.

6.4.1 Initial Set up

Figure 6.22 shows the sketch of the tapered anechoic chamber with the four-wire system instrumented for surface current measurements (S_{21} measurements). In this set up, amplifiers are used to increase the signal to noise ratio. Some of the targets used have resonances at several hundred megahertz and some below one hundred megahertz. Figure 6.23 shows the block diagram of the feed and the instrumentation. The four-wire antenna is fed by $+V$ and $-V$ voltages to obtain vertical polarization. To obtain the differential mode, a broadband balun followed by a pair of matched amplifiers was used. These amplifiers are rated one watt each in the frequency range from 0.01 to 4.2 GHz. By using two amplifiers in the differential configuration, two watts of power are obtained. The amplitudes and phases of the differential configuration are carefully matched to within ± 1 dB tracking in amplitude and $\pm$ 10 degrees in phase in the frequency range by selecting proper attenuators and coaxial lines. Figure 6.24 shows the photograph of the balun and the two amplifiers at the feed. The bundles of strings are the ends of ropes and strings used to raise the wires to eliminated drooping.

In these measurements, a two millimeter diameter(D=2 mm) shielded loop sensor [100],[101] is used to measure the surface currents. Figure 6.25 shows the loop sensor that is constructed from 0.020 inch diameter semirigid cable. The voltage induced at the gap of the loop sensor is delivered to the preamplifier through a coaxial line that

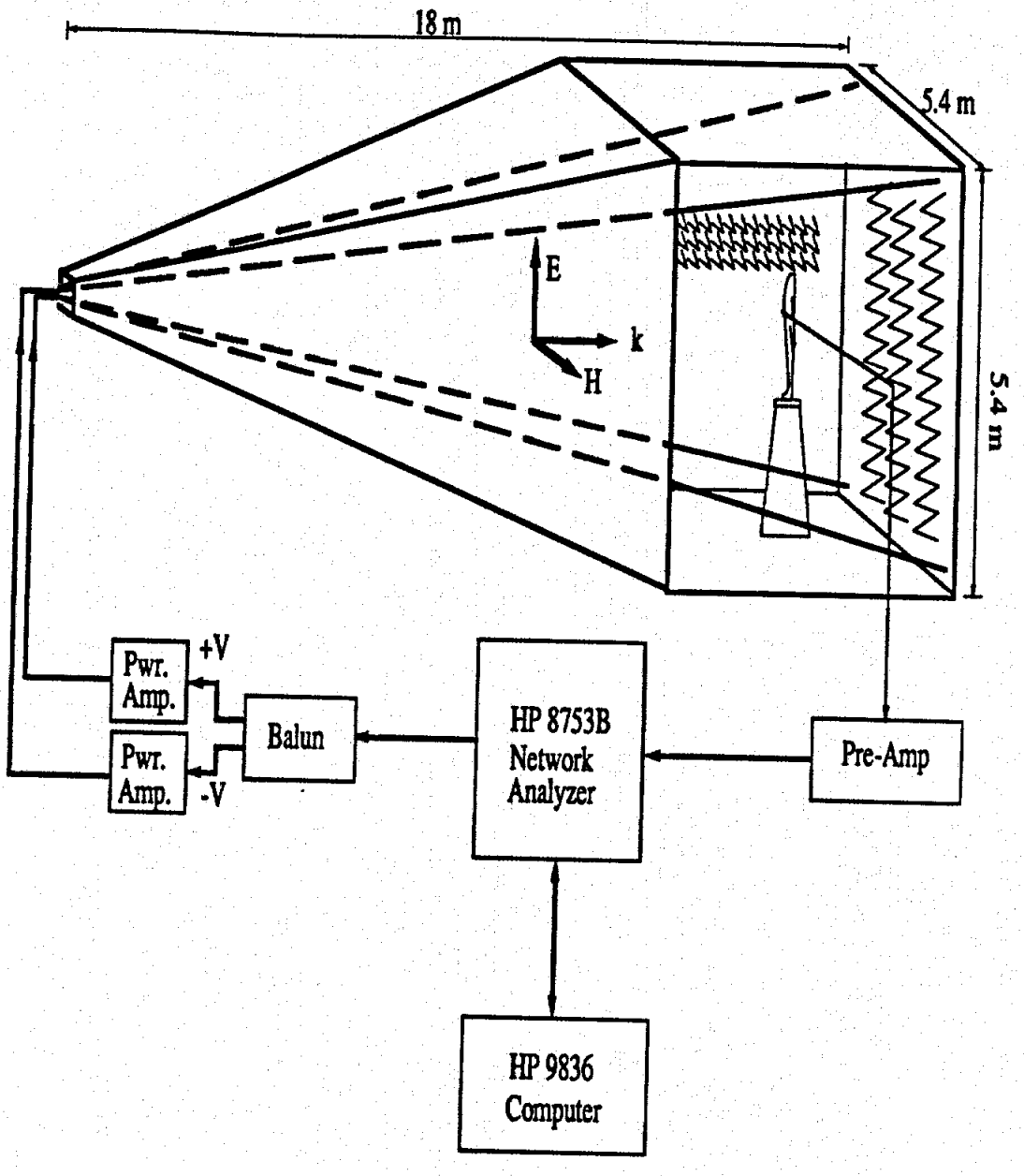

Figure 6.22: The tapered anechoic chamber with four-wire system with equipment set up for surface current measurements.

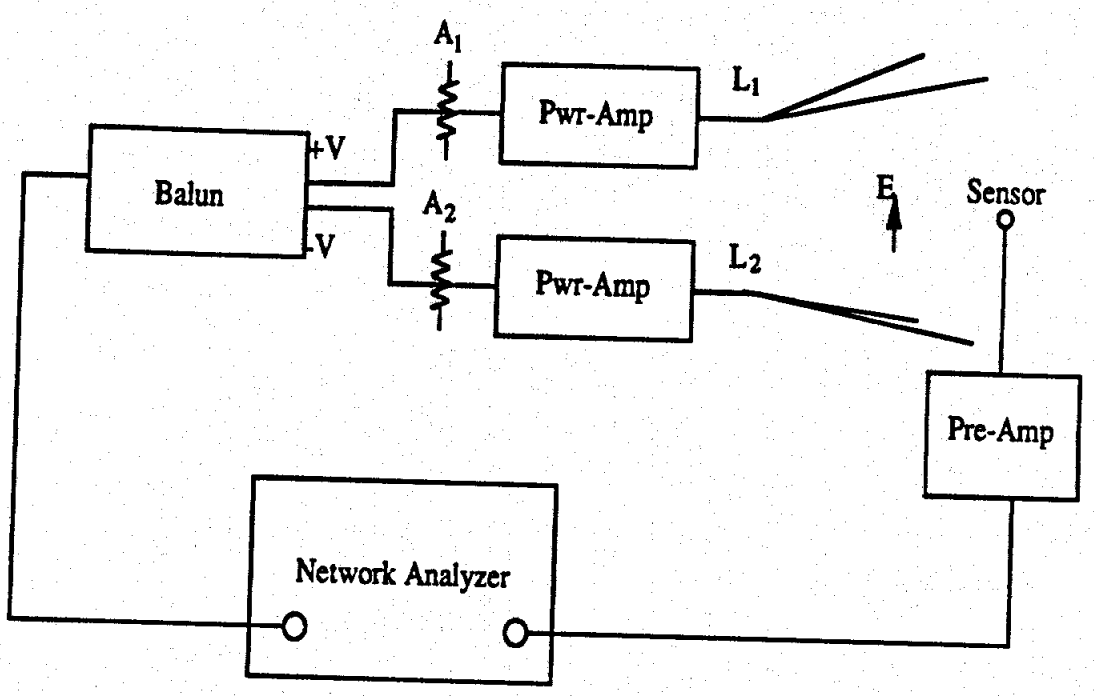

Network Analyzer	Hewlett Packard, 8753B
Pre-Amplifier	Minicircuits, ZHL-1042J
Pwr-Amplifier	Minicircuits, ZHL-42W, 2 ea
Balun	EG&G, DBM-4
L_1, L_2	Lines adjusted for phase match
A_1, A_2	Attenuators selected for amplitude match (norminal 3 dB)

Figure 6.23: Block diagram for the feed for a surface current measurement.

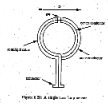

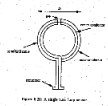

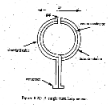

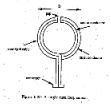

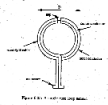

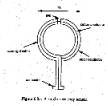

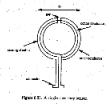

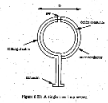

is supported horizontally in the chamber. With the network analyzer set to sweep from 0.3 MHz to 5000 MHz, the time domain response of an empty chamber is shown in Figure 6.26. The first peak, denoted by "A", is the direct signal. Peak "B" appears due to a ray bounced by the chamber ceiling, and peak "C" is due to the reflection at the rear wall. The antenna wires in this case were not terminated, but left in an open circuit. We note that these peaks are over 20 dB below the direct signal and can easily be gated out as was done in the field measurements (Section 6.2.2).

6.4.2 Measurements

For the surface current measurements, we performed measurement on two kinds of objects: spheres and B-1B aircraft models. A sphere is the most obvious model to start with to check the performance of the facility. For a sphere, the fields are well known and easily computable from the Mie series[99]. Also, the sphere is commonly used as the calibration target for most measurements. Aircraft models were selected for the targets of the test measurements. Similar aircraft models had been used in [100] and [101].

Figures 6.27 and 6.28 show the surface currents of the 7.96 centimeter and 15.24 centimeter diameter spheres, respectively. In the figures, the solid lines represent the magnitudes of the current densities that are normalized to the incident magnetic fields and the dotted lines show the phases. The theoretical curves (Mie series) are shown in (a) and the measured curves in (b) of each figure for comparison. For the measured curves, the 7.96 centimeter diameter sphere is used for calibration. In Figure 6.27, the measured data show the repeatability and the accuracy of the measurement since the measurement is calibrated with the same model at the same location. The measured data contain significant noise in the frequency ranges below

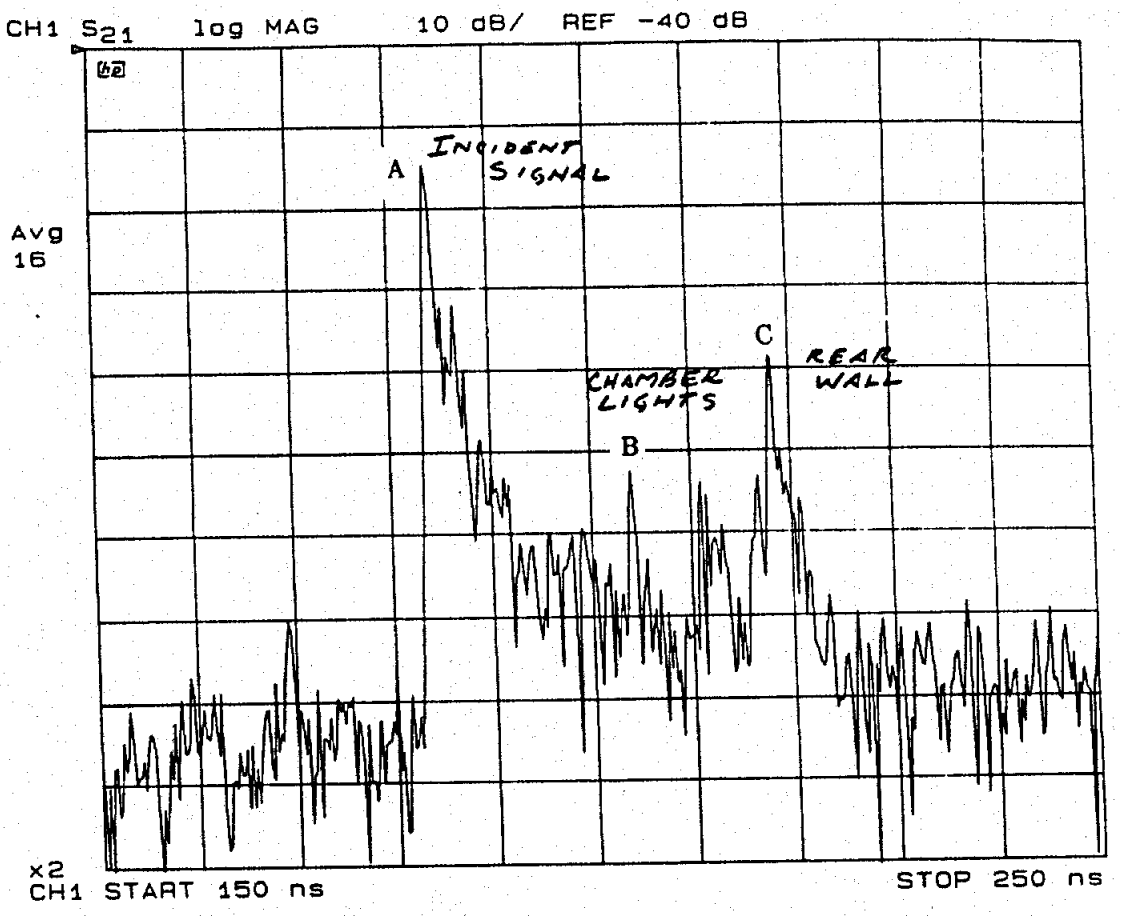

Figure 6.26: Time domain response of 0.3 MHz to 5 GHz sweep signal measured with small magnetic loop in test region.

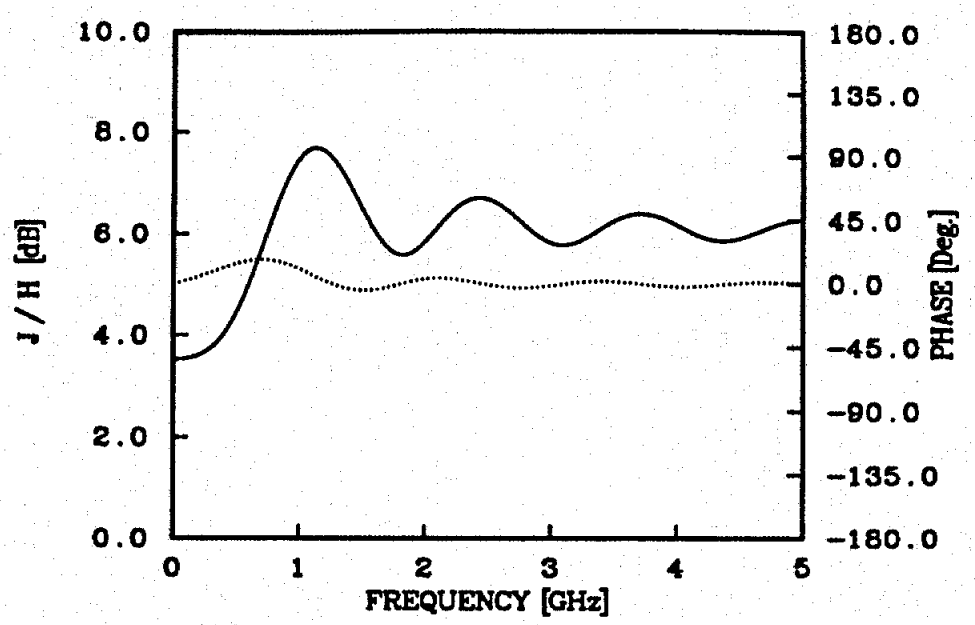

(a) Theoretical current.

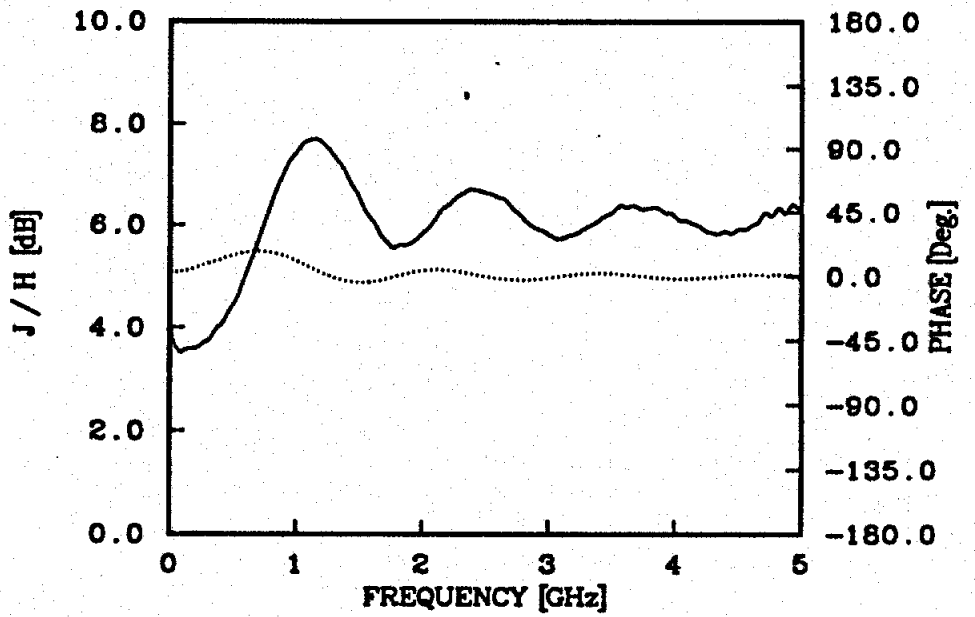

(b) Measured current.

Figure 6.27: Theoretical and measured current on the 7.96 cm diameter sphere. Solid line shows magnitude and dotted line phase.

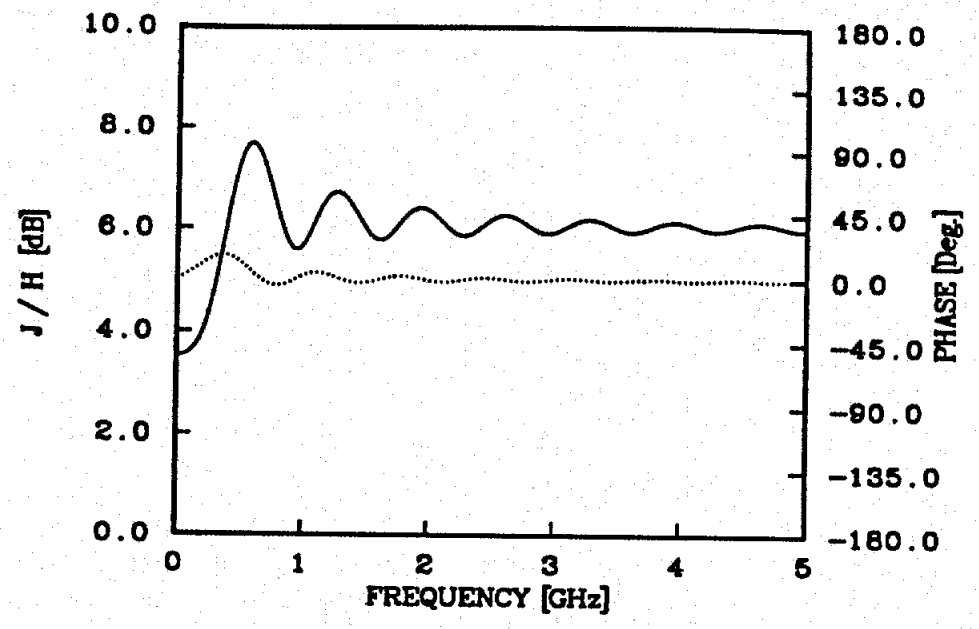

(a) Theoretical current.

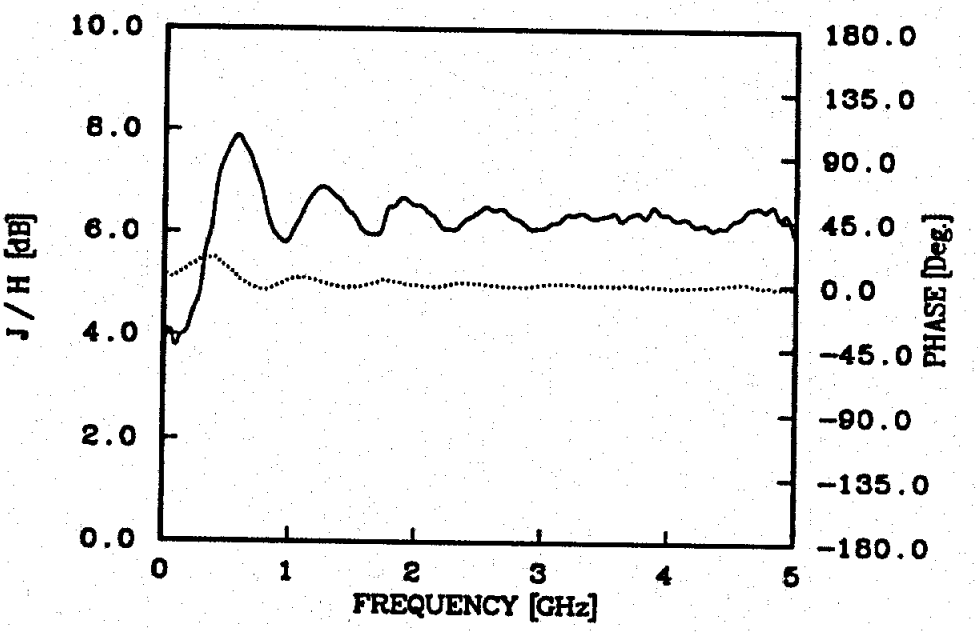

(b) Measured current.

Figure 6.28: Theoretical and measured current on the 15.24 cm diameter sphere. Solid line shows magnitude and dotted line phase.

50 MHz and above 4500 MHz. Figure 6.28 demonstrates the performance of the four-wire facility for the use of the surface current measurement. Comparing to the theoretical curve (upper graph), the measurement is accurate to ± 0.2 dB in amplitude and to five degrees in phase from 0.1 to 4.5 GHz.

In these measurements, the gate width, gate shape, and the bandwidth (or frequency range) of the network analyzer affect the final results. For example, Figure 6.29 shows a measurement on the 15.24 cm diameter sphere measured from 0.3 MHz to 1 GHz and gated with the same gate width as in Figure 6.28. The results are slightly different, which is not necessarily unexpected.

For the B-1B aircraft measurements, we acquired three models. Those models were 1/48 scale B-1B (Revell No.4900), 1/72 scale B-1B (Monogram No.5606), and 1/72 scale Boeing 707 Intercontinental (Heller No.80305). These aircraft were prepared in the usual way including spraying with conductive (silver) paint. The measurement point was selected on top of the fuselage at 30.3 percent of the fuselage length when measured from the tip of the radome. In all cases, the illumination was top incidence, electric vector parallel to the fuselage, and the measured field component was the axial surface current density normalized to the incident magnetic field. Figure 6.30(a) shows the the B-1B models mounted on the styrofoam with the loop sensor.

Figures 6.31 and 6.32 show the measurements of the current on the 1/48 scale and 1/72 scale models, respectively. In these figures, the upper graphs are for the "wings-forward" and the lower for the "wings-swept" configurations. Note that the frequency scales are not converted to full scale frequencies in order to help access the frequency range performance of the four-wire antenna facility. The amplitude curves in these figures show the classical half-wave resonance of 18 to 20 dB above

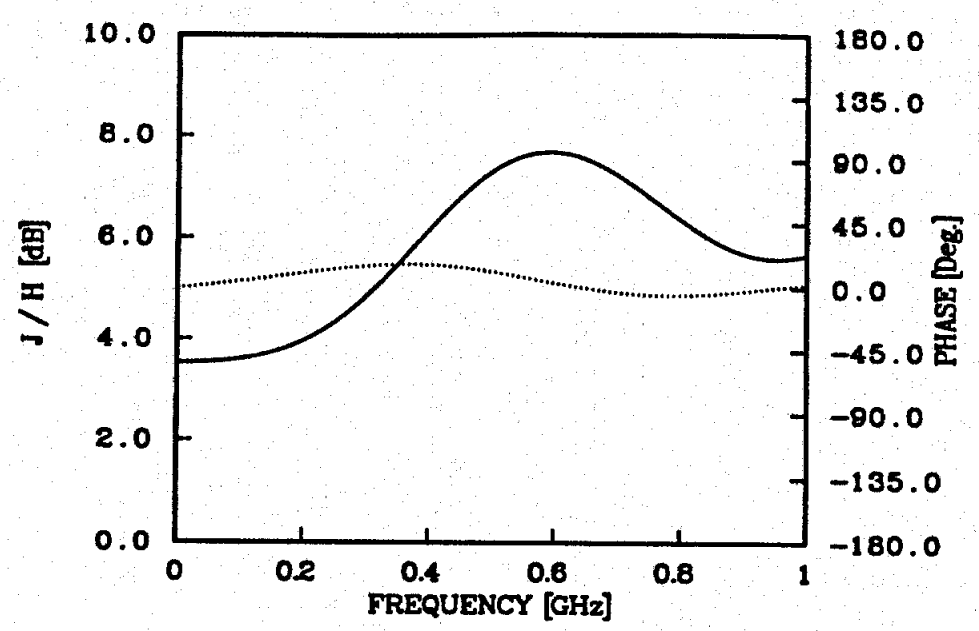

(a) Theoretical current.

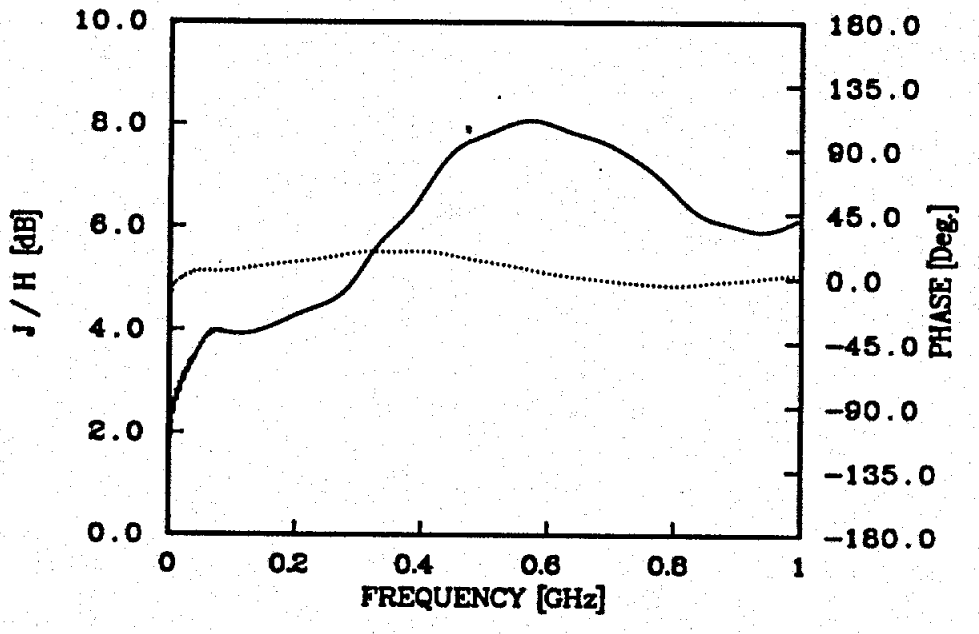

(b) Measured current.

Figure 6.29: Theoretical and measured current on the 15.24 cm diameter sphere; 0.3 MHz to 1 GHz frequency range. Solid line shows magnitude and dotted line phase.

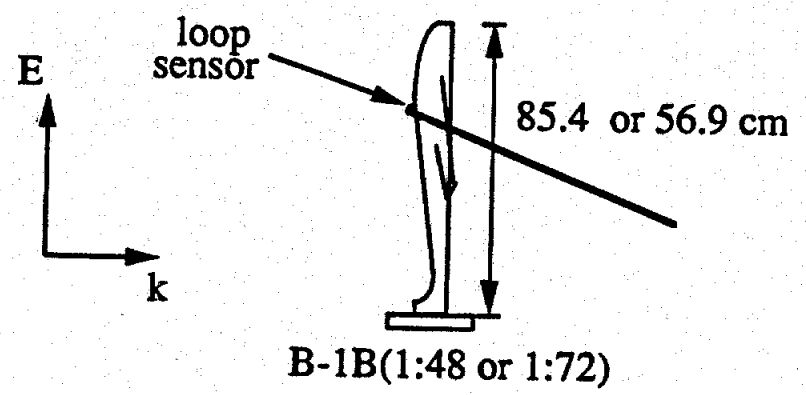

(a) B-1B flying mode.

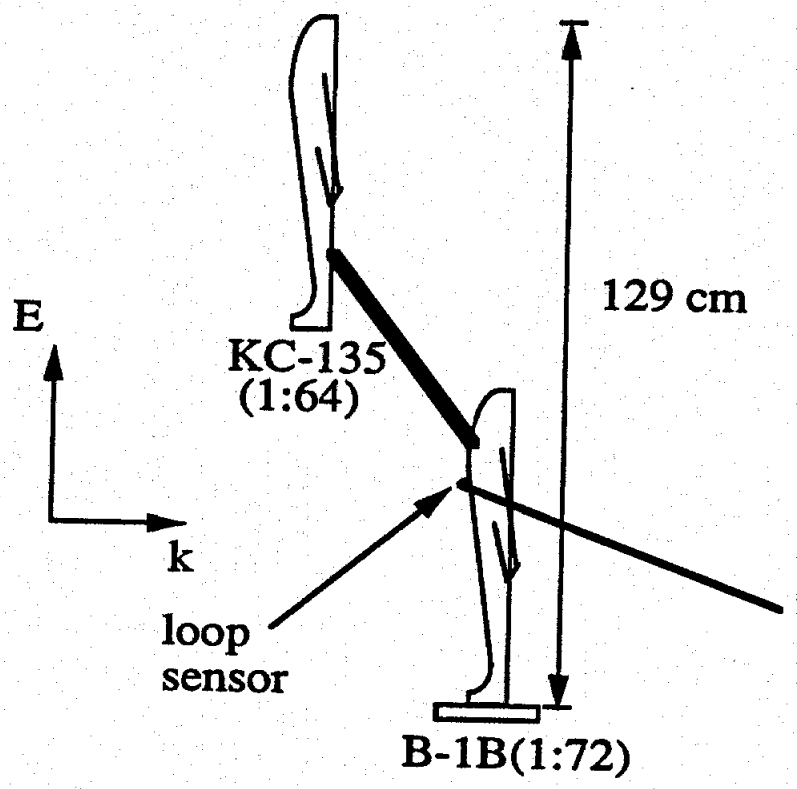

(b) B-1B refueling mode.

Figure 6.30: B-1B models. A loop sensor is located at 30.3 percentile fuselage position from the radome of the B-1B.

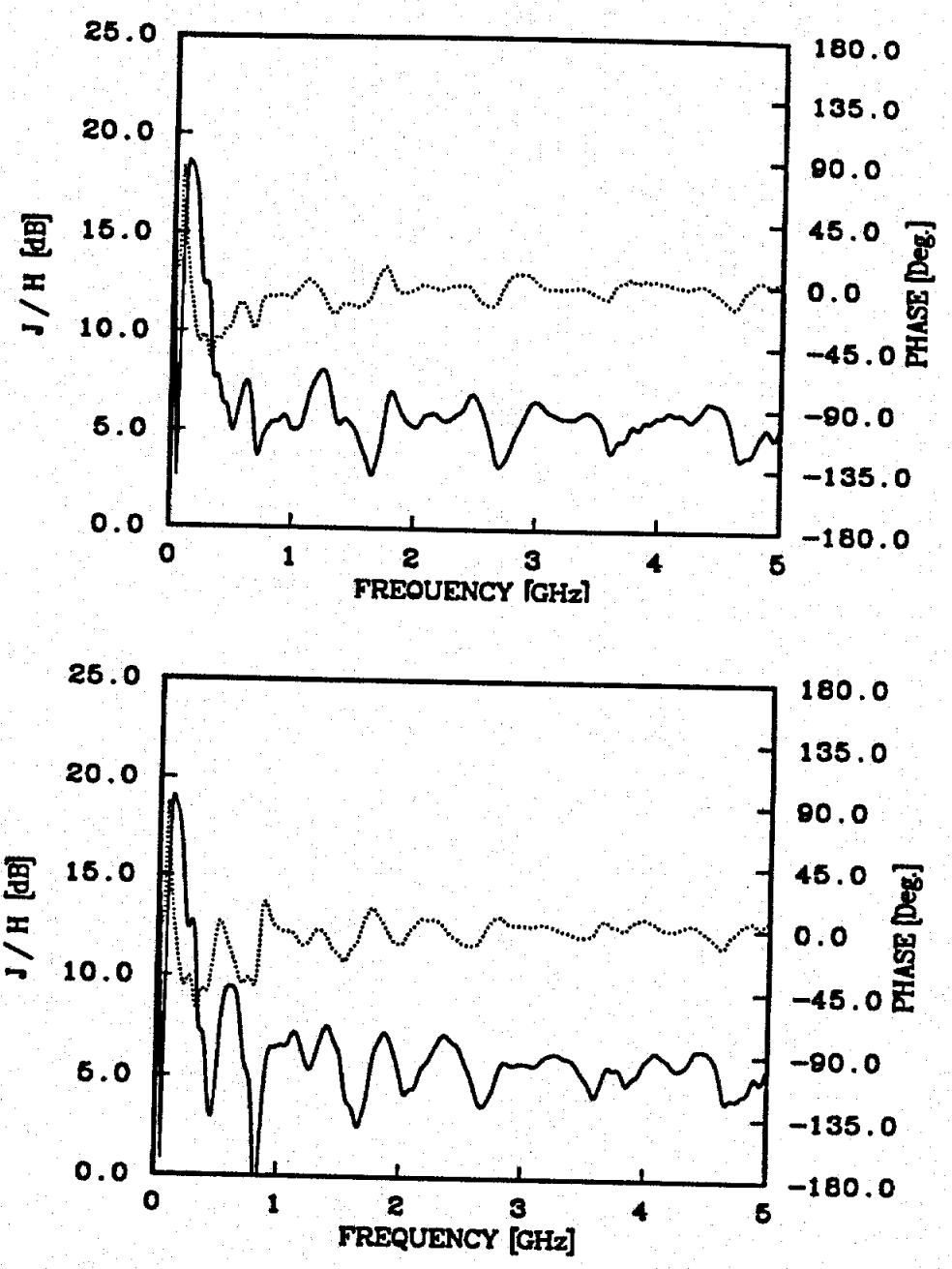

Figure 6.31: Surface current on 1/48 scale model of B-1B at 30.3 percentile fuselage position; wings forward (top) and wings swept (bottom). Solid line shows magnitude and dotted line phase.

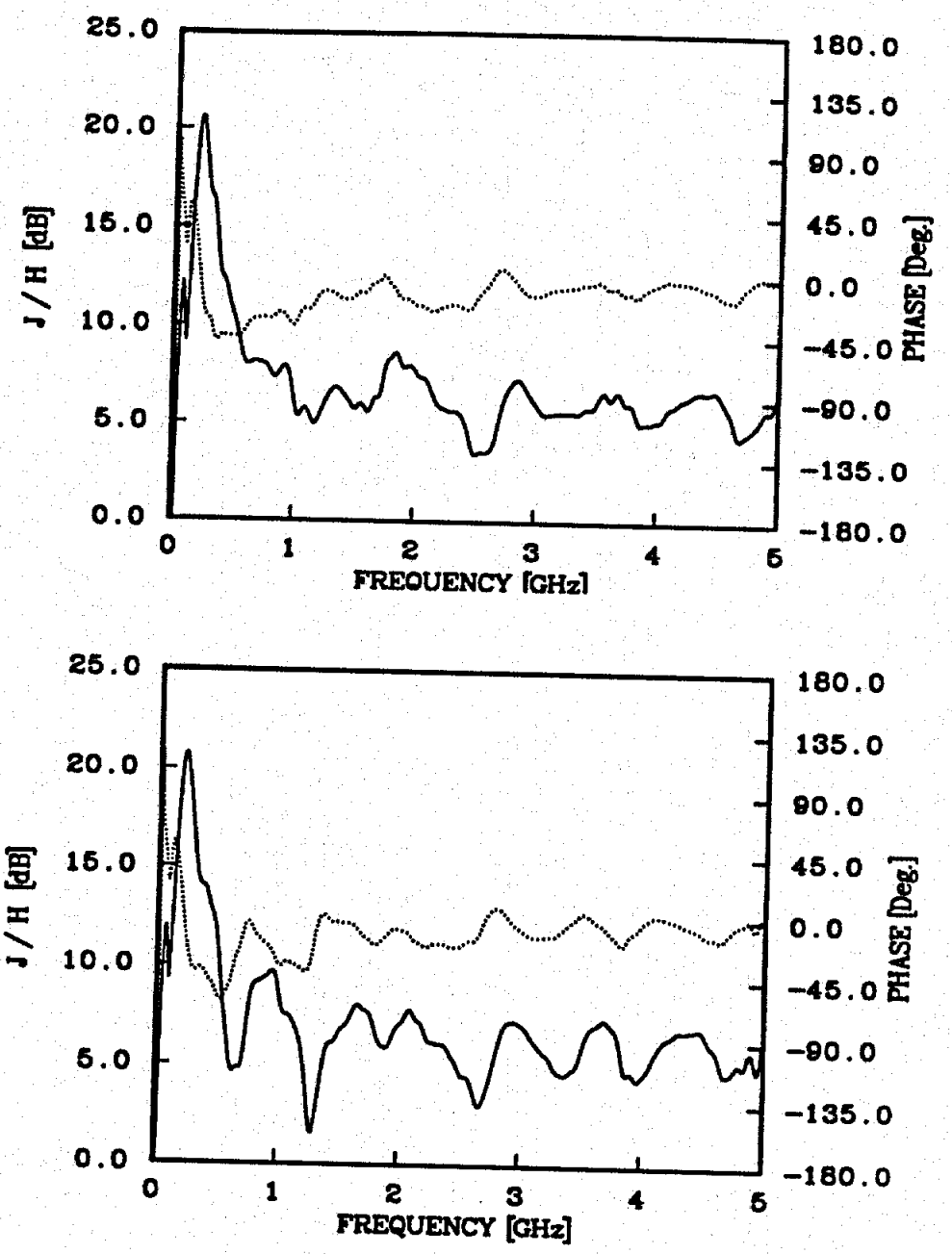

Figure 6.32: Surface current on 1/72 scale model of B-1B at 30.3 percentile fuselage position; wings forward (top) and wings swept (bottom). Solid line shows magnitude and dotted line phase.

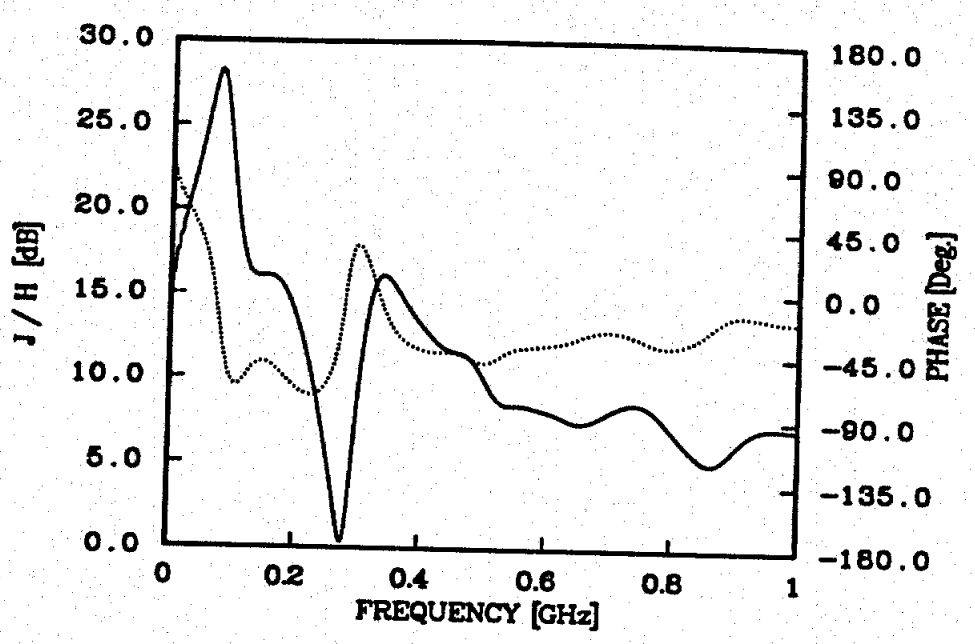

Figure 6.33: Surface current on top of 1/72 scale model of B-1B at 30.3 fuselage percentile position for the in-flight refueling mode. The tanker is the KC-135 with same scale. Top incidence, axial fuselage current. Solid line shows magnitude and dotted line phase.

the incident field. The amplitudes vary around 6 dB, which is the high frequency optics approximation.

Figure 6.30(b) shows the 1/72 scale B-1B model for the in-flight refueling mode configuration. The tanker is the KC-135 at 1/72 scale that is a modified version of the Boeing 707 Intercontinental. The measurement point is chosen at the 30.3 percentile fuselage position when measured from the tip of the radome. The measured surface currents are shown in Figure 6.33. To show more detail in the resonance behavior, the measurement was performed over a 0.3 MHz to 1 GHz range. As this figure shows, the main resonant peak is at about 80 MHz, corresponding to 1.1 MHz full scale frequency. It is also observed that the peak here is about 8 dB higher than that of the individual cases shown in Figures 6.31 and 6.32.

CHAPTER VII

CONCLUSIONS AND FUTURE WORK

In this thesis, a four-wire antenna was introduced for use in EMC measurements. The four-wire antenna consists of two V-antennas that also form V geometry with each other. The antenna was designed to produce a uniform field in the test area over a wide frequency range. Since an anechoic chamber is a widely used facility in EMC measurements, the antenna was installed and tested in the anechoic chamber.

The antenna was first analyzed in free space using the Numerical Electromagnetic Code(NEC). In order to remove the reflections at the end of the wires, an appropriate loading resistance distribution was determined. The obtained resistance distribution, which has the form of a square function, is effective over a broad frequency range from 50 MHz to 1000 MHZ. The free space analysis showed that the antenna produced a $\pm$ 1 dB uniform field in a two meter diameter spherical test area with the symmetric arrangement of the wires. The computed input impedances and field distributions indicate that the antenna is usable in the frequency range from 50 MHz to 1000 MHz and possibly to 5000 MHz since the computations were limited to below 1000 MHz.

Since the antenna was installed in the anechoic chamber, the effects of absorbers were also studied. When frequencies are high, typically above 500 MHz, the absorbers show good performance and the antenna can be considered as being in free

space. However, below 500 MHz, and especially below frequencies where the absorbers are ineffective, the antenna performance will be affected by the chamber. To consider the effects of the chamber walls, which are covered by the absorbers, modified volume-surface integral equations(modified VSIEs) were developed. By applying the modified VSIEs, the chamber walls with wedge type absorbers were analyzed. From the results of the analysis, equivalent lossy layers were obtained. The equivalent layers have compatible reflectivities with those of wedge absorbers. With the equivalent layers, the anechoic chamber with the four-wire antenna was analyzed using the finite element technique. In the finite element analysis, the fields were confirmed to be uniform.

The four-wire antenna was constructed and installed in the anechoic chamber at the University of Michigan Radiation Laboratory. The field distributions were measured and are within $\pm$ 1 dB field deviation in a two meter diameter spherical test area. The input impedances of the antenna were also measured in the frequency range from 3 MHz to 6000 MHz. The advantage of the four-wire antenna is the extremely wide bandwidth capability. Whereas typically horn antennas have a 2:1 bandwidth and ridge-horns a 10:1, or even 20:1, bandwidth, the four-wire structure can easily achieve 100:1 bandwidth such as 50 MHz to 5000 MHz.

To show the potential of the four-wire system for EMI/EMC applications, sample measurements were performed and presented. These include induced surface field measurements on spheres and model aircraft and backscattering measurements from a cylinder. In surface field measurements a $\pm$ 0.2 dB measurement accuracy is demonstrated on the measurements made on spheres. The results of backscattering measurements are not as impressive ($\pm$ 1 dB), but it must be emphasized that such measurements can be made at frequencies below 100 MHz, a frequency region that

otherwise could not be measured in an anechoic chamber.

There are two topics that need further study to bring the four-wire designs closer to practical implementation. One is the development of a practical and effective matching of the wire at the back wall and the other is a study of the interaction between the device under test and the antenna wires. In the case of resistive loading, some theoretical studies were presented in section 2.2, but the such design would be impractical to implement. In hindsight, the appropriate loading would be a lumped resistor located at the end of each wire and embedded in an absorbing material.

Finally, because of the presence of antenna wires along the walls of the chamber, questions still exist concerning the level of interaction between the model and the wires. This interaction could be studied in two ways (or in conjunction): (1) by theoretically/numerically analyzing the entire chamber with the test model present, and/or (2) by making careful backscattering or surface field measurements on objects for which the results are known and then analyzing the data.

BIBLIOGRAPHY

BIBLIOGRAPHY

[1] P. L. Rustan," Description of an aircraft lightening and simulated nuclear electromagnetic pulse (NEMP) threat based on experimental data," IEEE Trans. Electromagn. Compat., vol. EMC-29, pp. 49-63, Feb., 1987.

[2] C. E. Baum, F. L. Breen and G. D. Pitts, " The measurements of lightening environmental parameters related to interaction with electronic systems," IEEE Trans. Electromagn. Compat., vol. EMC-24, pp. 123-136, May 1982.

[3] M. A. Uman and P. E. Krider, " A review of natural lightening: Experimental data and modeling," IEEE Trans. Electromagn. Compat. vol. EMC-24, pp. 79-112, May 1982.

[4] N. C. Gerson and W. H. Gossard, "Sweepers, communication and solar activity," IEEE Trans. Electromagn. Compat., vol. EMC-5, pp. 86-97, Mar. 1963.

[5] A. U. H. Sheikh and J. D. Parsons, "Statistics of electromagnetic noise due to high-voltage power lines," IEEE Trans. Electromagn. Compat., vol. EMC-23, pp. 412-419, Nov. 1981.

[6] T. Nakai and Z. Kawasaki, "Automotive noise from a motorway:Part I, Measurement," IEEE Trans. Electromagn. Compat. vol. EMC-26 pp. 169-174, Nov. 1984.

[7] R. Shepherd, "Measurements of amplitude probability distributions and power of automobile ignition noise at high frequency," IEEE Trans. Veh. Technol., vol. VT-23, pp. 72-83, Aug. 1974.

[8] T. Nakai and Z. I. Kawasaki, "APD's and CRD's for noise from bullet trains in Japan," in Proc. IEEE Int. Symp. EMC, Tokyo, Japan, pp. 250-255, Oct. 1984.

[9] H. A. Turner and G. H. Hagn, "Measurement of radiation from selected TD-2 microwave relay stations," IEEE Trans. Electromagn. Compat., vol. EMC-7, pp. 104-111, June 1965.

[10] M. Kanda, " Time and amplitude statistics for electromagnetic noise in mines." IEEE Trans. Electromagn. Compat. vol. EMC-17, pp122-129, Aug. 1975.

[11] H. H. Hoffman and D. C. Cox, " Attenuation of 900 MHz radio waves propagating into a metal building," IEEE Trans. Antennas Propagat., vol AP-30, pp 808-811, July 1982.

[12] D. C. Cox, R. R. Murray, and A. W. Norris, " Measurement of 800 MHz radio transmission into buildings with metallic walls," Bell Syst. Tech. J., vol. 62, no. 9, pp. 2695-2717, Nov. 1984.

[13] S. G. Lutz and D. E. Miller, " Interference problems of co-channel communication satellite system," IEEE Trans. Electromagn. Compat., vol. EMC-4, pp. 49-57, Oct. 1962.

[14] M. Haskard, M. Miller, A. Johnson, and P. Marconi, " Radio noise measurements in an urban environment," J. Elec. Electron Eng. Australia, vol. 2, no. 2, pp. 94-102, June 1982.

[15] J. Parsons and A. Sheikh, " Statistical characterization of VHF man-made radio noise," Radio Elec. Eng., vol. 53, no. 3, pp 99-106, Mar. 1983.

[16] P. L. Rustan, "The lightning threat to aerospace vehicles," AIAA J. Aircraft, vol. 23, no. 1, pp. 62-67, Jan. 1986.

[17] J. P. Muccioli and S. Awad, " The electromagnetic environment of an automobile electronic system," IEEE Trans. Electromagn. Compat., vol. EMC-29, pp. 245-251, Aug. 1987.

[18] R. E. Richardson, V. G. Puglielli, and R. A. Amadori, " Microwave interference effect in bipolar transistors," IEEE Trans. Electromagn. Compat., vol. EMC-17, pp 216-219, Nov. 1975.

[19] J. J. Whalen, J. G. Tront, C. E. Larson, and J. M. Roe, " Computer aided analysis of RFI effects in digital integrated circuitts," IEEE Trans. EMC, vol. EMC-21, pp. 291-297, Nov. 1979.

[20] J. G. Tront, " Predicting URF upset of MOSFET digital IC's," IEEE Trans. Electromagn. Compat., vol EMC-27, pp. 64-69, May 1985.

[21] S. Gutsche, " A spectrum prediction technique for AM puse of arbitrary shape," IEEE Trans. Electromagn. Compat., vol. EMC-13, pp.64-69, May, 1971.

[22] B. Audone, " Graphical harmonic analysis," IEEE Trans. Electromagn. Compat., vol. EMC-15, pp.72-74, May 1973.

[23] C. Y. Wu and D. K. Cheng, " A method for symmetrizing generalized impedance matrices," IEEE Trans. Electromagn. Compat., vol. EMC-19, pp. 81 -88, May 1977.

[24] T. E. Baldwin, Jr., and G. T. Capraro, " Intrasystem Electromagnetic Compatibility Program (IEMCAP)," IEEE Trans. Electromagn. Compat., vol. EMC-22, pp. 224-228, Nov. 1980.

[25] J. W. Ashforth, " A broadband, multichannel transient monitoring system for improved interference control," IEEE Trans. Electromagn. Compat., vol. EMC-7, pp. 55-63, May 1965.

[26] M. Kanda and F. X. Ries, " A broad-band isotropic real-time electric-field sensor (BIRES) using resistively loaded dipoles," IEEE Trans. Electromagn. Compat., vol. EMC-23, pp.122-132, Aug. 1981.

[27] C. E. Baum, "Winding topology for transformers," Air Force Weapons Lab. Measurement Notes, Note 31, Kirtland AFB, NM, Oct. 1986.

[28] W. K. Roberts, " A new wideband balun," Proc. IRE, pp. 1028-1031, Dec. 1957.

[29] V. H. Rumsey, Frequency Independent Antennas. New York: Academic Press, 1966.

[30] C. E. Smith, Log Periodic Antenna Design Handbook. Cleveland, OH: Smith Electronics, 1966.

[31] H. Jasik, Antenna Engineering Handbook. New York: McGraw-Hill, 1961.

[32] M. Kanda, " The effects of resistive loading of "TEM" horns," IEEE Trans. Electromagn. Compat., vol. EMC-24, pp. 245-255, May, 1982.

[33] Constantine A. Balanis, Antenna Theory, New York: Harper & Row Publishers, Inc., 1982.

[34] H. F. Harmuth, " Antennas for nonsinusoidal waves. I. Radiators," IEEE Trans. Electromagn. Compat., vol. EMC-25, pp. 13-24, Feb. 1983.

[35] C. W. Gillard and R. E. Franks, " Frequency independent antennas - several new and undeveloped ideas," The Microwave Journal, pp. 67-72, Feb. 1961.

[36] K. L. Walton and V. C. Sundberg, " Broadband rigid horn design," the microwave journal, pp. 96-101, Mar. 1964.

[37] M. Kanda and L. D. Driver, " An isotropic electric-field probe with tapered resistive dipoles for braod-band use, 100 KHz to 18 GHz," IEEE Trans. Microwave Theory Tech., vol. MTT-35, Feb. 1987.

[38] D. A. Weston, Electromagnetic Compatibility: principles and application, Marcel Decker, Inc., 1991.

[39] C. E. Baum, "Impedances and field distributions for symetrical two wire and four wire transmission line simulators," Sensor and Simulation Note 27, October 1966.

[40] J. M. Jarem, "Electromagnetic field analysis of a four-wire anechoic chamber," IEEE Trans. Antennas and Propagat., vol. 38, pp. 1835-1842, Nov. 1990.

[41] J. M. Jarem, "TEM wave propagation in a parallel, four-wire anechoic chamber enclosure," Proc. 21st South Eastern Symp. Syst. Theory, Mar. 26-28, pp. 476-480, 1989.

[42] E. N. Clouston, P. A. Langsford, and S. Evans, " Measurement of anechoic chamber reflections by time-domain technique," Proc. IEE, vol. 135, Pt. H, no. 2, Apr. 1988.

[43] B. T. Dewitt and W. D. Burnside, " Electromagnetic scattering by pyramidal and wedge absorber," IEEE Trans Antennas and Propagat., vol. 36, pp. 971-984, July 1988.

[44] G. J. Burke and A. J. Pogio, "Numerical Electromagnetics Code," Naval Ocean Systems Center, 1981.

[45] H. E. Foster, Transient Radiation from Resistively Loaded Transmission Lines and Thin Biconical Antennas, Ph.D. Dissertation. Univ. of Michigan, 1973.

[46] B. T. Dewitt and W. D. Burnside, " Electromagnetic scattering by pyramidal and wedge absorber," IEEE Trans. Antennas Propagat., vol. AP-36, pp. 971-984, July 1988.

[47] J. L. Yen, " Multiple scattering and wave propagation in periodic structures," IRE Trans. Antennas Propagat., vol. AP-10, pp. 769-775, Nov. 1962.

[48] S. L. Chuang, J. A. Kong, " Wave scattering and guidance by dielectric waveguides with periodic surfaces," J. Opt. Soc. Am., vol. 73, pp. 669-679, 1983.

[49] K. Sarabandi, " Simulation of a periodic dielectric corrugation with an equivalent anisotropic layer," Int. J. of Infrared and Millimeter Waves, vol. 11, pp. 1303-1321, Nov. 1990.

[50] K. Uchida, T. Noda, T. Matsunaga, " Spectral domain analysis of electromagnetic wave scattering by an infinite plane metallic grating," IEEE Trans. on Antennas Propagat., vol. AP-35, pp. 46-52, Jan. 1987.

[51] R. C. Hall, R. Mittra, and K. M. Mitzner, " Scattering from finite thickness resistive strip gratings," IEEE Trans. Antennas Propagat., vol. AP-36, pp. 504-510, Apr. 1988.

[52] T. C. Tong, Scattering of electromganetic waves by a periodic surface with arbitrary profile, Ph.D. Dissertation. Univ. of Michigan, 1972.

[53] J. M. Jin, V. V. Liepa, and C. T. Tai, " A volume-surface integral equation for electromagnetic scattering by inhomogeneous cylinders," J. of EM Waves and Appl., vol. 2, pp. 573-588, 1988.

[54] C. C. Su, "A surface integral equations method for homogeneous optical fibers and coupled image lLines of arbitrary cross sections," IEEE Trans. Microwave Theory Tech., vol. MTT-33, pp. 1114-1119, Nov. 1985.

[55] J.M. Jin, V. V. Liepa, "Simple moment method program for computing scattering from complex cylindrical obstacles," Proc. IEE, vol. 136, Pt. H, No. 4, Aug. 1989.

[56] C. Cheon and V. Liepa, "Dielectric constant measurement of microwave absorber for four-wire system," Radiation Lab. Report 027631-1-F, EECS, Univ. of Michigan, July 1990.

[57] Hewlett Packard, "Measuring Dielectric Constant with the HP 8510 Network Analyzer," Production Note No. 8510-3., 1985.

[58] Johnson, W. C.,"Transmission Lines and Networks," New York: McGraw-Hill Book Co., 1950.

[59] R. F. Harrington, Time-Harmonic Electromagnetic Fields, New York: McGraw-Hill Book Company, pp.373, 1961.

[60] Ulaby, F. T., T. Bengal, J. East, M.C. Dobson, and J.Garvin, "Microwave Dielectric Spectrum of Rocks," Radiation Lab. Report 023817-T, EECS, Univ. of Michigan, March, 1988.

[61] W. P. R. King, The Theory of Linear Antennas, Harvard University Press, 1956.

[62] L. M. Brekhovskikh, Waves in Layered Media, Academic Press, 1960.

[63] J. R. Wait, Electromagnetic Waves in Stratified Media, A Pergamon Press Book, 1962.

[64] J. A. Kong, "Electromagnetic fields due to dipole antennas over stratified anisotropic media," Geophys., vol. 37, pp. 985-996, Oct. 1972.

[65] E. K. Miller, A. J. Pogio, G. J. Burke, and E. S. Selden, "Analysis of wire antennas in the presence of a conducting half-space. Part I: The vertical antenna in free space," Can. J. Phys., vol. 50, pp. 879-888, 1972.

[66] E. K. Miller, "Analysis of wire antennas in the presence of a conducting half-space. Part II: The horizontal antenna in free space," Can. J. Phys., vol. 50, pp. 2614-2627, 1972.

[67] A. Karwowski and K. A. Michalski, "A comparative numerical study of several techniques for modeling a horizontal wire antenna over a lossy half-space," Radio Science, vol. 22, pp. 922-928, Nov. 1987.

[68] P. Parhami, Y. Rahmat-samii and R. Mittra,"An efficient approach for evaluating Sommerfeld integrals encountered in the problem of a current element radiation over lossy ground," IEEE Trans. Antennas Propagat., vol. AP-28, pp. 100-104, 1980.

[69] K. A. Michalski, "On the efficient evaluation of integrals arising in the Sommerfeld halfspace problem," Proc. IEE, vol. 132, Pt. H, pp. 312-318, Aug. 1985.

[70] K. A. Michalski, C. E. Smith, and E. M. Butler, "Analysis of a horizontal two-element antenna array above a dielectric halfspace," Proc. IEE, vol. 132, Pt. H, pp. 335-338, Aug. 1985.

[71] L. Tsang, R. Brown, J. A. Kong, and G. Simmons, "Numerical evaluation of electromagnetic fields due to dipole antennas in the presence of stratified media," J. of Geophys. Res., vol. 79, pp. 2077-2080, May 1974.

[72] A. Mohsen, "On the evaluation of Sommerfeld integrals," Proc. IEE, vol. 129, Pt. H, pp. 177-182, Aug. 1982.

[73] P. B. Katehi, N. G. Alexopoulos, "Real axis integration of Sommerfeld integrals with applications to printed circuit antennas," J. Math. Phys., vol. 24, pp. 527-533, Mar. 1983.

[74] I. V. Lindell and E. Alanen, "Exact image theory for the Sommerfeld half-space problem, Part I: Vertical magnetic dipole," IEEE Trans. Antennas Propagat., vol. AP-32, pp. 126-133, Feb. 1984.

[75] I. V. Lindell and E. Alanen, "Exact image theory for the Sommerfeld half-space problem, Part II: Horizontal electric dipole," IEEE Trans. Antennas Propagat., vol. AP-32, pp. 841-847, Aug. 1984.

[76] W. L. Stutzman and G. A. Thiele, Antenna Theory and Design, John Wiley & Sons, Inc., 1981.

[77] J. W. Cooley, P. A. W. Lewis, and P. D. Welch, "Application of the fast Fourier transform to computation of Fourier integrals, Fourier series, and convolution integrals," IEEE Trans. Audio Electroaccoustics, vol. 15, 1967.

[78] I. S. Gradshteyn and I. W. Ryzhik, Tables of Integrals Series and Products, pp. 707, Academic Press, 1965.

[79] W. H. Press, B. P. Flannery, S. A. Teukolsky and W. T. Vetterling, Numerical Recipes, Cambridge University Press, 1986.

[80] C. Cheon and V. Liepa, " Analysis and design of broadband antenna for anechoic chamber illumination," Nuclear EMP Meeting, Digest pp. 48, May 1988.

[81] V. Liepa and C. Cheon, " Analysis and design of 4-wire antenna for anechoic chamber excitation," IEEE AP-S/URSI Symp, San Jose, CA, June 1989.

[82] P. P. Silvester and R. L. Ferrari, Finite Elements for Electrical Engineers, Cambridge University Press, 1983.

[83] A. J. Davies, The Finite Element Method: A First Approach, New York: Oxford University Press, 1980.

[84] O. C. Zienkiewicz, The Finite Element Method, London: McGraw-Hill Book Co., 1977.

[85] O. C. Zienkiewich and K. Morgan, Finite Element and Approximation, New York: John Wiley & Sons, 1982.

[86] E. Hinton and D. R. J. Owen, Finite Element Programming, Academic Press, 1977.

[87] Z. J. Csendes, P. Silvester, " Numerical solution of dielectric loaded waveguides: I-finite-element analysis," IEEE Trans. Microwave Theory Tech., vol. MTT-18, pp. 1124-1131, Dec. 1970.

[88] B. M. A. Rahman and J. B. Davies, " Finite-element analysis of optical and microwave waveguide problems," IEEE Trans. Microwave Theory Tech., vol. MTT-32, pp. 20-28, Jan. 1984.

[89] C. C. Su, " A combined method for dielectric waveguides using the finite-element technique and the surface integral equations method," IEEE Trans. Microwave Theory Tech., vol. MTT-34, pp. 1140-1146, Nov. 1986.

[90] J.-M. Jin and J. L. Volakis, " A finite element-boundary integral formulation for scattering by three-dimensional cavity-backed apertures," IEEE Trans. Antennas Propagat., vol. AP-39, pp. 97-104, Jan. 1991.

[91] B. M. A. Rahman and J. B. Davis, " Penalty function improvement of waveguide solution by finite elements," IEEE Trans. Microwave Theory Tech., vol. MTT- 32, pp922-928, August 1984.

[92] A. Konrad, " Vector variational formulation of electromagnetic fields in anisotropic media," IEEE Trans. Microwave Theory Tech., vol. MTT-24, pp. 553-559, Sep. 1976.

[93] C. Cheon and V. Liepa, "Full wave analysis of infinitely periodic lossy wedges," IEEE AP-S/URSI Symp., May 6-10, Dallas, TX, 1990.

[94] B. M. Irons, " A frontal solution program," Int. J. Num. Meth. Eng., vol. 2, pp. 5-32, 1970.

[95] P. Hood, " A frontal solution program for unsymmetric matrices," Int. J. Num. Meth. Eng., vol. 10, pp. 379-400, 1976.

[96] V. Liepa, C. Cheon and N. Fang, " Performance of four wire antenna in anechoic chamber," Nuclear EMP Meeting, Albuquerque, NM, May 1990.

[97] C. Cheon and V. Liepa, " Analysis and design of broadband antenna for anechoic chamber illumination," The University of Michigan, Radiation Laboratory Report #026589 1-F, August 1, 1989.

[98] F. T. Ulaby, R. K. Moore, and A. K. Fung, Microwave Remote Sensing, Volume II, Addison-Wesley Publishing Co., 1982.

[99] J. A. Stratton, Electromagnetic Theory, McGraw-Hill Book Co., New-York, 1941.

[100] V. V. Liepa, " Scale model measurements of the B-52," AFWL Interaction Application Memo 36, Kirtland AFB, NM, Dec. 1980.

[101] V. V. Liepa, "Surface field measurements on scale model EC-135 aircraft for VPD and SRF data interpretation," The University of Michigan, Radiation Laboratory Report #015414 1-T, July 1977.